sid.inpe.br/mtc-m21b/2015/06.09.17.32-TDI

# COMPUTATIONAL ANALYSIS OF THE AEROTHERMODYNAMIC EFFECTS IN A REENTRY VEHICLE WITH SURFACE DISCONTINUITY LIKE A COMBINED GAP/STEP

Paulo Henrique Mineiro Leite

Doctorate Thesis of the Graduate Course in Engineering and Space Technology/Combustion and Propulsion, guided by Dr. Wilson Fernando Nogueira dos Santos, approved in June 25, 2015.

URL of the original document:
<http://urlib.net/8JMKD3MGP3W34P/3JL5CRP>

# COMPUTATIONAL ANALYSIS OF THE AEROTHERMODYNAMIC EFFECTS IN A REENTRY VEHICLE WITH SURFACE DISCONTINUITY LIKE A COMBINED GAP/STEP

Paulo Henrique Mineiro Leite

Doctorate Thesis of the Graduate Course in Engineering and Space Technology/Combustion and Propulsion, guided by Dr. Wilson Fernando Nogueira dos Santos, approved in June 25, 2015.

URL of the original document:
<http://urlib.net/8JMKD3MGP3W34P/3JL5CRP>

INPE

São José dos Campos

2015
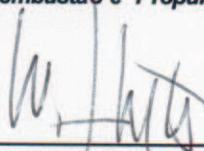
Aprovado (a) pela Banca Examinadora
em cumprimento ao requisito exigido para
obtenção do Título de *Doutor(a)* em

*Engenharia e Tecnologia*
*Espaciais/Combustão e Propulsão*

Dr.  Wilson Fernando Nogueira dos
     Santos
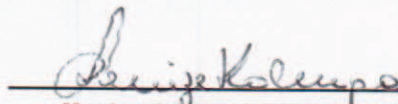
*Presidente / Orientador(a) / INPE / Cachoeira Paulista - SP*

Dr.  Jerônimo dos Santos Travelho

*Membro da Banca / INPE / São José dos Campos - SP*

Dra.  Denize Kalempa
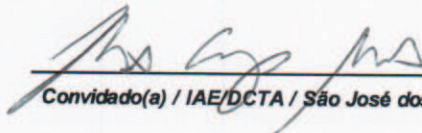
*Membro da Banca / USP/Lorena / Lorena - SP*

Dr.  Helcio Francisco Villa Nova

*Convidado(a) / UNIFEI / Itajubá - MG*

Dr.  Humberto Araujo Machado

*Convidado(a) / IAE/DCTA / São José dos Campos - SP*

*Este trabalho foi aprovado por:*

*( )  maioria simples*

*(X)  unanimidade*

**Título: "Computational Analysis of the Aerothermodynamic Effects in a Reentry Vehicle with Surface Discontinuity Like a Combined Gap/Step."**

Aluno (a):  *Paulo Henrique Mineiro Leite*

*São José dos Campos, 25 de Junho de 2015*

*"Os covardes nunca tentaram, os fracos ficaram pelo caminho, só os fortes conseguiram".*

UNKNOWN AUTHOR

*To my parents José Silvio Beraldo Leite and Nair Eklund Mineiro Leite, to my brothers Silvio Luiz Mineiro Leite and Marco Antônio Mineiro Leite, and to my daughter Helena Gomes Mineiro Leite*

# ACKNOWLEDGEMENTS

Firstly to my parents José Silvio e Nair, for always being at my side, supporting in every decision.

To my daughter Helena Gomes Mineiro Leite, who was able to understand all times that I have not been at her side.

To my teachers at the National Institute for Space Research (INPE) than with their knowledge, they formed the basis for the development of this research, with special attention to my advisor, Dr. Wilson Fernando Nogueira dos Santos, whom I have great admiration and respect since the beginning of the Master course, and to Jerônimo dos Santos Travelho.

To my really friends, especially to Débora de Oliveira Silva, Jaime César de Moura Oliveira, Lúcio Américo de Oliveira Rosa, Silvia Grandelle da Costa, Marcelo da Costa Magalhães, Alison José da Silva Seelig, Antônio Sérgio Reis Filho, Luis Thiago Lucci Correa Paolicchi, Bruno Peruchi Trevisan, Marcos da Silva e Souza, Brunna Romero Penna, Natália Ludmila Pereira Cândido, Natália de Oliveira Faria, Murilo Ghilardi Matos, Lucas Gabriel dos Santos Borba, Anderson Magalhães Melo, and Rafael da Silva Cortês.

To everybody that in your way, helped me to complete this work.

**ABSTRACT**

This work is a computational study of a hypersonic rarefied non-reacting flow past a combined gap/step configuration at zero-degree angle of attack in thermal non-equilibrium conditions. Effects on the flowfield structure and on the aerodynamic surface quantities due to changes in the gap $L/H$ ratio and on the step frontal-face height $h$ in a combined gap/step configuration are investigated by employing the Direct Simulation Monte Carlo method. The work focuses the attention of designers of hypersonic configurations on the fundamental parameter of surface discontinuity, which can have an important impact on even initial design. The results presented highlight the sensitivity of the primary flowfield properties – velocity, density, pressure, and temperature – to changes in the gap $L/H$ ratio and in the step frontal-face height $h$ in a combined gap/step configuration. In addition, the behavior of heat transfer, pressure and skin friction coefficients due to variation in the gap $L/H$ ratio and in the step frontal-face height $h$ is detailed. For the conditions investigated in the present account, the analysis shows that hypersonic flow past a combined gap/step configuration in the transition flow regime is characterized by a strong compression ahead of a combined gap/step, which influences the aerodynamic surface properties upstream and adjacent to the step frontal-face. The analysis also shows that the upstream disturbance imposed by the combined gap/step configuration increased with increasing the step frontal-face height $h$. As a consequence, it was found that the aerodynamic heating and pressure loads were affected by the step frontal-face height changes. Locally high heating and pressure loads were observed at three locations along the surface, i.e., on the lower surface, on the frontal-face surface, and on the upper surface. It was evident that these loads increased with increasing the step frontal-face $h$. Peak values for the heat transfer coefficient on the frontal-face surface were at least one order of magnitude larger than the maximum value observed for a smooth surface, i.e., a flat-plate without a combined gap/step. Furthermore, the gap $L/H$ ratio in a combined gap/step did not affect the aerodynamic surface coefficients along lower surface. Additionally, it was also found that density and pressure inside the gap in a combined gap/step configuration dramatically increased when compared to those observed for the gap alone due to the presence of the step. Finally, a comparison of the present simulation results with numerical and experimental data showed close agreement concerning to the wall pressure and kinetic temperature acting on the combined gap/step surface.

# ANÁLISE COMPUTACIONAL DOS EFEITOS AEROTERMODINÂMICOS EM UM VEÍCULO DE REENTRADA COM DESCONTINUIDADE NA SUPERFÍCIE DO TIPO FILETE/DEGRAU

## RESUMO

O presente trabalho descreve um estudo computacional de um escoamento hipersônico rarefeito não-reativo incidindo sobre uma geometria definida pela combinação de um filete e um degrau. Nesse estudo, investigou-se, utilizando-se o método Direct Simulation Monte Carlo (DSMC), o efeito na estrutura do escoamento e nas quantidades aerodinâmicas na superfície da geometria devido a mudanças na razão largura/profundidade ($L/H$) do filete e na altura $h$ da face frontal do degrau. Define-se por estrutura do escoamento a distribuição das propriedades primárias, tais como velocidade, massa específica, pressão e temperatura, ao redor da geometria filete/degrau. Denota-se como propriedades aerotermodinâmicas na superfície o fluxo de calor e as forças normal e tangencial agindo na superfície em termos de coeficiente de transferência de calor, coeficiente de pressão, e coeficiente de atrito. Os resultados obtidos apresentam o comportamento dessas propriedades devido a mudanças nos dois parâmetros geométricos, a razão $L/H$ e a altura $h$. O estudo mostrou que a estrutura do escoamento ao redor da geometria filete/degrau é caracterizada por uma forte zona de compressão a montante do degrau, na qual afeta as propriedades aerodinâmicas não somente na superfície a montante da geometria filete/degrau bem como na face do degrau. A análise também mostrou que a extensão desse efeito a montante aumentou com o aumento da face frontal $h$ do degrau. Como resultado, as cargas térmicas e de pressão foram afetadas devido a mudanças na altura $h$ do degrau. Altas cargas térmicas e de pressão foram observadas em determinadas posições na superfície a montante a geometria filete/degrau, na face do degrau, e na superfície a jusante a geometria. Os valores obtidos para o coeficiente de transferência de calor ao longo da face do degrau, foram de uma ordem de magnitude superiores ao valor máximo observado para uma superfície livre de descontinuidades, i.e., uma placa plana sem a geometria filete/degrau. No que concerne as variações da razão $L/H$ do filete em uma geometria combinada filete/degrau, observou-se que estas variações não afetaram as propriedades aerotermodinâmicas ao longo da superfície inferior, para as condições investigadas. Ademais, foi também observado um aumento expressivo nas propriedades primárias de pressão e massa específica dentro do filete presente na geometria filete/degrau, devido a presença do degrau, quando comparados aos resultados obtidos de quando da existência de somente o filete. Finalmente, dados experimentais e numéricos quando comparados com os dados obtidos pela presente simulação, mostraram estar bem próximos dos valores obtidos para as propriedades de temperatura e pressão que agem sobre a superfície da geometria filete/degrau.

# LIST OF FIGURES

xvii

xviii

# LIST OF TABLES

# Nomenclature

| | |
|---|---|
| $b$ | Impact parameter |
| $C_f$ | Skin friction coefficient, $\tau_w/(\frac{1}{2}\rho_\infty U_\infty^2)$ |
| $C_h$ | Heat transfer coefficient, $q_w/(\frac{1}{2}\rho_\infty U_\infty^3)$ |
| $C_p$ | Pressure coefficient, $(p_w - p_\infty)/(\frac{1}{2}\rho_\infty U_\infty^2)$ |
| $\mathbf{c}$ | Molecular velocity vector, $m/s$ |
| $\mathbf{c'}$ | Thermal molecular velocity, $m/s$ |
| $d$ | Molecular diameter, $m$ |
| $D$ | Diffusion coefficient, $m^2/s$ |
| $e$ | Especific molecular energy, $J/kg$ |
| $E$ | Molecular energy, $J$ |
| $f$ | Distribution function |
| $f_0$ | Equilibrium distribution function |
| $F$ | Force, $N$ |
| $F_N$ | Real molecules represented by a single DSMC particle |
| $H$ | Gap depth, $m$ |
| $k$ | Boltzmann constant, $1.3806488 \times 10^{-23}\ Js$ |
| $Kn$ | Knudsen number, $\lambda/L$ |
| $L$ | Characteristic, Gap lenght, $m$ |
| $m$ | Molecular mass, $kg$ |
| $n$ | Number density, $m^{-3}$ |
| $N$ | Number of particles |
| $N_f$ | Dimensionless number flux |
| $p$ | Pressure; Normal momentum flux, $N/m^2$ |
| $P$ | A probability |
| $Pr$ | Prandtl number, $\mu c_p/K$ |
| $q$ | Net heat flux, $W/m^2$ |
| $r$ | Intermolecular separation, $m$ |
| $R$ | Ordinary gas constant, $J/Kmol$ |
| $R_F$ | Random number between 0 and 1 |
| $Sc$ | Schmidt number, $\mu/(\rho D_{11})$ |
| $t$ | Time, $s$ |
| $T$ | Temperature, $K$ |
| $u$ | Tangential velocity, $m/s$ |
| $V$ | Cell volume, $m^3$ |
| $v$ | Normal velocity, $m/s$ |

| | |
|---|---|
| $X$ | Dimensionless length, $x/\lambda_\infty$ |
| $X'$ | Dimensionless length, $(x - L_u)/\lambda_\infty$ |
| $X'_L$ | Dimensionless length, $(x - L_u - L/2)/\lambda_\infty$ |
| $Y$ | Dimensionless height, $y/\lambda_\infty$ |
| $Y_H$ | Dimensionless height, $y/H$ |
| $Y'_H$ | Dimensionless height, $(y + H)/H$ |
| $Z$ | Relaxation collision number |

# Greek Symbols

| | |
|---|---|
| $\alpha$ | Accommodation coefficient |
| $\chi$ | Deflection angle, degree |
| $\Delta$ | Increment |
| $\epsilon$ | Molecular energy |
| $\eta$ | Power law |
| $\Gamma$ | Mass flux; Gamma function |
| $\lambda$ | Mean free path, $m$ |
| $\mu$ | Viscosity coefficient, $kg/m.s$ |
| $\nu$ | Collision frequency |
| $\omega$ | Viscosity-temperature index; Angular velocity |
| $\phi$ | Potential energy of interaction; Polar angle; Azimuth angle |
| $\Phi$ | Perturbation term |
| $\Psi$ | Azimuthal angle; Average of the degree of freedom |
| $\rho$ | Gas density, $kg/m^3$ |
| $\sigma$ | Collision cross-section, $m$ |
| $\sigma_u$ | Viscosity cross-section |
| $\sigma_M$ | Diffusion cross-section |
| $\sigma_T$ | Total collision cross-section |
| $\tau$ | Relaxation time, $s$; Tangential momentum |
| $\theta$ | Angle; Elevation angle, degree |
| $\Theta$ | Characteristic temperature, $K$ |
| $\zeta$ | Number of degrees of freedom |

# Subscripts and superscripts

| | |
|---|---|
| $i$ | Refers to incident; internal |
| $o$ | Refers to overall |

| | |
|---|---|
| $r$ | Refers to rotational; reduced; relative; reattachment |
| $rf$ | Refers to reflected |
| $ref$ | Refers to reference values |
| $t$ | Refers to translational |
| $v$ | Refers to upstream |
| $v$ | Refers to vibrational |
| $d$ | Refers to dissociation; downstream |
| $w$ | Refers to wall conditions |
| $\infty$ | Refers to the freestream |
| $c$ | Refers to cell; collision |
| $n$ | Refers to normal |
| $m$ | Refers to centre of mass |
| $n$ | Refers to pairs |
| $x, y, z$ | Refers to x-,y-, and z- cartesian axes |
| $1, 2$ | Refers to species |

# CONTENTS

# 1 INTRODUCTION

## 1.1 Motivation

Aeronautical history was made recently in March and November of 2004, when the X-43 Hyper-X test vehicle achieved hypersonic sustained flight at Mach 6.9 and 10, making it the fastest airplane in history. At hypersonic speeds, the aerodynamic heating becomes a major problem and the vehicle must be fabricated from special high-temperature materials. Due to these flow peculiarity, the knowledge of the factors that affect the thermal and aerodynamic loads and the viscous interaction, defined as a mutual interaction between external flowfield and the boundary layer growth around the vehicle surface, becomes imperative.

Usually, in the calculations of the thermal and aerodynamic loads, the analysis assumes that the vehicle has a smooth surface. However, the presence of surface discontinuities, such as protuberances, cavities, gaps or steps, in modern aerodynamic configurations occurs as a desired or undesired design feature, due for instance, fabrication tolerances, sensor installations, and differential expansion or ablation rates between non-similar materials (BERTRAN; WIGGS, 1963; BERTRAN et al., 1967; HAHN, 1969; NESTLER et al., 1969; BERTIN; KEISNER, 1978; NESTLER, 1982; MORGENSTERN; CHOKANI, 1994). These discontinuities, due to the interaction with external flows, may contribute to physical phenomena related to the problem of flow separation. When separation occurs in high Mach number flows, changes on the pressure and heat transfer distributions acting on the surface can have catastrophic effects on the vehicle. Additionally, the presence of hot spots at separation and reattachment points changes the characteristics of the flow over the vehicle and may cause failure in the thermal protection system. In order to operate safely, these loads have to be correctly predicted.

For instance, for the Space Shuttle Orbiter, Figs. 1.1 (a-b) and 1.2(a) or the X-38 vehicle, Fig.1.2(b), the thermal protection system requires gaps between the individual tiles in order to account for the thermal expansion of non-similar materials. These thermal protection system can be damage due to the vertical and lateral relative movement between adjacent tiles. This adjacent movement can cause a misalignment among these individual tiles, like forward-facing steps and gaps on the thermal protection system. The combination of forward-facing steps and large tile-to-tile gaps has caused higher than expected heating within the gaps during atmospheric entry at random locations on the lower surface of the Space Shuttle Orbiter, resulting in damage to the filler material and the Strain Isolation Pad (SIP) (Tiles are bonded

Figure 1.1 - (a) Thermal protection tiles at the lower surface of the Space Shuttle, (b) magnified view of individual tiles of the thermal protection system.
Source: NASA.
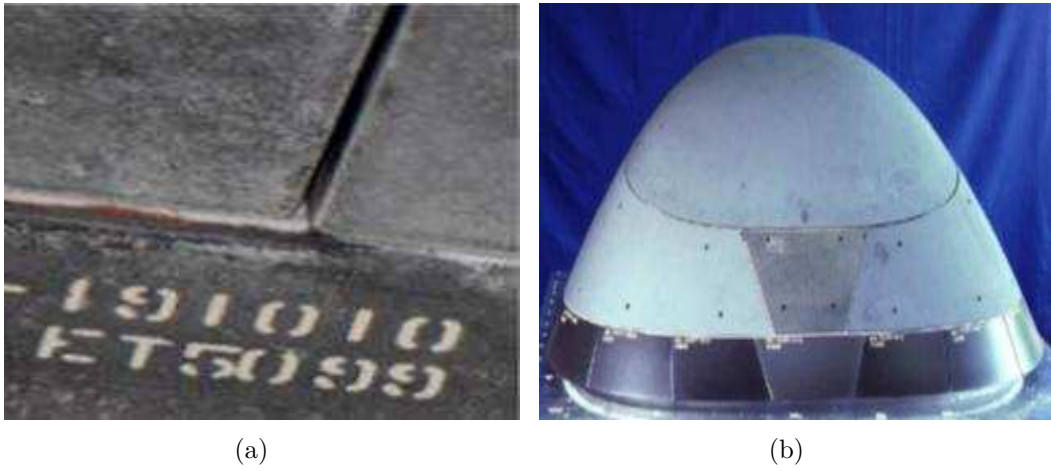


Figure 1.2 - (a) Gap/step configuration, and (b) Nose of the X-38 Crew Return Vehicle.
Source: NASA.

to the aluminium skin of the Orbiter through the SIP) (PETLEY et al., 1984). This undesired discontinuity on the vehicle surface can be defined by a gap/step configuration.

The flow on gaps, cavities, and steps may be complex due, among other things, to pressure gradients (EVERHART et al., 2006) and fluid-structure interaction (HINDERSKS; RADESPIED, 2006). In addition, the flow configuration can become even more complex if the vehicle structure is deformed by mechanical or thermal loads. Such loads can cause significant changes in the shape (dimensions) of gaps, cavities

or steps located between the thermal protection tiles on the surface of the vehicle. Consequently, such modifications in the nominal geometry of the vehicle can lead to stagnation point, hot spot, flow separation, or affect the boundary-layer transition, from laminar to turbulent.

Unfortunately, the accident with the Space Shuttle Columbia and Endeavour is an example. Afterwards the lost of the Space Shuttle Columbia, on February 1, 2003, a significant number of computational aeroheating studies (PULSONETTI et al., 2003; PULSONETTI; THOMPSON, 2004) has been released in order to understand the accident causes. These studies have focused on damage in the Thermal Protection System (TPS) of the vehicle. In this sense, the Columbia Accident Investigation Board - CAIB, (CAIB, 2003) concluded in their investigation that the Columbia accident during the STS-107 flight, which resulted in the spacecraft loss, has as the most probable cause a breach in the Thermal Protection System on the leading edge of the left wing due a piece of insulating foam that separated from the external tank and struck the wing during the launch of the Space Shuttle Orbiter. During re-entry, this breach in the thermal protection system allowed superheated air to penetrate the leading-edge insulation and progressively melt the aluminium structure of the left wing, resulting in a failure of the wing, and breakup of the Orbiter. In the same sense, during the STS - 118 mission of the Space Shuttle Endeavour, on August 8, 2007, again a piece of foam insulation was released from the external tank of the Space Shuttle and struck the TPS tiles toward the aft end of the windward surface of the vehicle. The impact caused a cavity in the Thermal Protection System. A photo extract from the CAIB and the Endeavour Space Shuttle damage location are displayed in Figure. 1.3 (a) and (b), respectively.

These examples emphasizes the importance of surface discontinuities on the flow-field structure. Furthermore, it also indicates that an detailed investigation on the aerothermodynamic loads on these surface discontinuities becomes imperative in a reentry hypersonic vehicle design.

## 1.2   Reentry Flows Regimes

Complex flow problems involving atmosphere reentry have been one of the main subjects of gas dynamics with the development of spaceflight. As an example, in a recent phase of the lunar exploration, one of its most critical aspects was reentry into the atmosphere after completion of the lunar mission, although most of the flight took place in space, outside the Earth's atmosphere. In fact, the aerothermodynamics around space vehicles is totally different in various flow regimes – free molecular
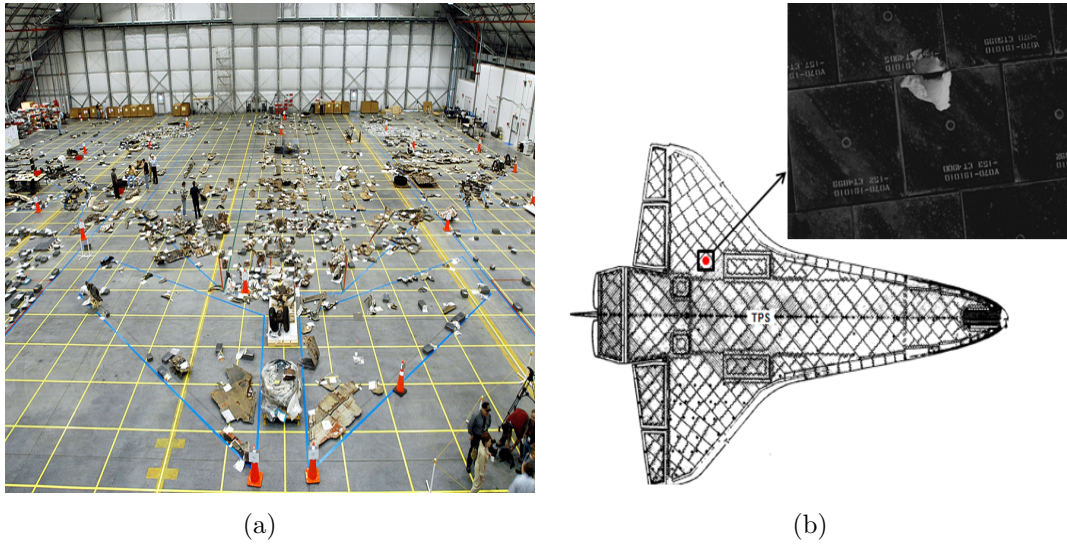
Figure 1.3 - (a) Columbia Accident Investigation Board-CAIB, and (b) Space Shuttle Endeavour damage site location.

|Source: (a) CAIB (CAIB, 2003), and (b) Palmer (PALMER et al., 2009).

flow, transition flow, slip and continuum flow – and takes into account the complex characteristics of many scales. During their trajectory, reentry vehicles cover a wide range of a flow regimes due to the rarefaction of the gas and also to the different velocity regimes, hypersonic, supersonic or subsonic. Particularly in the hypersonic speeds, some flows phenomena such as strong shock waves, viscous interactions, high temperature, or entropy layer may become important at Mach numbers around or greater than 5. It is important to mention that the definition of where the onset of hypersonic flow begins is an approximation.

Initially at highest altitudes, the interaction of the vehicle with the atmospheric air is characterized by the free molecular flow. In this regime, the molecules of the environment collide with the vehicle surface, interact with the surface and are reflected from the surface. However, collisions of reflected molecules with incoming molecules from the freestream are not frequently in this flow regime. As a result, these collisions are ignored.

As the space vehicle enters a little deeper into the dense atmosphere, the mean free path between incoming atmosphere molecules decreases, and collisions between molecules reflected from the vehicle surface and the molecules incoming from the freestream can no longer be ignored. As a result, the flow in this condition defines the transition flow regime, i.e., transition between the collisionless flow regime and

the continuum flow regime. In the transition flow regime, the contribution of aero-dynamic forces and heat flux to the vehicle surface start increasing rapidly with decreasing altitude, causing large changes in the aerodynamic characteristic of the vehicle, when compared with those observed in the free molecular flow.

Finally close to the ground, the space vehicle reaches the continuum flow regime. In this regime, the flow around the space vehicle is treated by a macroscopic model that considers the air as a continuum, and the description of the flow is made in terms of spatial and temporal variations of the primary properties, such as velocity, pressure, density and temperature.

The gas rarefaction defines which flow regime the reentry vehicle is subjected. The degree of a gas rarefaction is generally expressed by the Knudsen number ($Kn$) as follows:

$$Kn = \frac{\lambda}{L} \tag{1.1}$$

where $\lambda$ is the mean free path traveled by molecules between collisions and $L$ is a characteristic length of the problem.

It is generally accepted that kinetic non-equilibrium becomes important when $Kn$ > 0.01, and the Navier-Stokes equations are valid when $Kn$ is less than 0.1. The two main conditions that lead to non-equilibrium are low density and small length scales. A low density leads to a reduced collision rate, while a small length scale reduces the size of a fluid element. However, this can be misleading if $L$ is chosen to be some overall dimension of the flow in order to define a single overall Knudsen number for the complete flow. The limit can be specified precisely if a local Knudsen number is defined with $L$ as the scale length of the macroscopic gradients (BIRD, 1994) e.g;

$$L = \frac{\varphi}{\left|\frac{d\varphi}{dx}\right|} \tag{1.2}$$

where $\varphi$ may be density, velocity, pressure or temperature.
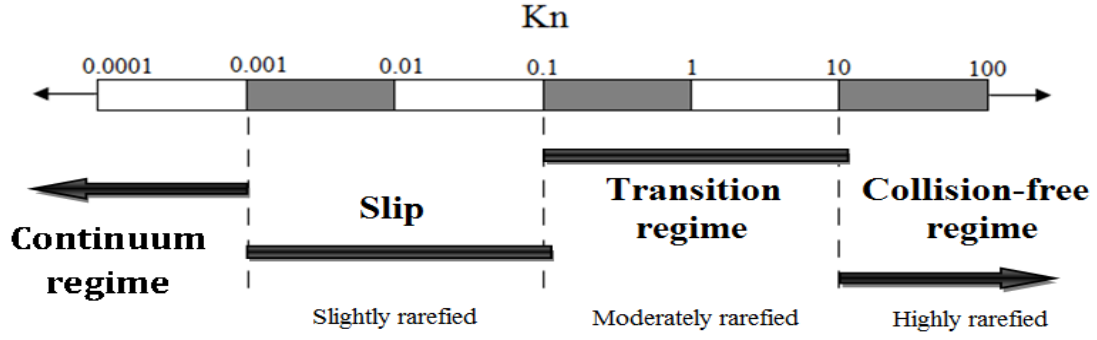
Figure 1.4 - Flow regimes as a function of the Knudsen number.

Usually, flow regimes are divided (SUN et al., 2011) into continuum ($Kn < 0.001$), slip ($0.001 < Kn < 0.1$), transition ($0.1 < Kn < 10$), and free molecular regime ($Kn > 10$). In the continuum flow regime, molecules are considered to be so densely packed that the mean free path is insignificant compared with the flow dimensions. In this way, the Knudsen number tends to zero. Conversely, free molecular flow is considered as the Knudsen number goes to infinity. Figure 1.4 presents the classification of flow regimes as a function of the local Knudsen number, and Fig. 1.5 the applicability of the conventional mathematical models.

For flows around reentry space vehicles in the range from 120 to 60 km of altitude, the molecular mean free path $\lambda$ may be of the order of the dimensions related to the discontinuities or imperfections on the vehicle surfaces. The dimensions associated to these discontinuities, the depth $H$, the length $L$, or the height $h$ related to cavities, gaps and steps are usually of the order of 3 to 16 mm (GAI; MILTHORPE, 1995; JAKUBOWSKI; LEWIS, 1973; GROTOWSKY; BALLMANN, 2000; JACKSON et al., 2001; HOZUMI et al., 2004; EVERHART et al., 2006). In such a circumstance, the Knudsen number, which indicates the degree of the flow rarefaction, may be in the range of the transition flow regime, i.e., between the continuum regime and the collisionless flow regime.

## 1.3   Previous Work

Flows over cavities, gaps or steps, often found in many engineering applications, have been investigated for several decades, since these discontinuities are often present as desired or undesired features in modern aerodynamic settings. Many experimental and computational studies (BERTRAN; WIGGS, 1963; BERTRAN et al., 1967; HAHN, 1969; NESTLER et al., 1969; NESTLER, 1982; MORGENSTERN; CHOKANI, 1994; GAI;
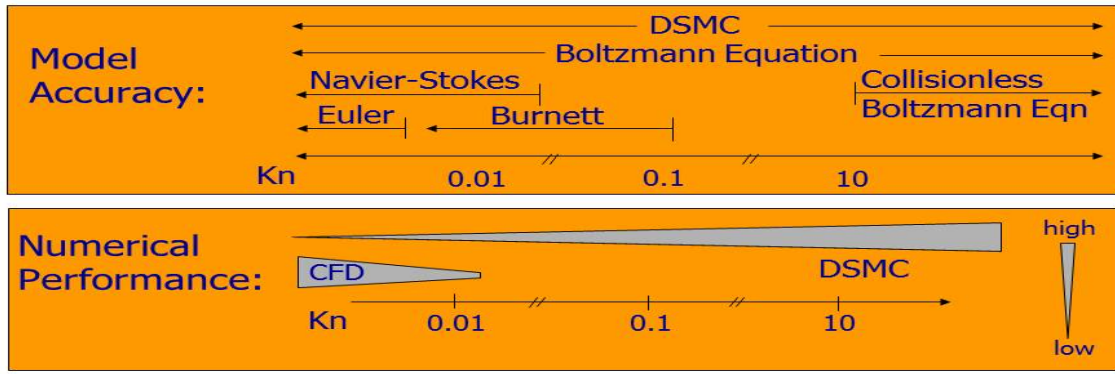
Figure 1.5 - Applicability of the conventional mathematical models as a function of the local Knudsen number.

MILTHORPE, 1995; JAKUBOWSKI; LEWIS, 1973; GROTOWSKY; BALLMANN, 2000; JACKSON et al., 2001; HOZUMI et al., 2004; EVERHART et al., 2006; HINDERSKS; RADE-SPIED, 2006; SHANKAR; DESHPANDE, 2000; ZDANSKI et al., 2004; LEE; CHANDRA, 2006; ROWLEY; WILLIAMS, 2006; NARIS; VALOUGEORGIS, 2005) have been performed with the purpose to investigate the impact of discontinuities, imperfections or distortions on the flowfield structure over hypersonic aerospace vehicles. For the purpose of this introduction, it will be sufficient to describe only a few of these studies.

Bertran and Wiggs (BERTRAN; WIGGS, 1963) investigated experimentally the effect of distortions, consisting of small protuberances and holes, on the wing of a hypersonic vehicle. The effect on pressure and heat flux to the surface was investigated for a range of Mach number from 7 to 10 and angle of attack up to 20 degrees. The results showed that these surface distortions presented a lower influence on the pressure rather than on the heat-flux distributions. They also showed that all distortions investigated caused an increase in the aerodynamic heating.

Jakubowski and Lewis (JAKUBOWSKI; LEWIS, 1973) investigated experimentally the heat and pressure distributions of a supersonic laminar flow over a backward-facing step, with/without mass suction at the separation region. In both cases, with or without suction, the step height increase led to a sharp reduction on the heating rates to the step base, which were gradually recovered to those observed in a flow without separation obtained in a flat-plate configuration. The analysis also showed that the step height is an essential parameter to the heat flux at the step base. However, for sections far away from the step, the heat flux is not dependent on the step height.

7

Bertin and Keisner (BERTIN; KEISNER, 1978) investigated experimentally the effect of a step and a gap tile misalignment, on transition locations in the plane of symmetry of the Space Shuttle Orbiter. Data were obtained for a Mach number of 8 and angle of attack of 30 degrees. Data correlations relating the location of boundary layer transition on the Space Shuttle Orbiter were presented. They concluded that the step height is more effective in the boundary layer transition than the gap length.

Transient hypersonic flow over a cavity was numerically investigated by Morgenstern Jr. and Chokani (MORGENSTERN; CHOKANI, 1994) using an implicit numerical algorithm based on three-dimensional numerical method of Yoon and Kwak (YOON; KWAKT, 1992). The objective of that study was to analyze the Reynolds number and the length-to-depth ($L/H$) ratio effects on a cavity. The analysis showed an appreciable increase on the heat flux and oscillations on the static pressure at the end of the cavity. Flow oscillations were observed at high Reynolds numbers. The results also showed that the amplitude increase of these oscillations was a function of the cavity $L/H$ ratio.

Grotowsky and Ballmannn (GROTOWSKY; BALLMANN, 2000) investigated laminar hypersonic flow over forward- and backward-facing steps by employing Navier-Stokes equations and CFD simulation. The hypersonic flow over the steps were simulated by considering freestream Mach number of 8, Reynolds number of the order of $10^8$ and an altitude of 30 km. According to them, the computational results presented a good agreement with the experimental data available in the literature. They also pointed out that the quantitative comparison exhibited major differences for the wall heat flux, probably due to the difficult in how to measure it accurately. In this fashion, they contributed to a better understanding of physical phenomena, and provided valuable information about hypersonic vehicles construction.

Pulsonetti and Willian (PULSONETTI; WILLIAN, 2005) performed an experimental investigation on open cavities at a variety of conditions. The analysis showed that wind tunnel tests and flight simulations presented similar heating patterns in the cavity. The increased levels of heating for the flight cases were due to a stronger total enthalpy gradient in the boundary layer feeding the cavity.

Based on the current literature, the flow in a continuum flow regime in cavities may be classified as illustrated in Fig. 1.6. According to Fig. 1.6, the flow regimes are identified by the $L/H$ ratio. Based on this $L/H$ ratio, four main cases can be defined as following:
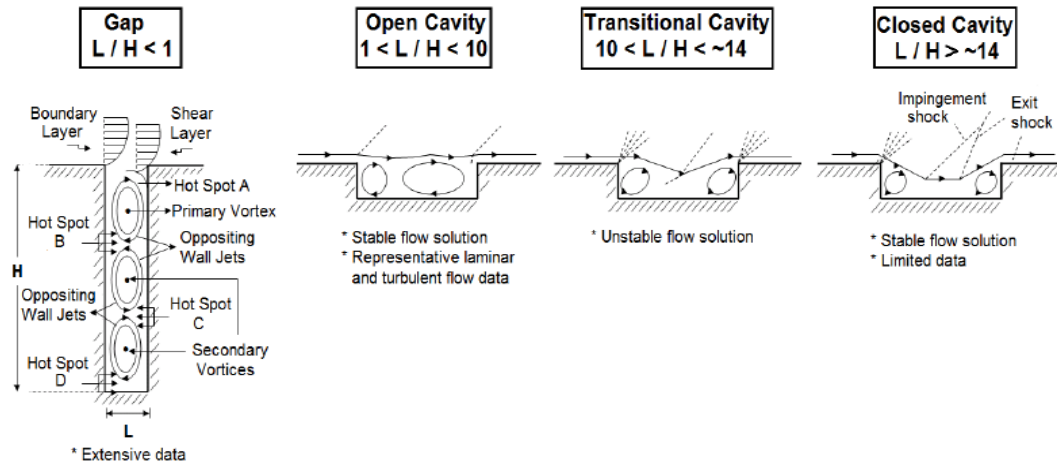
Figure 1.6 - Illustration of open and closed-cavity flow regimes.
Source: Adapted from Everhart (EVERHART et al., 2006).

- $L/H < 1$: very short or deep cavity (gap). For this particular $L/H$ range, the gap flow topology is usually defined by the development of a column of counter-rotating vortices within the gap caused by the main stream flow, where the number of vortices is approximately given by $H/L$ ratio. In addition, alternating hot spots are developed in the gap when the vortices directionally align and impinge on the gap sidewall;

- $1 < L/H < 10$: the cavity is defined as open-cavity: the mainstream flow does not enter the cavity directly, and the flow is stable. The pressure inside the cavity is much higher than that for the freestream conditions;

- $10 < L/H < 15$: the cavity is known as intermediate cavity, since the flow is unsteady and alternates between the two stable bounding conditions. This type of cavity requires a complex measuring system in an experimental investigation.

- $L/H > 15$: the cavity is known as closed-cavity; the mainstream flow is able to enter into the cavity and to impinge on the floor, and the flow is also stable. In this type of configuration, three different airflow could occurs: (1) the airflow could enter inside the cavity and impinge its lower surface. This behavior is like an airflow over a backward-facing step, (2) the boundary layer in the lower surface could develop until outside the cavity, and (3) when the airflow impinges on the other side of the cavity, it could be considered like an airflow over a forward-facing step.
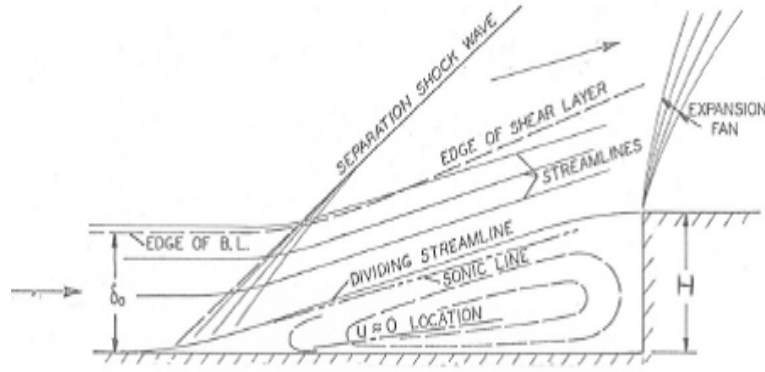
(a)
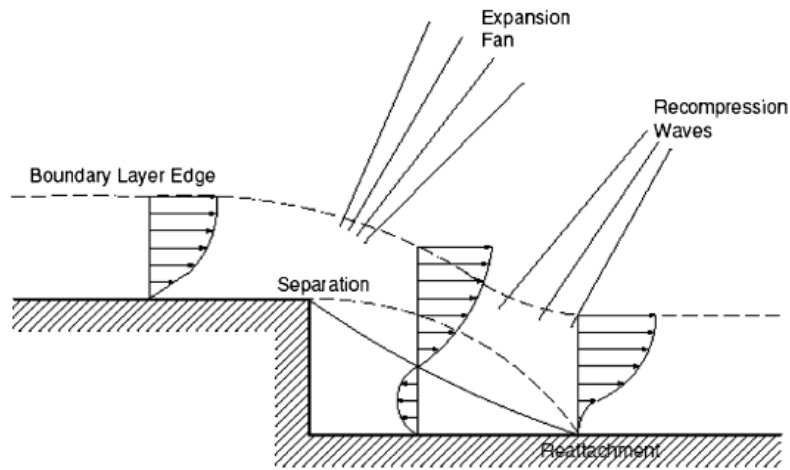


(b)

Figure 1.7 - (a) Forward-facing step and (b) Backward-facing step.
Source: Adapted from Leite (LEITE, 2009).

The limits of the $L/H$ ratio for the different types of cavities are considered only as a base. Actually, many different investigations have presented the $L/H$ ratio from 9 to 11 as a limit for open cavities, and from 12 to 15 as a limit for a closed cavity.

According to the available literature, the classical gas dynamic viscous flow features over forward- and backward-facing steps exposed to a hypersonic flow may be summarized by the schematic diagram displayed in Fig. 1.7. The flowfield around the steps is featured by a strong interaction between the viscous recirculation region and the inviscid flow of the freestream.

In many experimental and computational investigations, the flowfield around the

steps are focused in the cases when the boundary-layer thickness is lower than the step height $h$. Situations where the boundary-layer thickness is higher than the step height are very sparse. In addition, an examination of the literature revealed that the majority of the studies (BERTRAN; WIGGS, 1963; BERTRAN et al., 1967; HAHN, 1969; NESTLER et al., 1969; NESTLER, 1982; MORGENSTERN; CHOKANI, 1994; GAI; MILTHORPE, 1995; JAKUBOWSKI; LEWIS, 1973; GROTOWSKY; BALLMANN, 2000; JACKSON et al., 2001; HOZUMI et al., 2004; EVERHART et al., 2006; HINDERSKS; RADE-SPIED, 2006; SHANKAR; DESHPANDE, 2000; ZDANSKI et al., 2004; LEE; CHANDRA, 2006; ROWLEY; WILLIAMS, 2006; NARIS; VALOUGEORGIS, 2005) has considered laminar or turbulent flow for a range of Mach numbers in a continuum flow regime. However, there is a little understanding about the physical aspects of rarefied hypersonic flows past to surface discontinuities related to the severe aerothermodynamics environment associated to reentry vehicles.

In this fashion, Leite (LEITE, 2009) has presented a study on rarefied hypersonic flow over forward- and backward facing steps. This study was motivated by the interest of investigating the step-height $h$ impact on the flowfield structure. Computational results showed that the step-height changes contribute to significant modifications in the flowfield structure ahead the steps. The analysis showed a dramatically increase in the primary flow properties in the vicinity of the steps base, particularly for density and pressure. Surface aerodynamic properties were directly influenced by the recirculation region ahead the steps. High pressure and heat-flux coefficients were observed in the vicinity of the frontal-face of the steps as a consequence of the recirculation region ahead the steps.

Palharini (PALHARINI, 2010) has investigated a rarefied hypersonic flow over cavities in order to determinate the $L/H$ ratio impact on the flowfield structure and on surface aerodynamic properties. A detailed description of the macroscopic properties (velocity, density, pressure and temperature) and the surface aerodynamic properties (heat flux, pressure and skin friction coefficients) were presented for sections inside and in the vicinity of the cavity for $L/H$ ratio of 1, 2, 3 and 4. The analysis showed that the recirculation region inside the cavity is a function of the $L/H$ ratio. In the cases of $L/H < 3$, the flowfield structure on the cavities presents the same behavior of a "open cavity". In addition, for the $L/H = 4$ ratio, the flowfield structure presents the behavior of a "closed cavity". The surface aerodynamic properties were also investigated and the peak values were observed at the forward face of the cavity, more precisely at the cavity convex corner. It was also observed that the pressure and heat loads are larger than those for a flat plate without a cavity.

Finally, Paolicchi (PAOLICCHI, 2011) has investigated a hypersonic rarefied flow over a flat plate with a gap, for $L/H$ ratio of 1, 1/2, 1/3 e 1/4. The computational analysis showed that the recirculation region inside the gap in the transition flow regime is quite different from that in a continuum flow regime. It was found the recirculation region inside the gap did not depend on the $L/H$ ratio for the $L/H$ ratio investigated. It was also observed that the heat flux and pressure coefficients reached maximum values at the gap frontal-face, more precisely at the gap convex corner. In addition, these maximum values were larger than those observed to a flat plate case without a gap.

## 1.4 Objectives of the Present Work

In the present work, effort is directed to expand the previous studies on surface discontinuities (LEITE, 2009; PALHARINI, 2010; PAOLICCHI, 2011) by investigating another surface discontinuity defined by the combination of a gap and a step, a gap/step configuration. The primary goal is to provide a comprehensive description of the flowfield structure and the aerodynamic surface quantities with special relevance to the aerodynamic heating.

It is important to recall that this type of discontinuity may occur in the windward surface of the Space Shuttle configuration. The windward surface is composed by a large number of thermal protection tiles. However, a misalignment between individual tiles may occur, as earlier shown in Figs. 1.1 and 1.2. Therefore, the misaligned tiles may constitute in a potential source in a heat flux and pressure rise on the surface or even though in a premature transition from laminar to turbulent flow.

In this work, the flowfield structure is defined by the distribution of the primary properties, such as velocity, density, pressure, and the kinetic temperature, adjacent to the vehicle surfaces. Aerodynamic surface quantities are identified by the heat flux, and the normal and tangential forces acting on the vehicle surface.

In order to guide the reader, a breakdown of the purpose and contents of the following chapters is provided below.

- Chapter 2: In this chapter, a description of the appropriate computational method is presented. Particular emphasis is placed on the DSMC methodology, collision model, molecular model, Larsen-Borgnakke model, relaxation rate, internal degrees of freedom, boundary conditions, binary collision mechanics, and elastic collision models.

- Chapter 3: The computational procedure is explored in this chapter. It includes the simulation conditions, the definition of the geometry analyzed in this research as well as the important geometric parameters.

- Chapter 4: This chapter outlines the procedure for the verification and validation process of the DSMC code employed in the simulations. These procedures are applied in a test case defined by a flat-plate. The DSMC code is validated with simulation of a hypersonic flow over a flat-plate, and comparisons with previous experimental and numerical results are presented.

- Chapter 5: The purpose of this chapter is to present the computational results and discussion. In this chapter, the major features of the primary properties such as, velocity, density, pressure and kinetic temperatures, are discussed in details. Moreover, the aerodynamic surface quantities such as, number flux to the surface, heat flux, pressure, and shear stress, expressed in a coefficient form, are carefully examined.

- Chapter 6: The final chapter of this Ph.D Thesis contains a summary of the results obtained throughout the course of this work, and the conclusions that were drawn from them.

## 2 COMPUTATIONAL METHOD

### 2.1 Methods for Modeling Transition Flows

It is well established in the literature that hypersonic flows around bodies entering in a planetary atmosphere are characterized by a flow separation and by a thin shock viscous layer between the shock wave and the body surface. The flow separation and the viscous interaction phenomena have an adverse effect on the drag, surface heat flux and pressure distributions on the body surfaces. In this sense, it is important to make accurate quantitative predictions of the behavior of these separated flows and the viscous effects in the flowfield structure. For this reason, analytical and computational models of hypersonic separated and viscous flows have been a subject of active research for more than 50 years. Despite these efforts, a comprehensive predictive capability for the thermal and fluid flow behavior of separated viscous hypersonic low-density flows remains under constant investigation.

In many cases at hypersonic speeds, the shock layer is of the same magnitude as the boundary-layer, and as a consequence, the boundary-layer deflects the external inviscid flow, creating a comparably strong and curved shock wave which trails downstream from the leading edge. In turn, the surface pressure from the leading edge is considerably higher than freestream pressure $p_\infty$, and only approaches $p_\infty$ far downstream of the leading edge. In addition to influencing the aerodynamic forces, such high pressure increases the aerodynamic heating at the leading edge. It should be remarked that high temperatures in the shock layer is a dominant aspect of hypersonic flows. The temperature around the body can reach a few hundred thousand Kelvin and, as a consequence, molecules may undergo chemical reactions, decomposition, dissociation, or recombination. Thus, translational, rotational, vibrational, and eletronic temperatures differ from one to another, and the state becomes a non-equilibrium state. Thermal non-equilibrium occurs when the temperatures associated with translational, rotational, and vibrational modes of a polyatomic gas are different one to another.

The study of physical phenomena in rarefied non-equilibrium flows is a challenging problem directly related to the development of new aerospace technologies. Rarefied gas dynamics, that deals with these phenomena, is the synthesis of a great number of fundamental problems such as molecular collision dynamics, energy transfer phenomena in collisions, gas-surface interactions, and many others. Substantial difficulties arising in the study of such flows are caused by problems related to rarefaction and physico-chemicals effects.

It is commonly known that experimental simulation of non-equilibrium low-density flows is rather problematic and expensive. The difficulties of experimental modeling have estimulated intense development of various approaches for numerical simulations of these flows. Nowadays there are some numerical approaches for solving problems of rarefied gas dynamics, and the choice of this or that approach depends usually on the flow rarefaction, the problem dimension and the presence of real gas effects.

The conventional continuum flow assumption is valid when the overall Knudsen number tends to zero. In this flow regime, the velocity distribution function everywhere in a flowfield has the Maxwellian form. As a consequence, the transport terms, such as viscosity and thermal conductivity, vanish in the limit of zero Knudsen number. In this condition, the Navier-Stokes equations are reduced to the inviscid Euler equations. Indeed, the Euler equations of a fluid flow can be derived by taking moments of the Boltzmann equation (BOYD, 2014) and evaluating them by using the Maxwellian velocity distribution function. In this way, one can disregard its microscopic structure and consider only its macroscopic properties such as density, velocity or temperature.

For near-continuum flow, it is usually sufficient to take into account the effects of rarefaction through the boundary conditions of slip velocity and temperature jump on the surface. Navier-Stokes or viscous shock layer equations are commonly used here with these conditions. Navier-Stokes equations can be derived from the Boltzmann equation (CERCIGNANI, 1988) under the assumption of small deviation of the distribution function from equilibrium. The traditional requirement for Navier-Stokes equations to be valid is that the Knudsen number should be less than 0.1. The error in these equations is significant in the regions of the flow where the appropriately defined local Knudsen number exceeds 0.1, and the upper limit on the local Knudsen number, at which the continuum model must be replaced by the molecular model, may taken to be 0.2.

As the Knudsen number increases from zero up to values close to 0.01, the velocity distribution function in the flowfield may be represented as a small perturbation of the equilibrium Maxwellian form that is known as the classical Chapman-Enskog distribution (VICENTI; KRUGER, 1967). Evaluation of moments of the Boltzmann equation using the Chapman-Enskog velocity distribution function leads to the Navier-Stokes equations, in which shear stress and the heat flux depend linearly on the spatial gradients of velocity and temperature, respectively. As the Knudsen

number rises above 0.01, these linear transport relations are unable to accurately describe the strong non-equilibrium processes. In this situation, it is necessary to develop higher orders sets of partial differential equations, such as the Burnett equations (BURNETT, 1936), or to solve the Boltzmann equation (CERCIGNANI, 1988).

The range defined by $0.1 < Kn < 10$ is referred as the transition flow regime, where not only gas-surface collisions but also intermolecular collisions are important. In the transition flow regime, viscosity, heat conduction, relaxation, diffusion and chemical processes are important. The velocity distribution functions may be non-Maxwellian, thus a gas falls into a non-equilibrium state under conditions where there is not a large enough number of collisions occurring to maintain equilibrium, resulting in strong thermal non-equilibrium.

Finally, when the overall Knudsen number goes to infinity, the flow regime corresponds to the collisionless or free molecular flow. In this case, intermolecular collisions may be neglected and particle collisions with the body surface play the determining role. In this sense the Navier-Stokes equations become unsuitable for studying rarefied flows with finite Knudsen numbers where the distribution function becomes considerably in nonequilibrium. Also, the transport terms of the Navier-Stokes equation of continuum gas dynamics fail when gradients of the macroscopic variables becomes so steep that their scale length are of the same order as the average distance travelled by the molecules between collisions, i.e., the mean free path $\lambda$.

Analytical models have tended to be too simple to capture all the interacting processes that lead to separation and non-equilibrium state, while computational models, using numerical solutions of the Navier-Stokes equations, make assumptions about the flow behavior that become invalid at lower densities where rarefaction effects become significant. In such cases, non-equilibrium state and high degree of gas rarefaction, the molecular collision rate is low and the energy exchange occurs under non-equilibrium conditions. In such a circumstance, the Navier-Stokes equations are inappropriate due to the high degree of molecular non-equilibrium. In this case, it is necessary to solve the Boltzmann equation. Unfortunately, the development of a robust and general numerical solution schemes for the Boltzmann equation has also proved to be a significant challenge. Again, some progress has been made, but there is still much work to be done in order to simulate all of the flow physics relevant to hypersonic flows (BOYD, 2014). An alternative particle-based computational method, the Direct Simulation Monte Carlo (DSMC) method (BIRD, 1994),

has been demonstrated to provide physically realistic simulations at low densities, but it becomes computationally expensive as the density of particles increases, as shown in Fig. 1.5.

## 2.2 Direct Simulation Monte Carlo (DSMC) Method

The Direct Simulation Monte Carlo (DSMC) method is nowadays a popular and mature technique for simulation of rarefied gas flows (BURT; JOSYULA, 2011). The method, pioneered by Bird (BIRD, 1976; BIRD, 1994), is a well-established technique, and has become the main technique for studying complex multi-dimensional rarefied flows. It has been recognized as an extremely powerful tool capable of predicting an almost unlimited variety of rarefied flowfields in the regimes where neither the Navier-Stokes nor the free molecular approaches are appropriate. Among other applications, DSMC simulations are often utilized for applications related particularly to shock structure analysis and low density atmospheric flows around reentry and launch vehicles. The method emulates the same physics as the Boltzmann equation without providing a direct solution. The DSMC method follows a representative set of particles as they collide and move in a physical space. It has been demonstrated that DSMC converges to the solution of the Boltzmann equation in the limit of a very large number of particles (WAGNER, 1992).

The DSMC method is based on the physical concepts of rarefied gases and on physical assumptions that form the basis for the phenomenological derivation of the Boltzmann equation (BIRD, 1994). However, it is not derived from the Boltzmann equation itself. As both are based on the classical kinetic theory, the DSMC method is subject to the same restrictions as the Boltzmann equation. This requires the assumption of molecular chaos and the restriction to dilute gases (BIRD, 1994).

The method has been thoroughly tested in high Knudsen number flows over the past 50 years, and found to be in excellent agreement with experimental data (MOSS; SCOTT, 1986; MOSS et al., 1995; HARVEY; GALLIS, 2000). Comparisons with experiments have given credibility and have been vital in gaining widespread acceptance of the method. The potential advantages of the method that make it usable for practical scientific and engineering applications are conditioned to the comparative simplicity of transition from one-dimensional problems to two- and three-dimensional ones. Also, the DSMC method have the possibility of incorporating complex models of gas particle interaction, including the models of internal degrees of freedom and chemical reactions, without substantial complication of the computational algorithm and without significant increase in computational costs. It is also well suited for use on

modern computer architectures.

Since it is impossible to simulate the actual number of molecules in the computational domain, a smaller number of representative molecules, referred as simulated particles are used, each one representing a large number of real molecules (SHU et al., 2005). In this context, a large population of particles are used to represent discrete molecules each one with a position, velocity and internal energy. The state of the simulated particles is stored and modified with time as the particle move, collide and undergo boundary interactions in simulated physical space. The assumption of a dilute gas, which means that the mean molecular diameter is much less than the mean molecular spacing of molecules in the gas, allows for the molecular motion to be decoupled from the molecular collisions over discrete time step intervals, which are small in comparison to the local mean collision time (BIRD, 1994). During collision operations, a fraction of particles in each computational cell are paired with other nearby particles, and some or all of these pairs are selected to participate in binary collisions, which follow underlying dynamics of the collision term in the Boltzmann equation (BURT; JOSYULA, 2011).

A computational cell network, which represents the physical space, is required for the method execution. The cell provides a convenient reference for the sampling of the macroscopic gas properties and for the choice of the potential collision pairs (XUE et al., 2000). The dimension of the cells must be such that changes in flow properties across each cell be small. The linear dimensions of the cells should be small in comparison with the mean free path $\lambda$ in the direction of primary gradients (BIRD, 1994). Violation of cell dimension restriction leads to erroneous results, as was presented by Meiburg (MEIBURG, 1986) and other studies (ALEXANDER et al., 1995; ALEXANDER et al., 1998). In their analysis, Alexander (ALEXANDER et al., 1995) confirm that significant errors occurs when the cell dimensions are larger than the local mean free path $\lambda$. Since local mean free path $\lambda$ is inversely proportional to the density flow, high density flows demand more computational cells. This means that more molecules are simulated and more collisions are computed. Also, in order to minimize the smearing of gradients, the mean separation distance of the collision pair should be reduced. Bird (BIRD, 1987) solved these conflicting requirement by introducing the option of subdividing the sampling cell into an arbitrary number of sub-cells for the selection of collision pairs. In this way, the smallest unit of physical space is the subcell, where the collision partners are selected for the establishment of the collision rate. This procedure improves accuracy by ensuring that collisions occur only between near neighbors.

Another requirement of the DSMC method is the lower limit on the number of simulated particles per cell. As noted above, the DSMC method uses the cell system for the sampling of the macroscopic properties and for the selection of collision partners. The sampled density is used in the procedures for establishing the collision rate, and it is desirable to have the number of simulated particles per cell as large as possible. Furthermore, the corresponding number of possible collision pairs becomes too much large as the number of simulated particles in a unit cell is as large as possible. Therefore, in the selection of the collision partner, it is desirable to have the number of simulated particles per cell as small as possible. Chen and Boyd, (CHEN; BOYD, 1996) observed that the computed solution might be biased when a limited number of simulated particles is employed in the simulation. In this way, it is advisable that each cell be populated with a minimum number of simulated particles, typically around twenty (FALLAVOLLITA et al., 1993; CHEN; BOYD, 1996; SHU et al., 2005).

One additional requirement in the DSMC method is a proper time step $\Delta t$. The paths of the simulated particles are traced out in physical space by decoupling motion from intermolecular collisions. The size of the time step over which decoupling occurs should be chosen to be significantly smaller than the mean time between collisions (XUE et al., 2000). A very small time step results in an inefficient advancement of the solution and accumulation of statistics. Most simulated particles will take many time steps to cross a given cell. As a result, the collision phase of each time step will involve the same group of simulated particles as in the previous time step, since almost no simulated particles leave or enter the cell. Also, a large time step allows the simulated particles to move too far without the opportunity to participate in a collision. This again causes a smearing of the properties of the flow, resulting in yielding inaccurate or non-physical results. In this manner, the time step should be chosen such that a typical simulated particle moves about one fourth of the cell dimension, at each time step (LIU; YIN-KWEENG, 2002). It should be remarked in this context that stability problems are completely absent in the DSMC method and consequently, the DSMC method is not subject to a stability criterion such as the Courant-Friedrichs-Lewy condition of traditional Computational Fluid Dynamics (CFD). Since the DSMC method avoids the breakdown of continuum assumption in traditional CFD, it extends the validated range of numerical simulation.

Broadly speaking, the computational approximations associated with DSMC method are the ratio of the number of simulated particles to the number of real molecules, the time step over which the molecular motion and collisions are un-

coupled, and the finite cell and sub-cell sizes in physical space. The fundamental requirements are that the linear dimensions of the cells should be small in comparison with the scale length of the macroscopic flow gradients in the streamwise direction, which generally means that the cell dimensions should be of the order of the local mean free path, and the time step should be much less than the local mean free collision time. Theoretically, the method become more exact when the cell size and the time step tend to zero (ALEXANDER et al., 1998; ALEXANDER et al., 2000; XUE et al., 2000).

Finally, the DSMC method is so far the most successfully one as the numerical simulation of transitional flow regimes is concerned (MOSS; BIRD, 2003; ORAN et al., 1998; STRUCKMEIER; STEINER, 1995) and has the advantage of being more efficient than other particles based methods, because the place and time collision are no longer determined by computing the trajectories of all particles, but by means of a statistical consideration.

### 2.2.1 DSMC Methodology

The DSMC method is a particle-based numerical modeling technique that computes the trajectories of a large number of particles and calculates macroscopic quantities by sampling particle properties. The application of the method is displayed in Figure 2.1. Based on this figure, the DSMC algorithm may be divided into four basic procedures: (1) given a time step $\Delta t$, particles along their trajectories are displaced and interactions with boundary are calculated as they occur, (2) particles are sorted and their cell locations are rearranged, (3) collisions pairs are selected and intermolecular collisions are performed on a probabilistic basis, and (4) flow properties as velocity, temperature, and density are obtained by sampling the microscopic state of the simulated particles.

At the beginning of the simulation, the computational domain is divided into a net of cells representing the physical space where each particle is positioned inside the cell with a velocity that was assumed to be a linear combination of the thermal velocity and the freestream velocity, and also have an internal energy. At this time, the computational domain is initialized with a uniform equilibrium gas condition that agrees with the freestream conditions in the physical space. Boundary conditions corresponding to the desired flow are imposed at time zero and should be such that a steady flow is established at a sufficient large time, and the desired steady result is a time average of all values calculated after reaching the steady state.
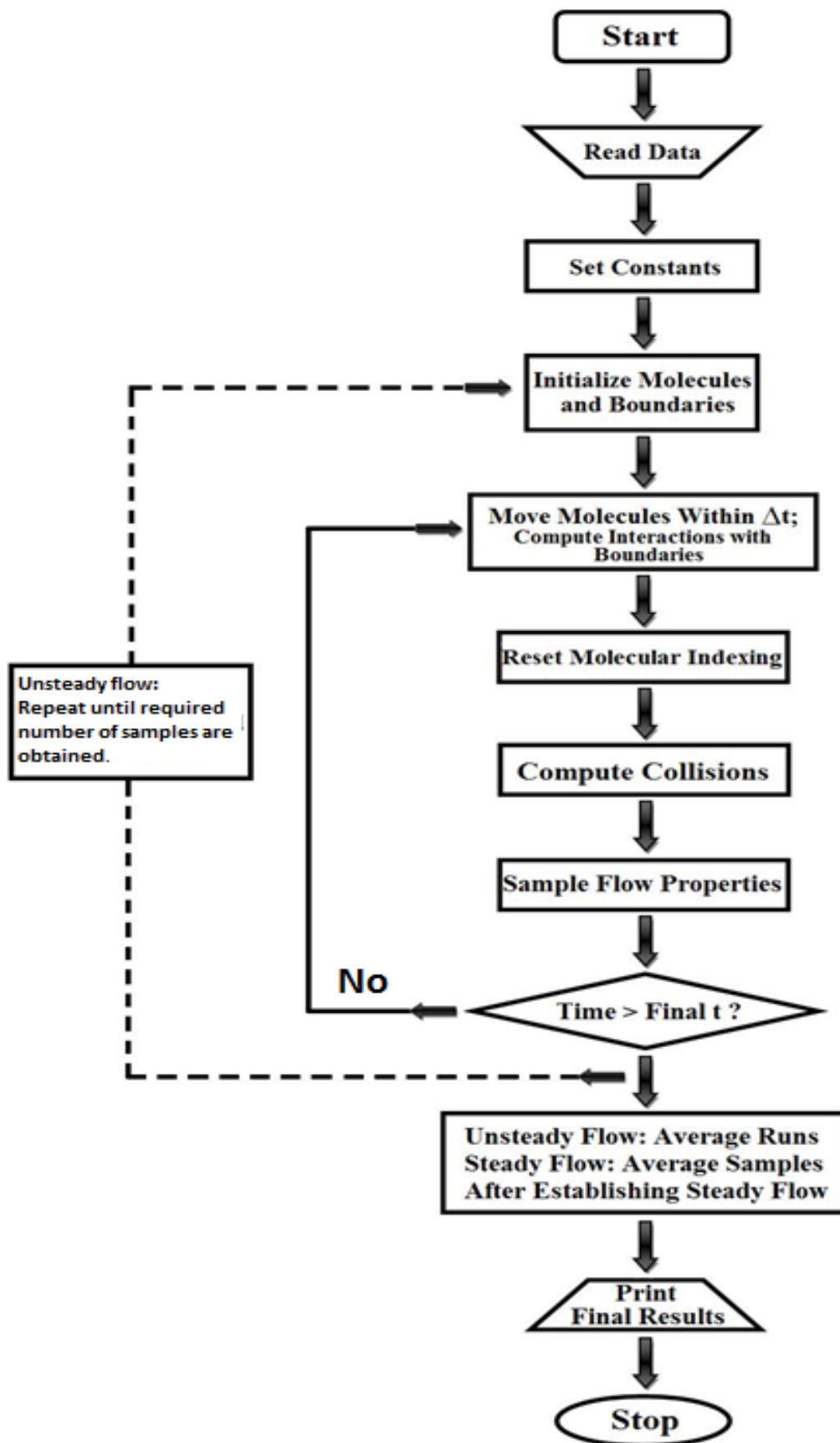
Figure 2.1 - Flowchart of DSMC Method.

Source: Sebastião (SEBASTIÃO, 2011).

In a second stage, the computation proceeds in small discrete time step $\Delta t$, making all particles to be moved through distances appropriate to their velocity components. At this time, the motion of the particles and their interactions are uncoupled. Within one time step, all particles are first advanced according to their individual velocity, and interactions with boundary are calculated as they occur. Once a particle has been moved, its location in the computational domain must be determined. For simple cartesian meshes, particle destinations are quickly computed, and the new cell is computed by using indexing schemes (BIRD, 1994). For structured and unstructured grids, efficient particle tracing schemes are outlined by Dietrich (DIETRICH, 1990) and Laux (LAUX, 1997), respectively.

After establishing the location of the particles, appropriate action is taken if the particles cross boundaries representing solid surface, lines, surfaces of symmetry or the outer boundary of the flow. Particles crossing the side from the computational domain are removed from the flow. New particles are introduced to the simulation at the outer boundaries of the computational domain for freestream boundary conditions or from within the domain from sources. Collisions with surfaces can be treated as being either fully specular, fully diffuse or some combination of these two. Modeling molecule-surface interactions requires applying the conservation laws to individual particles instead of using the velocity distribution function.

The third step of the simulation consists in a selection of the possible collision pairs to be selected inside the subcells. Inside of them, a certain number of statistical collisions must be computed. Several different collision modeling schemes have been formulated and applied in the DSMC method. Among them, one has the time-counter (TC) technique (BIRD, 1976), Nanbu scheme (NANBU, 1986), null-collision (NC) technique (KOURA, 1986),(KOURA, 1998), no-time-counter(NTC) technique (BIRD, 1989) and the generalized scheme (ABE, 1993) of the no-time-counter technique. The NTC scheme proposed by Bird (BIRD, 1989) for the DSMC is the preferred model currently used along with the subcell approach discussed earlier. The collision procedure takes place on a cell-by-cell basis. The time step, the cell volume and the number of particles resident in the cell will determine the number of candidate collision pairs that will be evaluated. The particles are randomly selected as collision partners with the restriction that their mean separation be a fraction of the molecular mean free path. This restriction is enforced by selecting collision pairs from the list of particles in the subcell. The DSMC method evaluates individual collision in a probabilistic basis, conserving momentum and energy.

Finally, the current description is completed by considering the sampling of the macroscopic flow properties such as density, velocity, pressure and temperature by appropriate averaging of the microscopic state of particles in each cell.

### 2.2.2 Collision Models

The DSMC method emulates the physics of the Boltzmann equation by following the motions and collisions of a large number of simulated particles. Therefore, it is traditionally considered as a method of computer simulation of the behavior of a great number of model gas molecules. Usually, the number of simulated particles is large enough – $\approx 10^5 - 10^6$ – but this is extremely small in comparison with the number of molecules that would be present in the real gas flow. Each simulated particle is then regarded as representing an appropriate number of real molecules. Each particle possesses molecular level information including a position and a velocity vector, and physical information such as mass and size. Particle motion and collisions are decoupled over a time step $\Delta t$ that is smaller than the local mean free time. During the movement of the particles, boundary conditions such as reflection from solid surfaces are applied. The physical domain to be simulated in a DSMC computation is covered by a mesh of cells. These cells are used to collect together particles that may collide (BOYD, 2014) and for the sampling of macroscopic flow properties such as density, velocity and temperature.

The DSMC technique calls for the estimation of a quantity called total collision cross-section (the cross-section of an imaginary sphere surrounding a molecule into which the centre of another molecule cannot penetrate) of the interacting particles. This quantity is necessary for the calculation of the collision frequency, the collision probability and the mean free path of the particles, which is used for setting the dimensions of the cell structure. In addition, the scattering angle is also estimated for the computation of the post-collision velocities of a colliding pair of particles. In the following, the total collision cross-section $\sigma_T$ is expressed by (PRASANTH; KAKKASSERY, 2008):

$$\sigma_T = 2\pi \int_{b_1}^{b_2} b\,db \tag{2.1}$$

This relation is useful only when the relation between the deflection angle $\chi$ and the parameter $b$ is known so that the terms inside the integral sign could be expressed

in terms of $\chi$. The impact parameter $b$ is the distance of closest approach of the trajectories of two particles in the centre of mass frame of reference, unaffected yet by the intermolecular force. The specification of the impact parameter allows the deflection angle to be calculated. The smaller this parameter, the greater is the effect of interaction. When $b$ exceeds a certain limit, the particles do not interact with each other.

In addition to the total cross-section, the so-called viscosity cross-section $\sigma_u$ and the diffusion cross-section $\sigma_M$ are also important. These are certain convergence integrals, which are encountered in the Chapman Enskog theory (HIRSCHFELDER et al., 1954) for the coefficients of viscosity, thermal conductivity and diffusion. Their expressions in terms of the impact parameter and deflection angle are:

$$\sigma_u = 2\pi \int_{b_1}^{b_2} sin^2\chi b db \tag{2.2}$$

$$\sigma_M = 2\pi \int_{b_1}^{b_2} (1 - cos\chi) b db \tag{2.3}$$

The reference molecular diameter for the estimation of the total collision cross-section in a particular molecular model is obtained by equating the temperature dependent expression for the coefficient of viscosity of that model to the experimentally observed coefficient of viscosity, at a particular reference temperature. In the transport theory of Chapman-Enskog, the first approximation to the coefficient of viscosity $\mu$ at a temperature $T$ of a gas is given as (VICENTI; KRUGER, 1967)

$$\mu = \frac{\frac{5}{8}\sqrt{\pi m k T}}{(m/4kT)^4 \int_0^\infty c_r^7 \sigma_u e^{-mc_r^2/4kT} dc_r} \tag{2.4}$$

where $m$ is the molecular mass, $k$ the Boltzmann constant and $c_r$ the relative molecular speed. The evaluation of the quantities inside the integral sign depends on the molecular model under consideration, which results in different expressions for the coefficient of viscosity for different models.

In order to compute the collisions between these simulated particles, several different collision-modeling schemes have been formulated and implemented in the DSMC method, and all of them achieve a faster numerical performance than those in molecular dynamics (MD) by ignoring the influence of the relative positions of particles within a cell in determining particles that collide. Among them, the time-counter (TC) technique (BIRD, 1976), Nanbu scheme (NANBU, 1986), null-collision (NC) technique (KOURA, 1986; KOURA, 1998), no-time-counter (NTC) technique (BIRD, 1989) and the generalized scheme (ABE, 1993) of the no-time-counter technique. NTC scheme (BIRD, 1989) is the most widely used collision scheme in which a number of particle pairs in a cell is formed and is given by:

$$N_c = \frac{1}{2} n \bar{N} (\sigma_T c_r)_{max} \Delta t \tag{2.5}$$

where $n$ is the number density, $\bar{N}$ is the average number of particles in a cell, $\sigma_T$ is the total collision cross section, and $c_r$ is the relative molecular speed. Each one of the $N_c$ pairs of particles is formed at random regardless of position in the cell, and then a probability of collision for each pair is evaluated using:

$$P_c = \frac{\sigma_T c_r}{(\sigma_T c_r)_{max}} \tag{2.6}$$

This procedure reproduces the expected equilibrium collision rate under conditions of equilibrium. It is determined whether the particle pair actually collides by comparing the collision probability, $P_c$, to a random number $R_F$. When collision occurs, post-collision velocities are calculated using conservation of momentum and energy (BOYD, 2014).

### 2.2.2.1 Collision Frequency

The mean free path is defined in a frame of reference moving with the stream speed of the gas and is therefore equal to the mean thermal speed $\bar{c'}$ divided by the collision frequency, $\nu$, i.e.,

$$\lambda = \bar{c'}/\nu \tag{2.7}$$

The mean thermal speed $\bar{c}'$ in a equilibrium gas at temperature $T$ is given by

$$\bar{c}' = \frac{2}{\pi^{1/2}\beta} \tag{2.8}$$

Where $\beta = (2RT)^{-1/2}$ is the reciprocal of the most probable molecular speed. The combination of Eqs. 2.7 and 2.8 gives an expression of the collision frequency at temperature $T$ (XUE et al., 2000), i.e.

$$\nu = \frac{2}{\lambda}\sqrt{\frac{2RT}{\pi}} \tag{2.9}$$

### 2.2.2.2  Probabilistic Nature of Collision Between Molecule Pairs

As one of the fundamental requirements, the computational time step $\Delta t$ can be roughly estimated by $\Delta t << (1/\nu)$, i.e. the time step should be much smaller than the mean collision time. The NTC scheme proposed by Bird (BIRD, 1989) is a generalized scheme, in which the number of collisions pairs ($N_p$) considered in a given cell is computed through the following equation,

$$N_p \propto \Delta t \frac{N_c^2}{n_{ref}V_c} \tag{2.10}$$

where $V_c$ is the volume of a cell, $N_c$ is the number of computational particles in a cell, $n_{ref}$ is the simulated number density (the total simulated particles divided by the total simulated volume). NTC scheme can overcome the defects of other schemes, such as the time-counter (TC) by Bird (BIRD, 1976) and the null-collision scheme (NC) by Koura (KOURA, 1986)(KOURA, 1998). The sensitive tests of the schemes for the evaluation of the lower limit of the mean molecular number per cell ($N_{c,min}$) were carried out by Koura (KOURA, 1990) and Kaburaki and Yokokawa (KABURAKI; YOKOKAWA, 1994). The recommended $N_{c,min}$ is between 4 to 30. Considering a DSMC cell of volume $V_c$, in which each simulated particle represents $F_N$ real molecules, the probability $P$ of a collision between two simulated particles over the time internal $\Delta t$ is proportional to the product of their relative speed $c_r$ and the total cross-section $\sigma_T$, i.e.

$$P = \frac{F_N \sigma_T c_r \Delta t}{V_c} \qquad (2.11)$$

The average number of real molecules in the cell is $nV_c$ and averaged number of simulated particles is $N = nV_c/F_N$. The full set of collisions can be calculated by selecting, in turn, all $N(N-1)/2$ pairs in the cell and computing the collisions with probability $P$. In order to carry out the simulation more efficient, only a fraction of the pairs are chosen. The resultant probability is increased by dividing Eq.2.11 by this fraction. Hence,

$$P_{max} = F_N (\sigma_T c_r)_{max} \Delta t / V_c \qquad (2.12)$$

In the NTC Scheme $(1/2)N\bar{N}F_N(\sigma_T c_r)_{max}\Delta t/V_c$ pair are chosen from the cell at the time step, where $\bar{N}$ is an average value. The collision is then computed with probability $\sigma_T c_r/(\sigma_T c_r)_{max}$ as seen in Eq. 2.6 (XUE et al., 2000).

### 2.2.3 Molecular Model

In the procedures involved in DSMC, the accuracy of the simulation of the intermolecular collisions depends on the collision model adopted in the collision routine. In order to accurately and reliably simulate the molecular collisions process in DSMC, realistic collisions models based on physically realistic interaction potentials are critical. The simplest molecular model is the hard-sphere model (HS), and after this more and more refined collision models were introduced for the use in DSMC. Thus, the variable hard-sphere (VHS) (BIRD, 1981), the variable soft-sphere sphere (VSS)(KOURA; MATSUMOTO, 1991), and the generalized hard sphere (GHS) (HASSAN; HASH, 1993) were put forward by many researchers, and all these models have varying individual degrees of success. Meanwhile, the Larsen-Borgnakke (LB), statistical inelastic cross-section models for both continuous or discrete internal energy and the dynamic molecular collision model were proposed for the treatment of polyatomic molecules in which transfer of energy among translation, rotational and vibrational degrees of freedom is possible.

A molecular model is established through the definition of force or the potential energy of interaction (PRASANTH; KAKKASSERY, 2008). The force of interaction

$F(r)$ and the potential energy of interaction $\phi(r)$ between two spherical non-polar molecules is a function of the intermolecular separation $r$ as shown in Figure. 2.2. These two are simply related as:

$$F_r = -\frac{d\phi}{dr}, \ \phi(r) = \int_r^\infty F(r)dr \qquad (2.13)$$

In selecting the form of an intermolecular potential to use in calculations, one must consider two factors: the degree of realism desired and the numerical difficulties associated with the manipulation of the function. For the DSMC applications, the first interaction potential used was the rigid impenetrable sphere model due to its simplicity. This empirical intermolecular potential functions may be expressed as:

$$\phi(r) = \begin{cases} \infty & \text{if } r < d\,, \\ 0 & \text{if } r > d\,. \end{cases}$$
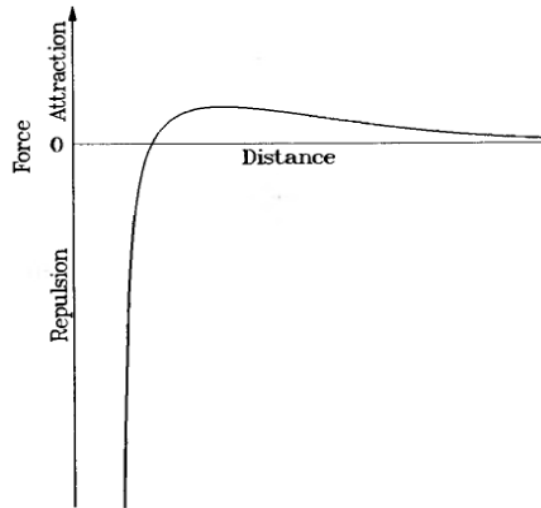


Figure 2.2 - Typical intermolecular force field.
Source: Bird (BIRD, 1994).

This potential function represents rigid impenetrable spheres of a diameter $d$. Due to its simplicity, it is frequently used for exploratory calculations. It works on the simple premise that interactions occurs only when molecules come into actual phys-

ical contact. Through this model is handled very conveniently but it is a not very realistic model. It is well know that two molecules attract each other when they are far apart and repel each other when they come close together, as illustrated in Fig. 2.2. However, for most applications, except for extremely low temperatures, the attractive component of the interaction potential may be neglected. This simplification gives the mathematically and computationally convenient inverse power law (IPL) potential or the point centers of repulsion model, which is expressed as:

$$\phi(r) = K r^{-\zeta} \tag{2.14}$$

The index of repulsion $\zeta$ for most molecules has a value between 9 and 15 and $K$ is a constant. This function is useful in exploratory calculations in which a differentiable potential function is needed.

The IPL model becomes deficient at low temperatures where the attractive force dominates. Therefore, it becomes desirable to introduce models based on potentials with both attractive and repulsive components like the Lennard-Jones potential, which is expressed as:

$$\phi(r) = 4\varepsilon \left[ \left( \frac{\sigma}{r} \right)^{12} - \left( \frac{\sigma}{r} \right)^{6} \right] \tag{2.15}$$

The constant parameters $\sigma$ and $\varepsilon$ (which have dimensions of length and energy, respectively) depend on the characteristics of the chemical species of the colliding molecules; $\sigma$ is that value of $r$ for which $\phi(\text{r}) = 0$ and $\varepsilon$ is the maximum energy of attraction, which occurs at $r = 2^{1/6}\sigma$. At large separations ($r >> \sigma$), the inverse sixth-power attractive component is dominant, and the molecules are attracted from one to another with a force proportional to the inverse seventh-power of separation. When separations are small ($r << \sigma$), the inverse twelfth-power repulsive component is dominant, and the molecules are repelled from one to another with a force proportional to the inverse thirteenth-power of separation. The Lennard-Jones attractive-repulsive potential is adequate for a number of non-polar molecules. In the case of polar molecules, strong electrostatic interaction leads to anomalous behavior with respect to the Lennard-Jones potential. This electrostatic contribution

has been proven to be proportional to the inverse third-power of the intermolecular separation. The Stockmayer potential combines such a term with the Lennard-Jones potential to describe the interaction between polar molecules and is expressed as,

$$\phi(r) = 4\varepsilon \left[ \left( \frac{\sigma}{r} \right)^{12} - \left( \frac{\sigma}{r} \right)^{6} - \delta \left( \frac{\sigma}{r} \right)^{3} \right] \tag{2.16}$$

where the constant $\delta$ measures the polarization of a substance.

Among all the molecular models used in the collision routine of the DSMC method, for the purpose of this study, only the VHS model will be described. The VHS model has been the most popular molecular model used in DSMC applications. It has been recommended (BIRD, 1994) for engineering calculations, since for the most flows of interest, the variation in the collision cross section has a far greater influence on the structure of a flow than any variation in the molecular scattering characteristics.

### 2.2.3.1 Variable Hard-Sphere (VHS) model

As the temperature of the gas increases, both its relative molecular velocity and its translational kinetic energy also increases. It has been observed that as these quantities increase, the effective total collision cross-section decreases and this rate of decrease can be directly related to the change of coefficient of viscosity with temperature. Whereas, the rigid interaction potential does not capture the variation of viscosity with temperature accurately, the IPL interaction potential captures the rate to a reasonable accuracy at high temperatures (PRASANTH; KAKKASSERY, 2008). The IPL interaction potential or the point centre of repulsion model is described by a Force field $F(r)$ of the form:

$$F(r) = \frac{k}{r^{\eta}} \tag{2.17}$$

where $k$ is the constant and $\eta$ is the exponent in the IPL.

This is a very useful interaction potential at high temperatures. For any finite value of the exponent, the force field extends to infinity and the total cross-section diverges. For a fixed value of the relative molecular velocity, the total cross-section $\sigma_T$ is

obtained (SHEN, 2006) as:

$$\sigma_T = \pi W_m{}^2 \cdot \left(\frac{k}{2E_t}\right)^{\frac{2}{\eta-1}}$$
(2.18)

where $W_m$ is a constant and $E_t$ is the relative translational energy given by $E_t = 0.5 m_r c_r{}^2$, where $m_r$ calculated as $m_1 m_2/(m_1 + m_2)$, is the reduced molecular mass of two colliding molecules of mass $m_1$ and $m_2$.

The value of the constant $W_m$ is arbitrary and, hence this expression is not suitable for setting the effective collision frequency or the mean free path. Thus, in the direct simulation of gas flows, though the IPL model was in use, it had to be replaced and researchers had to fall back to the rigid-sphere molecular model, which has a constant $\sigma_T$. However, as can be deduced from Eq. 2.18, in a realistic situation, $\sigma_T$ is hardly a constant. It is inversely proportional to $c_r^{4/(\eta-1)}$. This led to the introduction of the variable hard-sphere model introduced by Bird (BIRD, 1981). This model incorporates the hard-sphere scattering law for collisions, but it cross-section is inversely proportional to the relative translational energy in the collision to the power $2/(\eta-1)$. Hence, for an equilibrium gas, the average total cross-section is related to the temperature as:

$$\bar{\sigma_T} \propto T^{-2/(\eta-1)}$$
(2.19)

The VHS model combines a finite cross-section with a realistic temperature exponent of the coefficient of viscosity. It has permitted the definition of a mean free path and a Knudsen number (BIRD, 1983) that accounts for the real temperature exponent of the coefficient of viscosity. The deflection angle is given by Eq. 2.20, where $b$ is the impact parameter and $d$ is the molecule diameter. The diameter $d$ is a function of relative translational energy and varies according to Eq. 2.21.

$$\chi = 2cos^{-1}\left(\frac{b}{d}\right)$$
(2.20)

$$d = d_{ref} \left( \frac{c_{r,ref}}{c_r} \right)^{2/(\eta-1)} \tag{2.21}$$

In the VHS model, the reference values $\sigma_{T,ref}, d_{ref}, c_{r,ref}$ and $E_{t,ref}$ are introduced, which define the VHS model as:

$$\frac{\sigma_T}{\sigma_{T,ref}} = \left( \frac{d}{d_{ref}} \right)^2 = \left( \frac{c_r}{c_{r,ref}} \right)^{-2\zeta} = \left( \frac{E_t}{E_{t,ref}} \right)^{-\zeta} \tag{2.22}$$

where $\sigma_{T,ref}$ and $d_{ref}$ are the values of the total collision cross-section and the molecular diameter when the relative velocity is $c_{r,ref}$ and the corresponding energy is $E_{t,ref}$. The index $\zeta$ is the power of $E_t$ in Eq. 2.18, i.e, this power law for variation of diameter with $c_r$ corresponds to the power law for the variation of $\sigma_T$ with $c_r$, as given by Eq. 2.18. In addition, it also permits for a variation of the coefficient of viscosity with temperature, in much the same way as that in the IPL model. This allows the cross-section in the VHS model to be determined from the viscosity coefficient. Incidentally, the viscosity cross-section and the momentum cross-section for this model have been found to be related to the total collision cross-section in the same way as they are related in the rigid-sphere model. These cross-sections are expressed by the following expressions:

$$\sigma_u = \frac{2}{3}\sigma_T = \frac{2}{3}\pi d^2 \tag{2.23}$$

$$\sigma_M = \sigma_T = \pi d^2 \tag{2.24}$$

Hence for this model, evaluating Eq. 2.4, the coefficient of viscosity can be written in the following form (BIRD, 2013):

$$\mu = \frac{\frac{15}{8}\sqrt{\pi mk}(4k/m)^\xi T^{1/2+\xi}}{\Gamma(4-\xi)\sigma_{T,ref}c_{r,ref}^{2\xi}} \tag{2.25}$$

In this equation, the coefficient of viscosity is proportional to $T$ to the power $\omega = (1/2 + \xi)$, which is defined as the temperature index of the coefficient of viscosity. By adjusting the value of $\xi$, the correct dependence of $\mu$ on $T$ can be obtained by observing that,

$$\xi = \frac{2}{\eta - 1}$$
$$\omega = \frac{1}{2}\frac{\eta + 3}{\eta - 1}$$

(2.26)

For the hard-sphere molecule, $\omega = 1/2$, $\eta \to \infty$, and $\xi = 0$, and for the Maxwellian molecule, one has $\omega = 1$ and $\xi = 1/2$ (BIRD, 1981). The Maxwellian model finds wide application in analytical studies because it simplifies a lot of the mathematical calculations. However, the viscosity of a gas for Maxwellian molecules is linearly proportional to the temperature and, hence it is unrealistic. The hard-sphere model with $\eta \to \infty$ is the most hard molecule and the Maxwellian molecule is the most soft among all molecular models (PRASANTH; KAKKASSERY, 2008).

For the unrealistic hard sphere molecular model, which the molecules has a fixed diameter $d$ and the collision cross-section is $\sigma = \pi d^2$, the mean free-path in a equilibrium gas of number density $n$ is given by:

$$\lambda = \frac{1}{\sqrt{2}n\sigma}$$

(2.27)

where $n$ is the number density, and $\sigma$ is the hard sphere collision cross section. In this sense, the Chapman-Enskog result for the coefficient of viscosity in a hard sphere gas, at a temperature $T$, was defined by:

$$\mu = \frac{5m}{16}\frac{(\pi R T)^{1/2}}{\sigma}$$

(2.28)

The cross section may be eliminated from Eqs.2.27 and 2.28 to give the standard result:

$$\lambda = \frac{16\mu}{5} \frac{(2\pi RT)^{-1/2}}{\rho} \qquad (2.29)$$

where $\rho = nm$ is the gas density.

The inconsistency in the above procedure is that the coefficient of viscosity has a fixed temperature exponent of $1/2$, while the real gas coefficient of viscosity yields to $\mu \propto T^{\omega}$ where $\omega$ is generally in the range 0.6 - 0.9. Therefore, as an alternative scheme, a consistent definition of the mean free path obtained through the variable cross-section hard sphere (VHS) was introduced by Bird (BIRD, 1994). The mean free path in a VHS is now defined by:

$$\lambda = \frac{2\mu}{15} \frac{(7 - 2\omega)(5 - 2\omega)(2\pi RT)^{-1/2}}{\rho} \qquad (2.30)$$

which can account for the real gas temperature exponent of the coefficient of viscosity.

### 2.2.4 Larsen-Borngakke (LB) Model

A phenomenological model is defined as one that reproduces the overall effects in a gas flow of some physical feature of the real molecules without the explicit incorporation of that feature. The phenomenological models superimpose the energy exchange between the internal and translational energy upon an otherwise monatomic model. This approach is based on assumption that for determining the macroscopic flow properties, the finer details of the collision process may be ignored. The models are therefore spherically symmetric and the phenomenological process allows the specification of the requisite number of rotational and vibrational degrees of freedom that leads to equipartition between these modes. There must also be exact equipartition between rotational, vibrational and translational modes, and, the distributions functions of each quantity must be the local Maxwellian (PRASANTH; KAKKASSERY, 2008), when the gas is in equilibrium.

The most widely used phenomenological model is that of Larsen-Bornakke (LB) (BORGNAKKE; LARSEN, 1975) model, in which a detailed balance is ensured by the selection of the post-collision values directly from the Maxwellian distributions. The LB procedures set the distribution of post-reaction internal energies to values that

satisfy the detailed balance principle. Therefore, the procedures maintain the equilibrium distribution of all modes and the establishment of equilibrium for each mode automatically leads to equilibrium between modes and to equipartition (BIRD, 2013). The method was developed originally to simulate the energy transfer between translational and rotational modes. Later, it was also extended to vibration-translation energy transfer. The main assumptions of the model are (1) post-collisional internal and relative translational energies are simulated in accordance with the local equilibrium distribution functions; (2) some fractions $1/Z_r$ and $1/Z_v$ of collisions are assumed to be rotationally and vibrationally inelastic. $Z_v$ and $Z_r$ are the vibrational and rotational relaxation collision numbers, respectively; and (3) rotational and vibrational energy are continuous. This is a valid assumption for translation because of enormous number of available states, and it is a good approximation for the rotational mode at normal or higher temperature (BIRD, 2013). For the purpose of the present investigation, the collision numbers was implemented to have a temperature dependence as defined by Bird (BIRD, 2008) for vibration and Boyd (BOYD, 1990) for rotation.

The LB model is in itself an inelastic collision model and the issue of inelasticity on polyatomic molecules is handled very easily using this model. All molecular interactions that are affected through this model are inherently inelastic in nature. However, if all collisions are implemented as inelastic collisions, then the relaxation rate, which is the rate at which the gas tends to equilibrium, would be too quick as compared to the physical relaxation process. Hence, this rate is controlled by regarding a fraction of the collisions as elastic. In general, the relaxation time $\tau_i$, which is usually several times larger than the collision time, is introduced to characterize the relaxation rate given by,

$$\tau_i = \frac{Z_i}{\nu} \tag{2.31}$$

where $Z_i$ is called the relaxation collision number and $\nu$ is the collision frequency (PRASANTH; KAKKASSERY, 2008).

The central idea of the LB model is to assume that the kinetic energy and internal energy follow the law of conservation of energy. The internal energy after collision is sampled according to the equilibrium distribution of the combination of the kinetic energy and internal energy. A general LB distribution function for the division of

post-collision energy between the energy modes has been developed by Bird (BIRD, 1994).

Consider a collision between a molecule of species 1 and a molecule of species 2. Also, consider the parameter $\Psi$ as the average of the degree of freedom of the two molecules. The number of degrees of freedom associated with the relative translational energy is $5 - 2\omega_{12}$ and the total average is as following;

$$\Psi = 5/2 - \omega_{12} + \zeta_{r,1}/2 + \zeta_{r,2}/2 + \zeta_{v,1}/2 + \zeta_{v,2}/2 \tag{2.32}$$

Let $\Psi_a$ be one or more of the terms on the right hand side of Eq.2.32 and let $\Psi_b$ be the remaining terms that are participating in the partitioning of energy. The energy that is assigned to the first mode or group of mode is $E_a$, and $E_b$ is that to be assigned to the second one. The sum of these energies is called the collision energy $E_c$ ($E_c = E_a + E_b$) even though it generally does not include the energy in all the modes of the two molecules. The collision energy is a known quantity and is a constant in the energy distribution process.

### 2.2.4.1  Rotational Energy Exchange

The rotational mode is usually simulated using a physics approach in which the rotational energy, $\epsilon_r$, is assumed to be continuously distributed at equilibrium to a Boltzmann distribution:

$$f(\epsilon_r)d\epsilon_r = \frac{1}{\Gamma(\zeta/2)} \left(\frac{\epsilon_r}{kT}\right)^{\zeta/2-1} exp\left(-\frac{\epsilon_r}{kT}\right) d\left(\frac{\epsilon_r}{kT}\right) \tag{2.33}$$

where $\zeta$ is the number of rotational degrees of freedom (2 for diatomic molecules and 3 for polyatomic molecules), $k$ is the Boltzmann's constant, and $T$ is the temperature.

When a particle representing a molecule is injected into a DSMC computation, it is given an initial rotational energy sampled from Eq. 2.33. The rotational energy of the particle can change through collisions with other particles and through collisions with solid surfaces. In a continuum analysis of rotational energy exchange, the rotational relaxation rate is usually employed:

$$\frac{de_r}{dt} = \frac{e_r^* - e_r}{\tau_r} \tag{2.34}$$

where $e_r$ is the specific rotational energy, $e_r^*$ is the equilibrium value at temperature $T$, and $\tau_r$ is the rotational relaxation time. The equivalent DSMC procedure involves evaluating a probability of rotational energy exchange for each collision followed by appropriate energy exchange mechanics for those collisions that lead to rotational relaxation. The average probability of rotational energy exchange is:

$$\langle P_r \rangle = \frac{1}{Z_r} = \frac{\tau_t}{\tau_r} = \frac{1}{\tau_r \nu} \tag{2.35}$$

where $Z_r$ is the rotational collision number, $\tau_t$ is the translational relaxation time that is equal to the inverse of the collision frequency $\nu$. Boyd (BOYD, 1990a) developed the following instantaneous rotational energy exchange probability based on Parker's model (PARKER, 2004) for the rotational collision number related to the VHS collision model:

$$P_r = \frac{1}{(Z_r)_\infty} \left( 1 + \frac{\Gamma(\zeta + 2 - \omega)}{\Gamma(\zeta + 3/2 - \omega)} \left( \frac{kT^*}{\epsilon_{tot}} \right)^{\frac{1}{2}} \frac{\pi^{\frac{3}{2}}}{2} + \frac{\Gamma(\zeta + 2 - \omega)}{\Gamma(\zeta + 1 - \omega)} \left( \frac{kT^*}{\epsilon_{tot}} \right) \left( \frac{\pi^2}{4} + \pi \right) \right) \tag{2.36}$$

where $\epsilon_{tot}$ is the total collision energy, defined earlier by $E_c$ (the sum of the translational collision energy and the rotational energy), $T^*$ is the characteristic temperature of the intermolecular potential, and $(Z_r)_\infty$ is the limiting value.

After evaluation of the rotational energy exchange probability, a random number is used to decide whether the collision leads to energy exchange. For those collisions involving rotational energy exchange, the LB model (BORGNAKKE; LARSEN, 1975) is employed to assign new post-collision rotational energies. The LB model assumes local thermodynamic equilibrium to sample the fraction of the total collision energy due to rotation, $\epsilon_r / \epsilon_{tot}$, from the following expression (BOYD, 2014):

$$\frac{P}{P_{max}} = \left( \frac{\zeta + 1 - \omega}{2 - \omega} \left( 1 - \frac{\epsilon_r}{\epsilon_{tot}} \right) \right)^{2 - \omega} \left( \frac{\zeta + 1 - \omega}{\zeta - 1} \left( \frac{\epsilon_r}{\epsilon_{tot}} \right) \right)^{\zeta - 1} \tag{2.37}$$

Once the new rotational energy is assigned, the remaining energy is the new translational energy and hence determines the new post-collision relative velocity. The regular DSMC collision mechanics is then performed to calculate the velocities of the colliding particles.

Lumpkin (LUMPKINIII et al., 1991) noted that an additional correction must be applied to any DSMC rotational energy exchange probability in order to make Larsen-Borgnakke exchange mechanics consistent with the continuum rotational relaxation equation, Eq. 2.34. The form of the correction is (BOYD, 2014):

$$P_{particle} = P_{continuum} \left( 1 + \frac{2\zeta}{4 - 2\omega} \right) \qquad (2.38)$$

that is usually close to a factor of two.

While the rotational energy is usually simulated in the classical limit, a quantum mechanical approach for DSMC has also been developed by Boyd (BOYD, 1993). Unlike rotational relaxation, a quantum mechanical approach is almost always employed for simulation of vibrational energy relaxation in hypersonic flows. A quantized vibrational energy exchange model corresponding to the classical Larsen-Borgnakke (LB) approach was formulated by Bergemann and Boyd (BERGEMANN; BOYD, 1994).

### 2.2.4.2 Vibrational Energy Exchange

The LB model is applied to vibrational modes through a quantum approach that assigns discrete vibrational levels to each molecule. A discrete approach is required because the vibrational levels are widely spaced and hence a continuous distribution for the vibrational energy may not be appropriate. It is important to recall that a monatomic molecules have no rotational or vibrational modes, but they do have electronic mode (BIRD, 2013). However in hypersonic flows, generally the electronic modes are ignored, as in the case of the CFD studies (BOYD, 2008).

Consider the quantum case in which the energy in a particular internal mode of a molecule is restricted to that of the discrete states $\varepsilon_i$, where $i = 0$ to $j$. The zero point energy has no effect and can be ignored, so that $\varepsilon_0 = 0$. Now consider the LB redistribution between the translational mode as group $b$ and a quantized internal mode with two degrees of freedom of molecule 1 as a group $a$. In this special case of the assignment of energy to a single internal mode with two degrees of freedom, one has:

$$f \left( \frac{E_a}{E_c} \right) = (5/2 - \omega_{12}) \left( 1 - \frac{E_a}{E_c} \right)^{3/2 - \omega_{12}} \qquad (2.39)$$

where $\omega$ is the viscosity-temperature index.

The representative value of $E_a$ that corresponds to the random number $R_F$ is:

$$E_a = E_c \left(1 - R_F^{1/(5/2-\omega_{12})}\right) \qquad (2.40)$$

This can be applied directly to the rotational energy of a diatomic molecule. In this scenario, Eq. 2.39 can then be applied with the energy $E_c$ equal to the sum of the pre-collision translational energy and the energy of the pre-collision state. $E_c$ is constant in the redistribution and the probability of post-collision state $i^*$ is proportional to $(1 - \varepsilon_{i^*}/E_c)^{3/2-\omega_{12}}$. The maximum probability is that of the ground state, so that the ratio of the probability to the maximum probability is:

$$\frac{P}{P_{max}} = \left(1 - \frac{\varepsilon_{i^*}}{E_c}\right)^{3/2-\omega_{12}} \qquad (2.41)$$

The acceptance-rejection procedure may be applied to this probability ratio in order to select the post-collision state of molecule 1. This selection process is applied to potential states that are chosen uniformly from the ground state to the highest state with energy below $E_c$. Note that the selection procedure involves states rather than levels and the degeneracy $g_k$ of a level $k$ must be taken into account. The spacing of the energy levels is not uniform but, in the the case of vibration, most applications employ the simple harmonic model that assumes uniformly spaced levels (BIRD, 2013):

$$\varepsilon_{v,i} = ik\Theta_v \qquad (2.42)$$

where $\Theta_v$ is the characteristic vibrational temperature.

In this sense, Eq. 2.41 then becomes:

$$\frac{P}{P_{max}} = \left(1 - \frac{i^* k\Theta_v}{E_c}\right)^{3/2-\omega_{12}} \qquad (2.43)$$

There is sufficient evidence that the LB is a statistical model based on the relaxation concept, which is suitable for a Monte Carlo simulation scheme. Typically, the model formulation specifies the number of internal degrees of freedom, the collision probability and a post-collision probability, such as the angular distribution of the relative velocity. The model has a high degree of flexibility and requires slightly

more computing time per collision than the hard-sphere gas of a monatomic gas. It satisfies all the requirements for a successful phenomenological model (PRASANTH; KAKKASSERY, 2008).

### 2.2.5 Relaxation Rate

In a gas of colliding molecules, energy is continually being transferred between the various internal modes. These collisions tend to push the internal energy distributions toward their equilibrium state, so the collision number $Z$ of an energy mode is the number of collisions required to bring that mode into equilibrium. Each internal mode has a separate collision number, which in general is classified as following (BOYD, 1990b):

$$Z_t < Z_r < Z_v \qquad (2.44)$$

where the subscripts $t$, $r$ and $v$, denotes translational, rotational and vibrational modes, respectively.

The collision procedure for a particular mode is applied in $1/Z$ of the relevant collisions. The relaxation collision numbers are set as part of the data for each molecular species. These collision numbers are often an arbitrary function of the temperature. However, it has been uncertain whether the relevant DSMC procedures can be based on effective collision temperatures, or whether they must be based on the macroscopic temperature.

The molecules in an intermolecular collision are unaware of the macroscopic temperature of the gas and all DSMC procedures should be based entirely on the microscopic properties of these molecules. To achieve this, procedures that employ temperature dependent physical data generally introduce a "collision temperature" that is based on the relative translational energy and some proportion of the internal energy of the molecules in the collision. This collision temperature is not uniquely defined and the procedures must satisfy physical constrains such as the eventual equipartition of energy between the modes as well as the establishment of the equilibrium distribution and compositions.

The DSMC procedures for intermolecular collisions employ a cross-section that is a function of the relative translational energy. The LB model for rotational and vibrational excitation assumes that only a fraction of the molecules is inelastic. An attempt was made to make the model physically more realistic by making a frac-

tion energy assignment in every collision. However, this led to violation of detailed balancing and there appears to be no alternative to an "inelastic fraction" that is based on the relevant relaxation collision number. If this number is temperature dependent, it is necessary to either introduce a collision temperature or employ the macroscopic temperature. The use of the collision temperature (BIRD, 1994) does not led to any problems with the classical models and the appropriate inelastic fraction is generally close to the inverse of the collision number (BIRD, 2008).

### 2.2.5.1 Rotational Relaxation Rate

In the present investigation, the relaxation rotation collision number was set to be energy dependent as introduced by Boyd (BOYD, 1990)(BOYD, 1990a). The following continuum expression for the rotational collision number was obtained by Parker (PARKER, 2004):

$$Z_r = \frac{(Z_r)_\infty}{1 + \frac{\pi^{3/2}}{2}\left(\frac{\Theta^*}{T_{coll}}\right)^{1/2} + \left(\frac{\pi^2}{4} + \pi\right)\frac{\Theta^*}{T_{coll}}} \tag{2.45}$$

where $\Theta^*$ (characteristic temperature of the intermolecular potential), and $(Z_r)_\infty$ (the limiting value) are constants. The values of $(Z_r)_\infty$ and $\Theta^*$ are chosen in order to obtain the best correspondence between Parker's expression and the results of Lordi and Mates (LORDI; MATES, 1970). In their analysis, Lordi and Mates (LORDI; MATES, 1970) found that nonequilibrium between the translational and rotational modes affects the rotational collision number. In order to consider the behavior of the model under nonequilibrium conditions it is useful to regard the temperature $T_{coll}$ as the weighted average of the translational and rotational temperatures. It has been shown by Boyd (BOYD, 1990b) that Eq. 2.45 may be reproduced in a discrete particle simulation by assuming that the probability of energy exchange is a function of the relative velocity of collision $c_r$ (BOYD, 1990a).

### 2.2.5.2 Vibrational Relaxation Rate

Bergemann and Boyd (BERGEMANN; BOYD, 1994) introduced the quantum model that has proved to be vastly superior to the classical model. However, with the collision temperature that had employed in the classical model, equipartition was not achieved. This led to the statement that vibrational equipartition could be achieved with the quantum model only if the vibrational collision number was based on the macroscopic temperature. The vibrational collision number is extremely dependent on the temperature and the use of a uniform value in a DSMC cell, means that

significant effects due to the distribution of collision energies within that cell are not taken into account. This problem has been solved by considering the collision temperature quantized in the same fashion as the vibrational energy and not otherwise dependent on the collision energy. With this procedure, exact equipartition is achieved (BIRD, 2008). The definition of the collision temperature based only on the relative translational energy in the collision follows as (BIRD, 2013):

$$T_{coll} = \frac{m_r c_r^2}{(5 - 2\omega)k} \qquad (2.46)$$

However the LB energy redistribution is based on the sun of the translational energy and a single internal mode. So the appropriate collision temperature based on $LB$ energy redistribution is given by:

$$T_{coll} = \frac{1/2 m_r c_r^2 + \varepsilon_{int}}{(5/2 + \overline{\zeta_{int}} - \omega)k} \qquad (2.47)$$

The definition in Eqs. 2.47 is preferred because temperature is a measure of energy and, to define a temperature, the energy is divided by the product of the Boltzmann constant and the "effective" number of degrees of freedom that takes the degree of excitation into account. However, the LB selection is based on the physical degrees of freedom, irrespective of the degree of excitation, and, for a partially excited mode, Eq. 2.47 leads to a temperature that is too low (BIRD, 2013). It was shown by Bird (BIRD, 2002)(BIRD et al., 2011) that equipartition is achieved if the local collision energy is quantized in the same way as the energy of the relevant vibrational mode. It was showed that the collision temperature should be employed when setting all temperature dependence parameters (BIRD, 2008).

Consider the binary collision of two polyatomic DSMC simulating particles $P$ and $Q$. Each particle in the collision pair is considered in turn and the following steps are undertaken (SCANLON et al., 2011):

- Calculate the pre-collision energy of particle $P$, $E_{c,P}$, which is the sum of the relative translational energy between $P$ and $Q$ and the vibrational energy of particle $P$ is:

$$E_{c,P} = E_{t,PQ} + E_{v,P} \qquad (2.48)$$

- Determine the maximum possible quantum vibrational level for the particle $P$, $i_{max,P}$, following the collision:

$$i_{max,P} = \left\lfloor \frac{E_{c,P}}{k\Theta_{v,P}} \right\rfloor \qquad (2.49)$$

where $k$ is the Boltzmann constant and $\Theta_{v,P}$ is the characteristic vibration temperature. The brackets in the Eq. 2.49 indicate that $i_{max,P}$ is "quantized" by truncating its value to an integer.

- A desired feature in the DSMC methodology is that numerical process should be not dependent on any macroscopic information. The two molecules in a collision have no knowledge of the overall macroscopic temperature, and, if highly non-equilibrium flows are to be resolved sufficiently. The procedures for energy redistribution in a collision should be based entirely on the energies and impact parameters associated with that collision. In order to adhere to this microscopic principle, a "quantized collision temperature", $T_{coll}$ is defined which is based on $E_{c,P}$ as:

$$T_{coll,P} = \frac{i_{max,P}\Theta_{v,P}}{7/2 - \omega_P} \qquad (2.50)$$

The Millican-White (MILLIKAN; WHITE, 2004) theory predicts that the product of the pressure and the vibrational collision time is proportional to the exponential of a constant times the minus one third power of the temperature. This leads (BIRD, 1994) to a vibrational collision number defined as:

$$Z_v = (C_1/T^\omega)exp(C_2 T^{-1/3}) \qquad (2.51)$$

where $C_1$ and $C_2$ are constants. The values of the constants that best fit to experimental data were provided for typical gases. Nevertheless, a problem with Millikan-White data is that the collision number goes to a nonphysical value less than unity before the dissociation temperature is reached. There is a strong case for setting the vibrational collision number to unity at the characteristic temperature of dissociation $\Theta_d$, and it is then possible to specify the vibrational collision number through a single value $Z_{v,ref}$ at the reference temperature $T_{ref}$. The expression for the vibrational collision number is then (SCANLON et al., 2011) (BIRD, 2008) (BIRD, 2013):

$$Z_v = \left(\frac{\Theta_d}{T_{coll,P}}\right)^\omega \left[Z_{ref}\left(\frac{T_{ref}}{\Theta_d}\right)^\omega\right]^{\left[\left(\frac{\Theta_d}{T_{coll,P}}\right)^{1/3}-1\right]/\left[\left(\frac{\Theta_d}{T_{ref}}\right)^{1/3}-1\right]} \tag{2.52}$$

where $\Theta_d$ is the characteristic temperature of dissociation, $\omega$ is the temperature exponent of viscosity, $Z_{ref}$ is a reference vibrational collision number, evaluated at an arbitrary reference temperature $T_{ref}$. The value of $T_{ref}$ should be representative of the range of temperatures expected in the application.

### 2.2.6 The Number of Degrees of Freedom

The DSMC method is able to simulate monatomic rarefied gas flows very well. Polyatomic rarefied gas flows, however, in which the gas molecule are able to transfer energy among translational, rotational and vibrational degrees of freedom, cannot be accurately predicted using the simple collision models. For any molecule, monatomic or polyatomic, relative translational energy has three degrees of freedom. Whereas, monatomic molecules have only translational degrees of freedom, polyatomic molecules have rotational and vibrational degrees of freedom in addition to the three translational degrees of freedom. The post-collisional energy in the LB model is divided according to the local equilibrium distribution functions that means that energies of modes are determined by the number of degrees of freedom of those models. For VHS and VSS models, the probability of collision is proportional to $c_r^{1-2\xi}$, and the number of translational degrees of freedom of colliding molecules is therefore $\zeta_t = 4 - 2\xi$ ($\xi$ is given by Eq. 2.26). For rotational energy, the number of degrees of freedom $\zeta_r$ is a function of the number of atoms $n_a$ (PRASANTH; KAKKASSERY, 2008), given by :

$$\zeta_r = \begin{cases} 0 & n_a = 1\,, \\ 2 & n_a = 2\,, \\ 3 & n_a \geq 3\,. \end{cases}$$

The number of effective vibrational degrees of freedom and the vibrational energy $E_v$ of diatomic molecules, can be derived from the Simple harmonic oscillator (SHO) approximation. In this sense, vibrational energy may be expressed by (BIRD, 1994):

$$E_v = \frac{k\Theta_v}{exp(\Theta_v/T) - 1} \tag{2.53}$$

where $k$ is the Boltzmann constant, $\Theta_v$ is the characteristic temperature of vibration and $T$ is the temperature. The vibrational degrees of freedom $\zeta_v$ is a function of the local temperature $T$ and the species characteristic vibrational temperature $\Theta_v$. Equipartition principle gives the number of effective degrees of freedom for vibrations as was also defined by Bird (BIRD, 1994),

$$\zeta_v = \frac{2\Theta_v/T}{exp(\Theta_v/T) - 1} \tag{2.54}$$

This approximation may also be applied to the polyatomic molecules. In this case $\zeta_v$ is the sum over all vibrational modes. Considering completely inelastic collision of molecules with the energy exchange between translational, rotational and vibrational modes, the total energy of colliding pairs is given by:

$$E_c = E_t + E_{i1} + E_{i2} \tag{2.55}$$

where $E_t = m_r c_r^2/2$ is the translational energy, $E_{i1,2} = E_{r_{1,2}} + E_{v_{1,2}}$ is the internal energy (rotational and vibrational) of molecules 1 and 2. The equilibrium relative translational energy distribution is:

$$f_{E_t} \sim E_t^{1-\xi} exp\left(-\frac{E_t}{kT}\right) \tag{2.56}$$

The equilibrium internal energy distribution function is:

$$f_{E_i} \sim E_i^{\bar{\zeta}-1} exp\left(-\frac{E_i}{kT}\right) \tag{2.57}$$

where $\bar{\zeta} = (\zeta 1 + \zeta 2)/2$ is the average number of internal degrees of freedom of pair.

The procedure of energy redistribution includes three main steps as following:

- step 1: Translational/internal energies.

As the joint distribution function of translational and internal energies is:

$$f_{E_{ti}} \sim E_t^{1-\xi} E_i^{\bar{\zeta}-1} exp \left( -\frac{E_t + E_i}{kT} \right) = E_t^{1-\xi} (E_c - E_t)^{\bar{\zeta}-1} exp \left( -\frac{E_c}{kT} \right)$$
(2.58)

and $E_c$ is a constant, then the relative post-collision translational energy $E_t'$ is sampled from the probability density:

$$E_t^{1-\xi} (E_c - E_t)^{\bar{\zeta}-1}$$
(2.59)

The post-collision internal energy is $E_i' = E_c - E_t'$.

- step 2: Molecule 1/ Molecule 2 internal energies. Joint equilibrium distribution function of internal energies of pair is proportional to

$$E_{i1}^{\frac{\zeta_1}{2}-1} E_{i2}^{\frac{\zeta_2}{2}-1} exp \left( -\frac{E_i}{kT} \right)$$
(2.60)

and the post-collision internal energy $E_{i1}'$ of a molecule 1 is sampled from the probability density:

$$E_{i1}^{\frac{\zeta_1}{2}-1} (E_i' - E_{i1})^{\frac{\zeta_2}{2}-1}$$
(2.61)

for the molecule 2: $E_{i2}' = E_i' - E_{i1}'$

- step 3: Rotational/vibrational energies.

For diatomic molecules their post-collisional rotational and vibrational energies are:

$$E_{r1,2}' = \frac{2}{2 + \zeta_{v1,2}} E_{v1,2}', \qquad E_{v1,2}' = E_{i1}' - E_{r1,2}'$$
(2.62)

The probability of rotational inelastic collision is $1/Z_r$ and vibrational inelastic collision is $1/Z_v$.

## 2.2.7 Boundary Conditions

The most important outcome from many DSMC analysis of hypersonic flows is the determination of the properties at the vehicle surface, and in particular the aerodynamic forces and moments, and the convective heat transfer. The surface properties are of course very sensitive to the model assumed in DSMC for gas-surface interaction (BOYD, 2014). Modeling the interaction of gas molecules with a solid surface

plays an important role in the DSMC simulation. But there is no model of gas-surface interaction that is adequate over a wide range of factors for all combinations of gases and surfaces. For example (PIEKOS, 1995) (XUE et al., 2000), some analytical and numerical simulations are based on the assumption of diffuse reflections with full thermal and momentum accommodation. The fully diffuse reflection is a common gas-surface interaction in which the particles reflect from the surface with new velocity components that are sampled from Maxwellian distributions characterized by the wall temperature (note that the velocity component normal to the surface is sampled from a biased Maxwellian distribution)(BOYD, 2014). Another method employed is the Cercignani-Lampis-Lord (CLL) gas-surface model (LORD, 1991b). The CLL model is a more sophisticated method and have a stronger theoretical basis, such as using a reciprocity relation, and offers more control through use of additional parameters (BOYD, 2014). Fig. 2.3 displays a schematic comparison of the Maxwell reflection model and the CLL reflection model. The CLL model has also been extended for covering diffuse scattering with partial energy accommodation. In addition, for simulating the accommodation of vibrational energy of a diatomic molecule modeled as simple harmonic oscillator (LORD, 1991a), and an anharmonic oscillator (LORD, 1994).

In the calculations of aerodynamic forces by the DSMC method, it is necessary to setting the velocity distributions functions for the molecules reflected from the surface. A simplified representation of this function is used, which must take into account the major features of gas-surface interaction, which have been revealed in experiments (force action and angular distribution of escaped molecules), on the one side, and it must be simple enough in application, on the other side. In this sense, one of the oldest and most widely used distribution functions for the reflected molecules is due to Maxwell, which proposed two models – specular and diffuse reflection – for the interaction of an equilibrium gas with a solid surface that maintain equilibrium.

In the diffuse model, the particle internal energies are also sampled from the appropriate equilibrium distribution, such as the Eq. 2.33 for rotation, using the wall temperature (BOYD, 2014). Also, the velocity of each molecule after reflection is independent of its velocity before reflection. However, the velocities of the reflected molecules as a whole are distributed in accordance with the half-range Maxwellian or equilibrium for the molecules that are directed away from the surface. Equilibrium diffuse reflection requires that both the surface temperature and the temperature associated with the reflected Maxwellian gas be equal to the gas temperature. A gas generally has a velocity component parallel to a surface, and this means that the
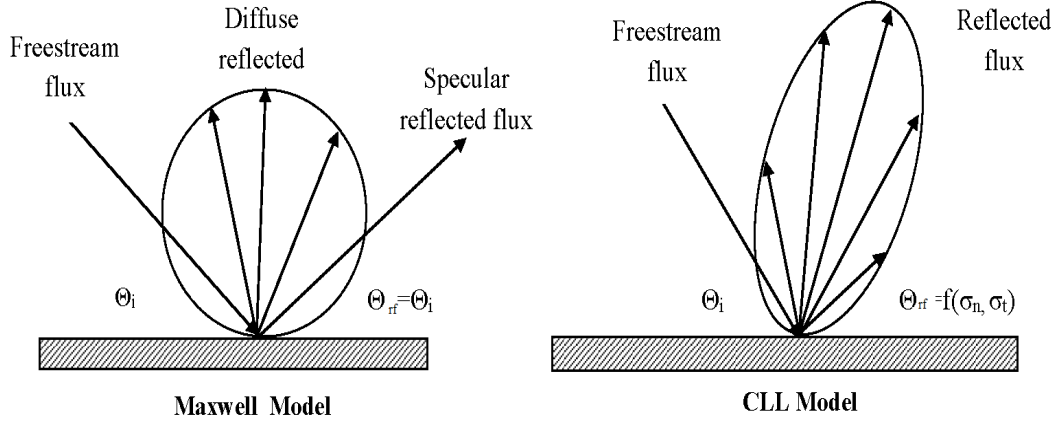
Figure 2.3 - Drawwing illustration of the Maxwell and CLL reflection model.
|Source: Adapted from Leite (LEITE, 2009).

stagnation temperature in a gas differs from the static temperature. For other than fully specular reflection, the distribution function for the incoming molecules will be different to that for the reflected molecules, and the distribution function for the molecules near the surface will not be Maxwellian. Also, the energy of a molecule relative to the surface before it strikes the surface will generally be different from the energy relative to the surface after it has been reflected from the surface, so that the process is inelastic (BIRD, 2013).

The opposite limit to diffuse reflection is the specular reflection in which is perfectly elastic, meaning that the only change to the particle properties is its velocity component normal to the surface that is simply reversed in sign (BOYD, 2014). Specularly reflecting surface is functionally identical to a plane of symmetry (BIRD, 2013). Many DSMC computations use an accommodation coefficient, $\alpha$, to simulate a combination of diffuse and specular reflections such that $\alpha = 1$ is fully diffuse, and $\alpha = 0$ is fully specular. This approach is sometimes referred to as the Maxwell model for gas-surface interaction. It has been found (BIRD, 2013) that, for surfaces that are encountered in engineering problems, there is generally good agreement with calculations as the molecules are assumed to reflect diffusely at the surface temperature, and generally require a value in the range of $\alpha = 0.8 - 0.9$ (BOYD, 2014).

The general requirement, at a molecular level, for equilibrium between a solid surface and a gas is that the interaction should satisfy the reciprocity condition. This is a

relationship between the probability of a gas-surface interaction with a particular set of incident and reflected velocities and the probability of the inverse interaction. It may be written (CERCIGNANI, 1969) as:

$$\boldsymbol{c_{rf}}.\boldsymbol{e}P(-\boldsymbol{c_{rf}}, -\boldsymbol{c_i})exp\left(\frac{-E_{rf}}{kT_w}\right) = -\boldsymbol{c_i}.\boldsymbol{e}P(\boldsymbol{c_i}, \boldsymbol{c_{rf}})exp\left(\frac{-E_i}{kT_w}\right) \qquad (2.63)$$

The unit vector **e** has been taken normal to the surface which is at temperature $T_w$. $P(c_1, c_2)$ is the probability that a molecule incident on a surface with velocity $c_1$ leaves with velocity $c_2$, and $E$ is the energy of the molecule. This condition is related to the law of detailed balance and is satisfied by both the diffuse and specular models for a gas in equilibrium with a surface. While most DSMC applications deal with non-equilibrium situations, the procedures for gas-surface interactions must be such that reciprocity is satisfied when they are applied to equilibrium situations (BIRD, 2013).

Finally, at inlet and outlet boundaries, the physical states of particles should be determined to avoid poorly formulated inflow and outflow treatment (PIEKOS; BREUER, 1996; ANDERSON, 1990). The most probable molecular thermal velocity of the introduced molecule is determined in accordance with the temperature given at inlet. The thermal velocity components perpendicular to the inlet and outlet boundaries are assigned to the incoming particles. Other variables at both inlet and outlet boundaries have to be specified from the states of particles inside the flowfield (XUE et al., 2000).

### 2.2.8    Binary Collision Mechanics

The models for internal energy modes are an add-ons to the VHS molecular model for the translational modes. They affect the translational modes only to extend that the post-collision translational energy differs from the pre-collision translational energy. The possibility of chemical reactions may be taken into account and there may be changes in the pre- and post-collision molecular masses (BIRD, 2013).

Consider a collision between two molecules of mass $m_1$ and $m_2$ with velocity $\mathbf{c}_1$, and $\mathbf{c}_2$, respectively. The corresponding post-collision variables are $m'_1$, $m'_2$, $\mathbf{c}'_1$ and $\mathbf{c}'_2$. Conservation of mass and momentum requires that,

$$m_1 + m_2 = m_1' + m_2'$$
$$m_1 c_1 + m_2 c_2 = m_1' c_1' + m_2' c_2'$$

(2.64)

The centre of mass velocity $c_m$ that is defined by:

$$c_m = \frac{m_1 c_1 + m_2 c_2}{m_1 + m_2} = \frac{m_1' c_1' + m_2' c_2'}{m_1' + m_2'}$$

(2.65)

is therefore unchanged in the collision. The pre-collision and post-collision relative velocities of the molecules are:

$$c_r = c_1 - c_2$$
$$c_r' = c_1' - c_2'$$

(2.66)

Equations 2.56 and 2.66 may be combined to obtain expressions for the molecular velocities in terms of the relative and centre of mass velocities. Those for pre-collision velocities are:

$$c_1 = c_m + \frac{m_2}{m_1 + m_2} c_r$$
$$c_2 = c_m - \frac{m_1}{m_1 + m_2} c_r$$

(2.67)

and those for the post collision velocities are:

$$c_1' = c_m + \frac{m_2'}{m_1' + m_2'} c_r'$$
$$c_2' = c_m - \frac{m_1'}{m_1' + m_2'} c_r'$$

(2.68)

When considering the translational energies associated with the collision, it is customary to introduce the reduced mass given by $m_1 m_2 / (m_1 + m_2)$. The pre-collision translational energy of the molecules can then be written down from Eqs. 2.67 and

2.68 as,

$$E_t = 1/2m_1c_1^2 + 1/2m_2c_2^2 = 1/2(m_1 + m_2)c_m^2 + 1/2m_rc_r^2 \qquad (2.69)$$

Mass is conserved in the collision and the centre of mass velocity is unchanged so that the corresponding post-collision translational energy is:

$$E_t' = 1/2m_1'c_1'^2 + 1/2m_2'c_2'^2 = 1/2(m_1 + m_2)c_m^2 + 1/2m_r'c_r'^2 \qquad (2.70)$$

It should be noted that, for collisions that involve chemical reactions, the post-collision reduced mass differs from the pre-collision value. The initial data for the DSMC computation of a binary collision comprises the molecular species, the three velocity components of each molecule and either the energy in or the quantum state of each internal mode. The collision routine involves the following steps (BIRD, 2013):

- The components of the centre of mass and relative velocity vectors are calculated from Eqs. 2.56 and 2.66 and the relative translational energy in the collision $1/2m_rc_r^2$ is calculated.

- The total collision energy is the sum of the relative translational energy and the energies in all the internal modes of both molecules.

- In the case of chemically reacting flows, the heats of formation of each molecule are added to the total collision energy. The reaction model is then applied and, if the reaction occurs, the molecular species are set to the post-reaction identities and the total collision energy is adjusted for the changed heats of formation.

- The models for the internal models are applied and the pre-collision energies are either retained or adjusted. The post-collision internal energies are subtracted from the total collision energy to obtain the post-collision relative translational energy $1/2m_r'c_r'^2$.

- The magnitude of the post-collision relative velocity is calculated and the elastic collision model is applied to determine the components of the post-collision relative velocity. Equation 2.68 is used to calculate the post-collision velocity components in the frame of reference.

## 2.2.9 Elastic Collision Models

As seen before, the cross-section of the Variable Hard Sphere (VHS) molecular model, is chosen to match the coefficient of viscosity at some reference temperature (Eq. 2.25), and the dependence of the cross-section on the relative translational energy is chosen to match the dependence of the viscosity on temperature in the real gas. The basic hard-sphere collision mechanics used in the VHS model is illustrated in the Fig. 2.4.
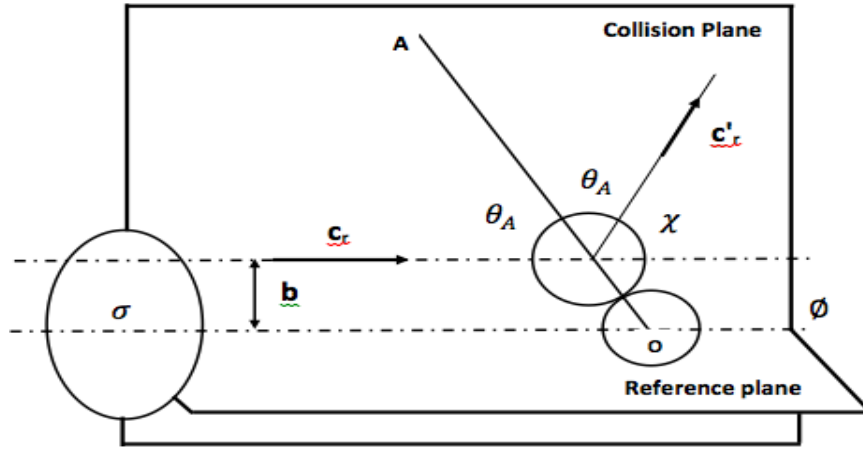


Figure 2.4 - The collision mechanics of hard sphere molecules in the centre of mass frame of reference.
Source: Adapted from Bird (BIRD, 1994).

A collision is planar in the centre of mass frame of reference and the impact parameters are the angle $\phi$ between the collision plane and a plane of reference and the distance $b$ between lines through the centres of the molecules that are parallel to the pre-collision relative velocity. As shown in Fig. 2.4, the origin $O$ is at the centre of one of the molecule and the line $OA$ through the centre of the other molecule defines de apse line. The apse line bisects the angle between the pre-collision and post-collision relative and the deflection angle is defined as:

$$\chi = \pi - 2\theta_A \tag{2.71}$$

where $\chi/2$ is complementary to $\theta_A$. The geometry in Fig. 2.4 is such that,

$$\chi = cos^{-1}(b/d_{12}) \tag{2.72}$$

where $d_{12} = (d_1 + d_2)/2$ is the mean diameter of the two molecules. The element of solid angle into which the molecule is scattered is:

$$d(\Omega) = sin\chi d\chi d\phi = (4/d_{12}^2)bdbd\phi = (4/d_{12}^2)d(\sigma) \tag{2.73}$$

The element of solid angle is therefore related to the element of cross-section by a constant so that the hard-sphere scattering is isotropic in the centre of mass frame of reference. The total solid angle is $4\pi$ so that the total collision cross-section for hard sphere molecule is, as expected,

$$\sigma = \pi d_{12}^2 \tag{2.74}$$

The direction of the post-collision relative velocity is set by randomly selected azimuth and elevation angles, i.e,

$$cos\theta = 2R_F - 1, sin\theta = \sqrt{1 - cos^2\theta}$$
$$\phi = 2\pi R_F \tag{2.75}$$

where $R_F$ is the random number.

In this sense, the three components of post-collision (BIRD, 2013) relative velocity are therefore,

$$u'_r = cos\theta c'_r$$
$$v'_r = sin\theta cos\phi c'_r \tag{2.76}$$
$$w'_r = sin\theta sin\phi c'_r.$$

# 3 COMPUTATIONAL PROCEDURE

## 3.1 Geometry Definition

In the present account, discontinuities present on the surface of a reentry vehicle are modeled by a flat-plate with a gap of length $L$ and depth $H$, and a forward-facing step with height $h$. The combination of a gap with a forward-facing step is defined herein as a gap/step configuration. By considering that the nose radius $R$ of a reentry vehicle [see Fig. 1.2(b)] is orders of magnitude larger than the gap depth $H$, the gap width $L$, or the step frontal-face height $h$, then one has that $H/R$, $L/R$, or $h/R \ll 1$. In this fashion, an understanding of the $L/H$ ratio and the frontal-face height $h$ impact on the flowfield structure can be gained by comparing the flowfield behavior of a flat-plate with a gap/step to that of a flat-plate without a gap/step. Figure 3.1 displays the schematic view of the model employed.
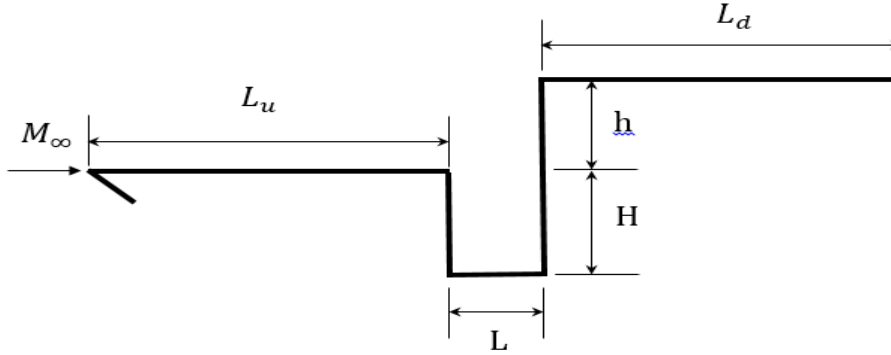


Figure 3.1 - Schematic view of the gap/step geometry.

According to Fig. 3.1, $M_\infty$ represents the freestream Mach number, $H$ is the gap depth, $h$ is the step height, $L_u$ is the length of the gap/step upstream surface, $L$ is the length of the gap, and $L_d$ is the length of the gap/step downstream surface. It was assumed three different length-to-depth ($L/H$) ratios for the combined gap/step configuration – 1, 1/2, and 1/4 – which corresponds to the gap length $L$ of 3 mm and a gap depth $H$ of 3, 6 and 12 mm, respectively. In addition, the step height $h$ investigated was defined as being 3, 6, and 9 mm, which correspond to the dimensionless height $h^*(\equiv h/\lambda_\infty)$ of 3.23, 6.46, and 9.69, respectively, where $\lambda_\infty$ is the freestream mean free path for 70 km. Furthermore, it was defined $L_u/\lambda_\infty$ of 50 and $L_d/\lambda_\infty$ of 50. It was considered that the flat-plate is infinitely long but only the total length $L_u + L + L_d$ is investigated.

As a base of comparison, for 90, 80, 70, and 60 km of altitude, the molecular mean free path $\lambda$ is 26.03, 4.11, 0.929, and 0.265 mm, respectively. As a result, for $H$ (or $L$ and $h$) of 3 mm, the global Knudsen number is the order of 8.67, 1.37, 0.31, and 0.088, for altitudes of 90, 80, 70 and 60 km, respectively. In this scenario, the Knudsen number is in the transition flow regime, as defined earlier in Fig. 1.4. In the transition flow regime, concepts of the continuum hypothesis cannot be applied, and the molecular structure of the gas must be considered as illustrated in Fig. 1.5.

## 3.2  Numerical Simulation Conditions

In the present study, molecular collisions are modeled by using the variable hard sphere (VHS) molecular model, and the No-Time-Counter (NTC) method as a collision-sampling technique. The energy exchange between kinetic and internal modes is controlled by the Larsen-Borgnakke (LB) phenomenological model (BORGNAKKE; LARSEN, 1975).

These inelastic collisions, ensure the energy exchange between the various internal modes. In addition, they tend to push the internal energy distributions toward their equilibrium state. Collision numbers, which correspond to the number of collisions necessary, on average, for a molecule to undergo relaxation, were assumed to have a temperature dependence as cited earlier and defined by Bird (BIRD, 2008) for vibration and Boyd (BOYD, 1990) for rotation.

The freestream coefficient of viscosity $\mu_\infty$ and the mean free path $\lambda_\infty$ used in the present simulation are evaluated from a consistent definition (BIRD, 1983) by using the VHS molecular model with the temperature exponent $\omega$ (Eqs. 2.25) equal to 0.77 and 0.74 for $O_2$ and $N_2$, respectively. Table 3.1 summarizes the air characteristics used in the present DSMC calculations.

The computational domain used for the calculations is large enough so that body disturbances do not reach the upstream and side boundaries, where the freestream conditions are specified. The flowfield is divided into a number of regions and each one of then has a separated value of time step $\Delta t$ and a scaling factor $F_N$, which relates the number of real molecules to the number of simulated particles (SHU et al., 2005). The ratio of these two quantities, $F_N$ and $\Delta t$, is the same in every region. The cell dimensions must be such that the change in flow properties across each cell is small; hence, the cell dimension is less then the local mean free path. Each cell is divided into four subcells (two subcell/cell in each coordinate direction), the smallest unit of physical space, where the collision partners are selected for the establishment

Table 3.1 - Characteristics of simulated air for DSMC calculations

| Properties | Values | Unity |
|---|---|---|
| Working Fluid | $N_2 + O_2$ | |
| Molecular Weight | 28.96 | kg/kgmole |
| Molecular Mass of $O_2$ | $5.312 \times 10^{-26}$ | kg |
| Molecular Mass of $N_2$ | $4.650 \times 10^{-26}$ | kg |
| Molecular Diameter $O_2$ | $4.070 \times 10^{-10}$ | m |
| Molecular Diameter $N_2$ | $4.170 \times 10^{-10}$ | m |
| Moles Fraction of $O_2$ | 0.237 | |
| Moles Fraction of $N_2$ | 0.763 | |
| Viscosity Index of $O_2$ | 0.77 | |
| Viscosity Index of $N_2$ | 0.74 | |
| Degrees of Freedom of $O_2$ | 5 a 7 | |
| Degrees of Freedom of $N_2$ | 5 a 7 | |

of the collision rate. Also, time is advanced in discrete steps such that each step is small in comparison with the mean collision time. A view of the computational domain is depicted in Fig. 3.2.

According to the Fig. 3.2, side I-A is the gap/step surface. Diffuse reflection with complete thermal accommodation is the condition applied to this side. Side I-B is a boundary where all flow gradients normal to the boundary are zero. Sides II and III are freestream sides through which simulated particles can enter and exit. Finally, the flow at the downstream outflow boundary, side IV, is predominantly supersonic and vacuum condition is specified. At this boundary, simulated particles can only exit. The choice of vacuum is normally used when the velocity of the gas through the boundary is supersonic. For flows with Mach number equal to or greater than three, the simulated particles entering to the computational domain through the boundary can be neglected (BIRD, 1994).

The mesh generation, the effect of the mesh resolution, and the verification and validation process employed in the present account are discussed in the next chapter.

## 3.3 Freestream Flow conditions

The freestream flow conditions represent those experienced by a reentry vehicle at an altitude of 70 km, and are summarized in Tab 3.2.

The freestream velocity $U_\infty$ is assumed to be constant at 7,546.5 m/s, which corresponds to a freestream Mach number $M_\infty$ of 25. The wall temperature $T_w$ is assumed
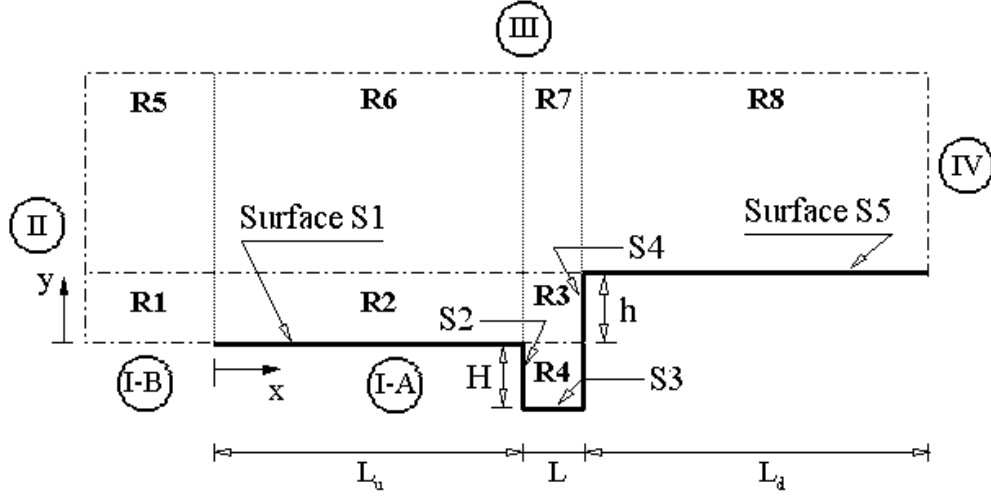
Figure 3.2 - Computational domain of the gap/step geometry.

Table 3.2 - Freestream flow conditions

| Altitude (km) | $T_\infty$(K) | $p_\infty$(N/m$^2$) | $\rho_\infty$(kg/m$^3$) | $\mu_\infty$(Ns/m$^2$) | $n_\infty$(m$^{-3}$) | $\lambda_\infty$(m) |
|---|---|---|---|---|---|---|
| 70 | 219.69 | 5.582 | $8.753 \times 10^{-5}$ | $1.455 \times 10^{-5}$ | $1.8192 \times 10^{21}$ | $9.285 \times 10^{-4}$ |

to be constant at $880\ K$. This temperature is chosen to be representative of the surface temperature near to the stagnation point of a reentry capsule, and it is also assumed to be uniform on the gap/step surface. It is important to mention that this surface temperature is low compared to the freestream stagnation temperature. This assumption seems reasonable since practical surface material will probably be destroyed if the surface temperature is allowed to approach the stagnation temperature.

# 4 VERIFICATION AND VALIDATION PROCESS

## 4.1 Code Verification and Validation

The code verification and validation process plays an important rule before proceeding with the numerical results. The verification and validation process in the DSMC method consists of four basic steps; (1) verification by increasing the number of computational cells, (2) by increasing the number of simulated particles, (3) by increasing the time step, and (4) validation by comparing with experimental or numerical results available in the literature. In such a context, the purpose of this Chapter is to discuss at length these four basic steps.

## 4.2 Computational Requirements

Three primary constraints on the DSMC method must be considered when evaluating computational requirements: (1) the simulation time step must be less than the local average collision time, (2) the cell size must be smaller than the local mean free path, and (3) the number of simulated particles per cell must be roughly constant in order to preserve collision statistics, since it is very important to obtain sufficient collisions in the computation.

As pointed by Bird (BIRD, 1994), an important assumption in the DSMC method is that the gas is dilute, meaning that the average molecular diameter is much smaller than the average spacing between molecules in the gas. This assumption allows that the molecular motion be decoupled from the molecular collisions over a small local time internal. Thus, the successful application of the method requires that the time step must be a fraction of the average time between collisions, as well the linear size of a collision cell should be usually not greater than the local mean free path, $\lambda$. Violation of this requirement can lead to a significant distortion of flow properties.

The DSMC method uses the mesh or cell system only for the selection of possible collision partners. Many practical problems involve complex body shapes and the generation of suitable mesh can be very demanding and time consuming task. Numerous efforts to develop alternative meshes and to reduce the computational cost of the method have resulted in a several different mesh schemes that provide an extensive list of options from which to choose: structured, unstructured, body-fitted, cartesian, and others. Each of these schemes has advantages and disadvantages such as a low cost during the movement of simulated particles, the use of cells with non-uniform size in regions where the gradients are more intense, and application

in simulation of complex geometries. For example, an advantage of the body-fitted over the cartesian mesh is a possibility of minimizing the computational domain size by adapting the domain shape to an expected disturbed area. The mesh cell structure can therefore be irregular with regard to the shape of the cells and there can be discontinuities in the mesh lines that define the cell (continuum methods generally require a near orthogonal mesh structure with no discontinuities). Wilmoth (WILMOTH et al., 1996) and Nance (NANCE et al., 1997) discussed in details the advantages of each scheme, in terms of accuracy, computational efficiency and ease of use.

In order to simulate the collisions, the present numerical DSMC investigation employs a cartesian mesh consisting of uniform cells where the computational domain is usually a rectangular cartesian box. The use of rectangular cells has a main advantage in the sense that to be simple and effective in the particle indexing process in cells, whereas the use of a body-fitted mesh or another, which requires tracing or sorting of particles, increases the computational cost by a factor of 2 to 10. This rectangular regular cells are divided into small cells depending on the flow pattern. Typically, closer to the body surface, the smallest cells are located (an order of or smaller than one third of the local mean free path).

In certain regions, such as the vicinity of adiabatic surfaces, flowfield gradients must be very small, and the cell size must be small enough to adequately capture flowfield physics near to the body surface. Otherwise, the most energetic particles so close to the far edge of the cell could transfer energy and momentum to simulated particles located immediately adjacent to the body surface. Moreover, such particles adjacent to the surface could transfer energy and momentum to the body surface, and as a consequence, this leads to a over prediction of the heat flux and of the aerodynamic forces (FALLAVOLLITA et al., 1993). This type of error can be minimized by reducing the cell size relative to the local mean free path of simulated particles near to the surface. The cell size should be small in regions within the flowfield where the physical properties vary rapidly. It is also important to mention that the division of the cells in sub-cells is performed during the adaptation procedure according to the local flow gradients. Studies of mesh convergence in typical test cases showed that reductions in the sub-cell size has the same benefits as reductions in cell size (BIRD, 2001).

With respect to adequately model the physics of interest, the number of simulated particles in the numerical code must be greater than a certain number. To obtain

accurate collision statistics and DSMC results, it is desirable to have at least 20 - 30 simulated particles in each cell (FALLAVOLLITA et al., 1993) (SHU et al., 2005). However, in high density regions the cell Knudsen number - $Kn_c$ (see Eq. 1.1) will be smaller than unity, i.e, the linear size of such cells will be greater than the local mean free path. The simplest way to avoid such a situation consists only in a significant increasing of the total number of simulated particles. On one hand, the use of a great total number of simulated particles allows one, in high density regions, to obtain cells with $Kn_c > 1$ and containing at least the minimum number of simulated particles. On the other hand, in low density regions, the number of simulated particles in a cell is much greater then that needed for correct modeling. Thus, an increase in the total number of simulated particles for detailed spatial resolution of flow in high density regions leads to overpopulation of particles in low density regions, which significantly decreases in the computational efficiency. In order to obtain a more uniform distribution of simulated particles per a cell throughout the computational domain, a variable scaling factor $F_N$, which is the ratio of real molecules to simulated particles, is used to control the distribution of simulated particles within the mesh. Based on this procedure, the flowfield is subdivided into an arbitrary number of regions where the time step $\Delta t$ and the scaling factor $F_N$ remain constant within a region, but they can vary from one region to another. The combination of subdividing the flowfield into regions along with the use of variable cell sizes, provides the flexibility to substantially reduce the total number of simulated particles used in the simulation and also resolves the flow gradients. It is important to mention that although $F_N$ and $\Delta t$ can vary from region to region, the ratio $F_N/\Delta t$ must be the same for all regions, in order to conserve mass across region boundaries in the flow. In this scenario, with all these set up parameters, the computational effort can be greatly reduced. More details for estimating the computational requirements of DSMC simulations are presented at length by Rieffel (RIEFFEL, 1999).

## 4.3 Computational Mesh Generation

In the present study, the mesh generation scheme used was based on the procedure presented by Bird G2 algorithm (BIRD, 1999). In this manner, the flowfield was divided into a number of arbitrary four-sided regions, Fig. 3.1. Along the opposite boundaries, point distributions are generated in such way that the number of points on each side is the same. The cell structure is defined by joining the corresponding points on each side by straight lines and then dividing each of these lines into segments which are joined to form the system of quadrilateral cells. The distribution

can be controlled by a number of different distribution functions which allow the concentration of points in areas where high flow gradients or small mean free paths are expected. The point distributions may be chosen independently for each region.

## 4.4 Computational Mesh Adaptation

The procedure for mesh adaptation employed in this study was threefold: (1) an initial region and cell mesh structure are generated from consideration of the freestream flow conditions, (2) assumed values of $F_N$ are chosen for each region, $\Delta t$ are then estimated subject to the condition that the ratio $F_N/\Delta t$ be the same for all regions, and (3) these parameters are iteratively modified until an acceptable number of simulated particles, cell size distribution and simulation time step are obtained.

## 4.5 DSMC Test Case

In the present section, the first numerical DSMC test case used for the verification and validation process was a hypersonic rarefied flow over a flat-plate with zero degree angle of attack. This simple geometry makes it most useful test case for the verification and validation code process. In pursuit of this goal, the first numerical DSMC code employed was adapted in order to reproduce the numerical DSMC data given by Tsuboi et al. (TSUBOI et al., 2004) and numerical DSMC and experimental results given by Lengrand et al.(LENGRAND et al., 1992), employing the Dynamic Molecular Collision (DMC) and LB for the gas-gas interaction model, respectively.

In the study given by Tsuboi et al.(TSUBOI et al., 2004), a bi-dimensional flow over a sharp flat-plate with a finite leading-edge angle, located in a rarefied hypersonic flow, was investigated numerically using the DSMC method along with the DMC gas-gas interaction model. Their goal was to reproduce the numerical DSMC/experimental investigations of a rarefied hypersonic flow over a flat-plate conducted by Lengrand et al. (LENGRAND et al., 1992). The DMC model was implemented by Tokumasu and Matsumoto (TOKUMASU; MATSUMOTO, 1999) in order to accurately predict the non-equilibrium between molecular internal degrees of freedom in a rarefied gas flow at a temperature bellow 2000 K. The method was based on the molecular dynamics simulation of Nitrogen molecules.

In the same fashion, Lengrand et al. (LENGRAND et al., 1992) presented a DSMC simulation and an experimental investigation of a rarefied hypersonic flow over a flat-plate. The numerical results were obtained by the DSMC method using the LB gas-gas interaction model. The experimental data were given by the flow conditions

obtained in the SR3 low-density facility of the Centre National de la Recherche Scientifique in Meudon, France. In this sense, the experimental work consisted of a flowfield surveys by an electron bean fluorescence probe, yielding the flowfield density distribution, wall pressure and heat transfer measurements using thermocouples imbedded in a thin wall.

The freestream flow conditions and the geometry parameters, used in the present section, are those given by the numerical and experimental investigations made by Lengrand et al.(LENGRAND et al., 1992) that was numerically reproduced by Tsuboi et al. (TSUBOI et al., 2004), and are displayed in Table 4.1.

<div align="center">

Table 4.1 - Freestream flow conditions

| Properties | Value | Unit(SI) |
|---|---|---|
| Mach number $(M_\infty)$ | 20.2 | |
| Pressure $(p_\infty)$ | 0.06822 | $N/m^2$ |
| Density $(\rho_\infty)$ | $1.7256 \times 10^{-5}$ | kg/$m^3$ |
| Number density $(n_\infty)$ | $3.716 \times 10^{20}$ | $m^{-3}$ |
| Temperature $(T_\infty)$ | 13.32 | K |
| Velocity $(U_\infty)$ | 1503 | m/s |
| Mean free path $(\lambda_\infty)$ | $2.35 \times 10^{-3}$ | m |
| Total plate length $(2L)$ | 80 $(\lambda_\infty)$ | m |

</div>

The computational domain used for the present simulation was made large enough so that flat-plate disturbances did not reach the upstream and side boundaries, where freestream conditions were specified. In order to avoid the effect of downstream boundary condition, the plate length used in the present numerical DSMC investigation was of about 80 $\lambda_\infty$. The computational domain was divided into ten regions, and regions were subdivided into computational cells. The schematic view of the computational domain used for the DSMC test case (flat-plate) is displayed into Fig. 4.1. Based on this figure, region 1 consisted of 40 cells along side I-A and 45 cells along side II. Region 2 up to region 10, consisted of 315 cells distributed along side I-B and 45 cells along side IV. This computational mesh was defined as being the standard case. In addition to this mesh, two other meshes, defined by coarse and fine, were used to study the sensitivity of the computations to the mesh resolution.
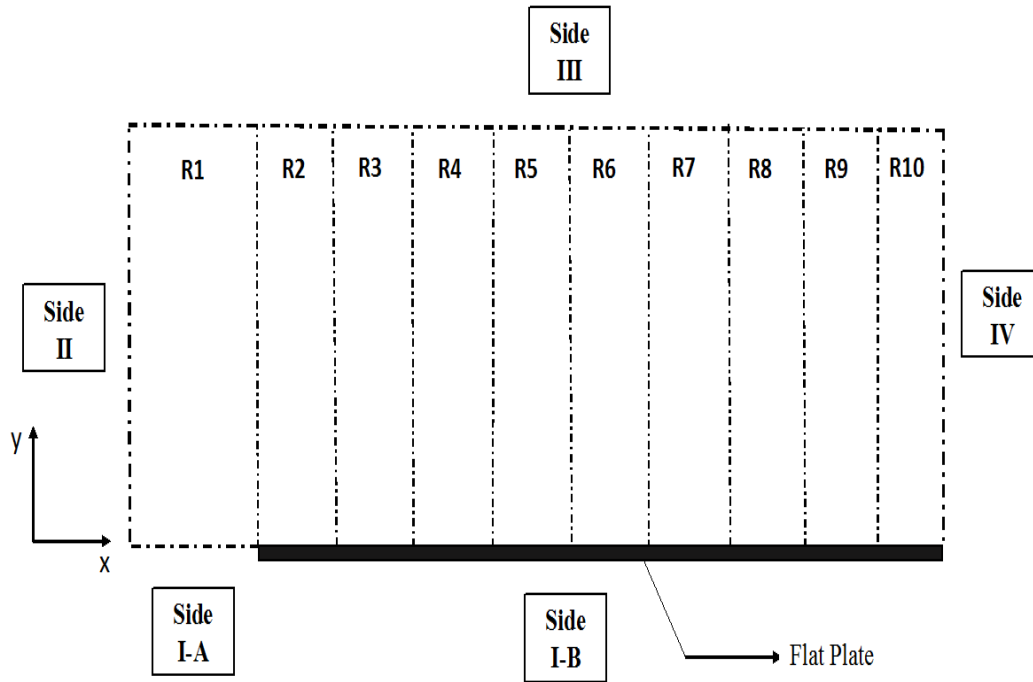
Figure 4.1 - Schematic view of the flat-plate geometry.

### 4.5.1 Effect of Mesh Resolution

The mesh resolution is an important parameter in the DSMC results with particular respect to the aerodynamic surface quantities. An insufficient mesh resolution can reduce significantly the accuracy of predicted aerodynamic heating and forces. Hence, pressure, skin friction, and heat transfer coefficients are used as the representative parameters for the mesh sensitivity study. The effect of altering the mesh resolution in the $x$ and $y$ direction was investigated for a coarse and a fine mesh with, respectively, 50% less and 100% more cells with respect to the standard mesh. Table 4.2 tabulates the number of cells employed in the ten regions for coarse, standard, and fine meshes. Furthermore, each mesh was made up of nonuniform cell spacing in both directions.

The effect of altering the cell size is displayed in Fig. 4.2 as it impacts the calculated pressure, skin friction and heat transfer coefficients. The comparison shows that the effect of cell variations over these quantities was negligible for the cases investigated in the present section, indicating that the standard mesh is essentially independent of the cell size.

Figure 4.2 - Effect of altering the cell size in $x$ and $y$-direction on pressure (top), skin friction (middle) and heat transfer (bottom) coefficients.

Table 4.2 - Number of cells in the (x-direction) and [y-direction] for the flat-plate case.

| Region | Coarse | Standard | Fine |
|--------|--------|----------|------|
| R1 | (20)[22] | (40)[45] | (40)[45] |
| R2 | (20)[22] | (35)[45] | (70)[90] |
| R3 | (20)[22] | (35)[45] | (70)[90] |
| R4 | (20)[22] | (35)[45] | (70)[90] |
| R5 | (20)[22] | (35)[45] | (70)[90] |
| R6 | (20)[22] | (35)[45] | (70)[90] |
| R7 | (20)[22] | (35)[45] | (70)[90] |
| R8 | (20)[22] | (35)[45] | (70)[90] |
| R9 | (20)[22] | (35)[45] | (70)[90] |
| R10 | (20)[22] | (35)[45] | (70)[90] |
| #Cells | 4400 | 15975 | 58500 |

### 4.5.2  Effect of Variation on the Number of Simulated Particles

A similar examination was made for the number of simulated particles. The sensitivity of the calculated results to the variation on the number of simulated particles is demonstrated in Figure 4.3. In this set of plots, the standard mesh corresponds to a total of 335,600 simulated particles. Two new cases using the same mesh were investigated. These new cases corresponds to, on average, 92,500 and 1,200,000 simulated particles in the entire computational domain. It is clearly seen that the results are the same for the three cases investigated, indicating that the number of simulated particles for the standard mesh (335,600) is enough for the code validation process.

### 4.5.3  Effect of Downstream Boundary Condition

At high speed flows, one conventional boundary condition used to the downstream boundary is to impose the vacuum condition (BIRD, 1994), where no simulated particles are allowed to enter in the computational domain. In order to determine the extend of the upstream effect of the imposed downstream vacuum boundary condition, calculations were made for other two plates with different lengths. Figure 4.4 displays a comparison of the aerodynamic surface quantities calculated for three different flat-plate sizes. In this set of plots, the flat-plate length considered was of 45, 80 and 120 $\lambda_\infty$.

According to this set of plots, it is observed that the vacuum boundary condition present a minor effect in the skin friction and in the heat transfer coefficients.
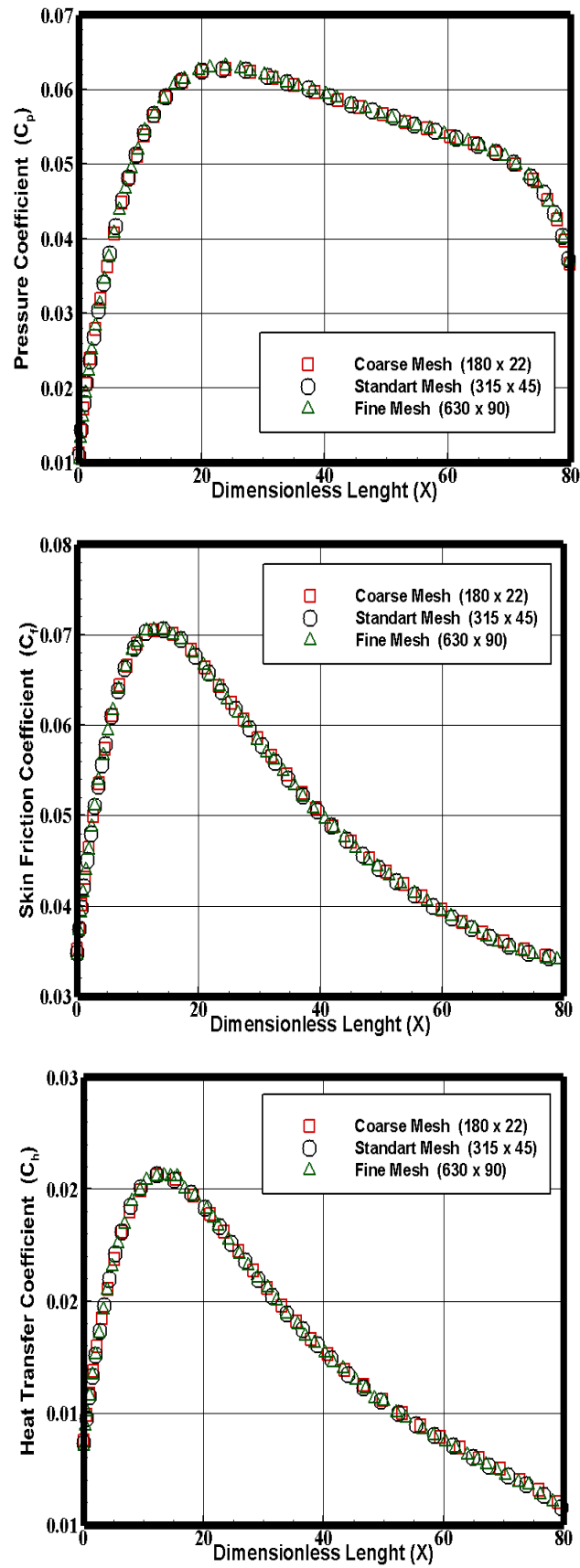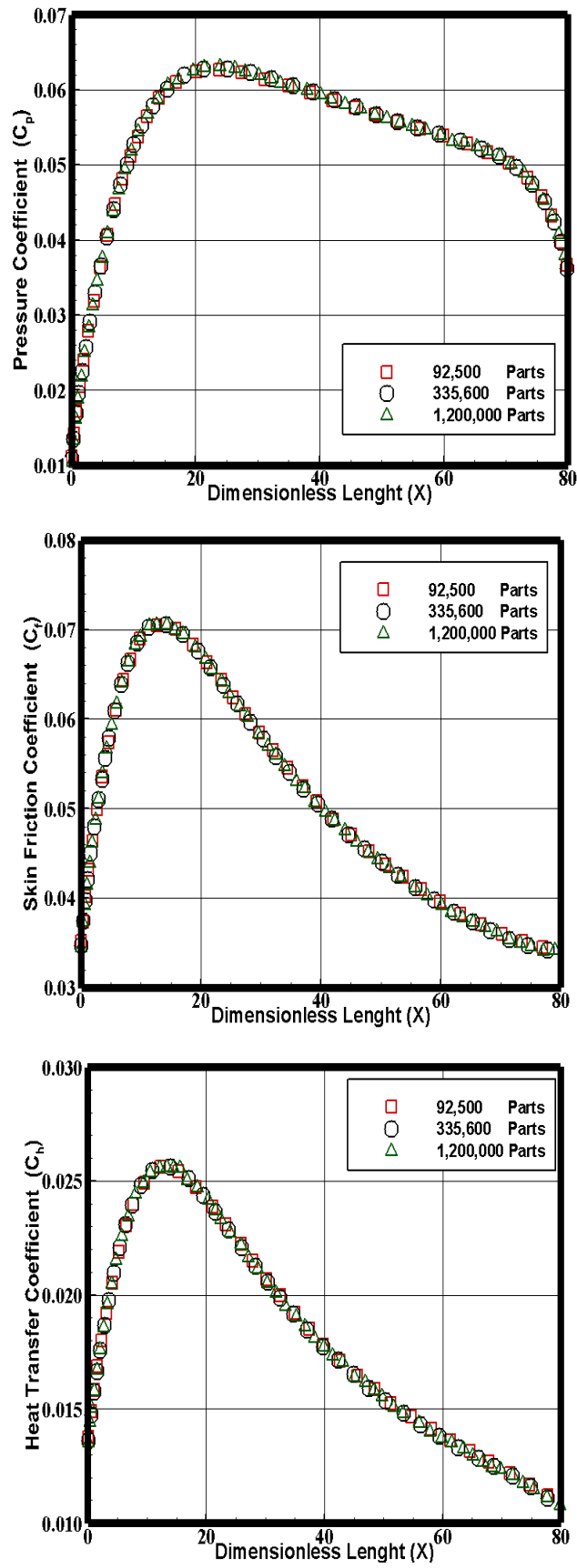
Figure 4.3 - Effect of altering the number of simulated particles on pressure (top), skin
friction (middle) and heat transfer (bottom) coefficients.
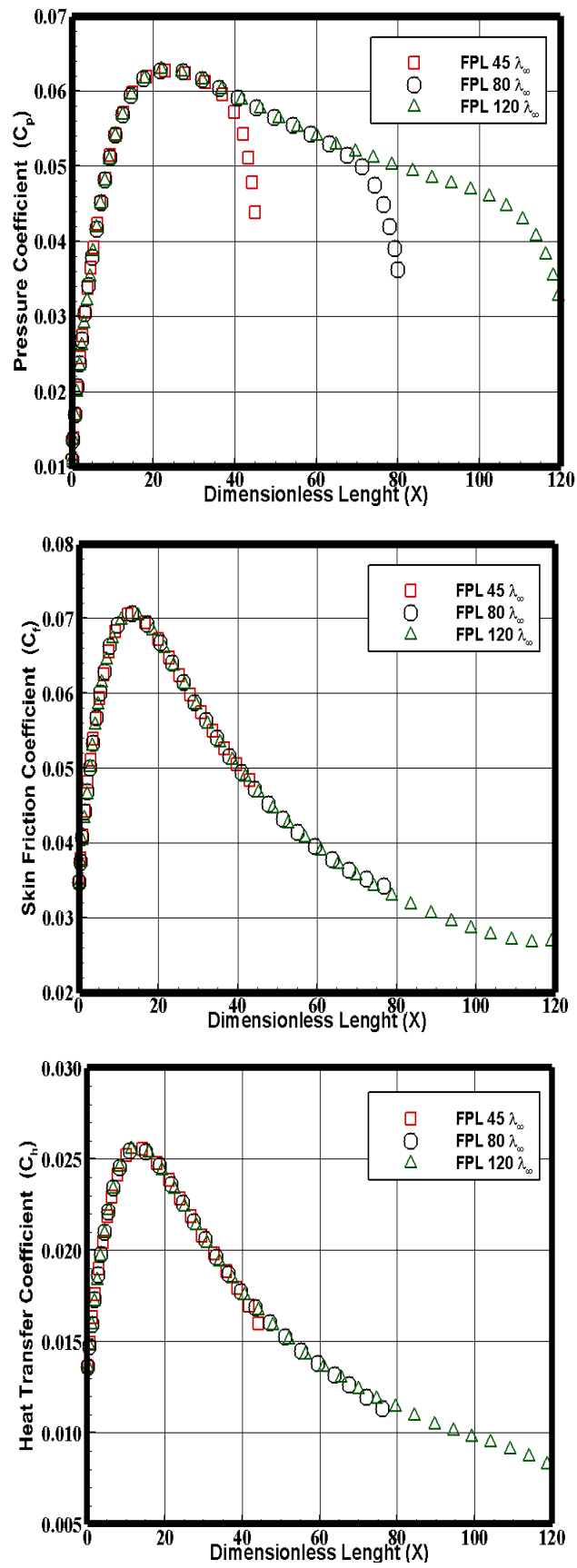
Figure 4.4 - Effect of altering the length of the flat-plate on pressure (top), skin friction (middle) and heat transfer (bottom) coefficients.

However it is clearly noticed that the pressure coefficient is affected around 10 $\lambda_\infty$ upstream of the downstream boundary.

### 4.5.4   Experimental and Numerical Comparisons

In order to ensure the validity of the present numerical DSMC results, this section presents the comparisons of two numerical DSMC flat-plate investigations with experimental and numerical results for a flat-plate given by (1) Lengrand et al. (LENGRAND et al., 1992), that was numerically reproduced using the DSMC method by Tsuboi et al. (TSUBOI et al., 2004), and (2) Tsuboi and Matsumoto (TSUBOI; MATSUMOTO, 2005), that was numerically reproduced using a Unified gas-kinetic scheme (UGKS), by Liu (LIU et al., 2014).

#### 4.5.4.1   First Test Case

The first test case was developed in order to reproduce the results for a rarefied hypersonic flow over a flat-plate that was conducted experimentally and numerically by Lengrand et al.(LENGRAND et al., 1992) and reproduced numerically by Tsuboi et al. (TSUBOI et al., 2004). Freestream flow conditions used in this test case is tabulated in Tab 4.1. In this sense, density profiles at section $x/L$ =1.5 is displayed in Figure 4.5. In this plot, the solid line represents the numerical DSMC test case used to reproduce the experimental and numerical DSMC previously investigated by Lengrand et al. (LENGRAND et al., 1992) and Tsuboi et al.(TSUBOI et al., 2004), respectively; empty and filled square symbols represent the zero[1] and the twenty[2] leading-edge angle of attack related to a bi-dimensional numerical DSMC flow over a flat-plate investigated by Tsuboi et al. (TSUBOI et al., 2004). Finally, for the same conditions, the experimental[3] data obtained by Lengrand et al.(LENGRAND et al., 1992) are represented by filled circles with uncertainty of 10%. Also the ratios $x/L$ and $y/L$ correspond to the distance $x$ from the sharp leading, and the height $y$, both normalized by the flat-plate length $L$.

According to Figure 4.5, it is seen a good agreement with the present results in comparison with experimental data and numerical results obtained by Lengrand et al. (LENGRAND et al., 1992) and Tsuboi et al.(TSUBOI et al., 2004), respectively.

Figure 4.6 displays the translational ($T_t$) and rotational ($T_r$) temperature distributions on the flat-plate (in the cells immediately adjacent to the surface). In this

---

[1] correspond to the *Tsuboi et al.*[1] legend in Figures 4.5, 4.6, and 4.7
[2] correspond to the *Tsuboi et al.*[2] legend in Figures 4.5, 4.6, and 4.7
[3] correspond to the *Lengrand et al.*[3] legend in Figure 4.5, and 4.7
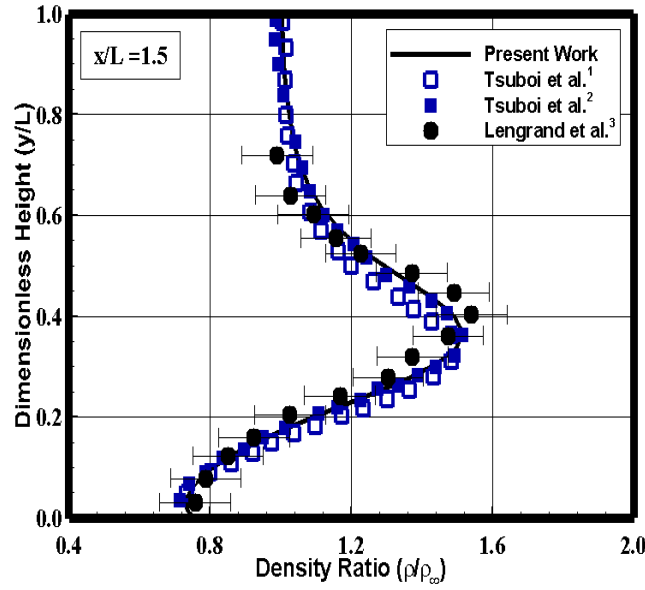
Figure 4.5 - Density profiles at section x/L = 1.5 on the flat-plate surface.

plot, solid and dotted lines represent the present DSMC results for translational and rotational temperatures, respectively. Also filled and empty symbols represent the translational and rotational temperatures, respectively, given by the numerical DSMC results obtained by Tsuboi et al. (TSUBOI et al., 2004). For this particular plot, it is important to mention that square and circle symbols represent the numerical results for zero[1] and twenty[2] leading-edge angle of attack, respectively. Again in this plot, the ratio $x/L$ correspond to the distance $x$ from the sharp leading normalized by the flat-plate length $L$. According to Figure 4.6, it is seen a good agreement of the present results with numerical DSMC investigation given by Tsuboi et al. (TSUBOI et al., 2004).

Figure 4.7 illustrates the pressure ratio distributions on the flat-plate surface. In this plot, numerical DSMC and experimental data are displayed as following: 1) solid line represents the present DSMC results; 2) empty and filled square symbols represent the data obtained by Tsuboi et al. (TSUBOI et al., 2004) for the numerical DSMC investigations for zero[1] and twenty[2] degrees angle of attack, respectively; 3) filled and empty circle symbols represent the data obtained by Lengrand et al. (LENGRAND et al., 1992) – experimental [3] data, and numerical DSMC B4[4] results, respectively – and finally empty triangle corresponds to numerical DSMC B5[5] data, also obtained by Lengrand et al. (LENGRAND et al., 1992).

---

[4]correspond to the *Lengrand et al.*[4] legend in Figures 4.7, and 4.8

[5]correspond to the *Lengrand et al.*[5] legend in Figures 4.7, and 4.8
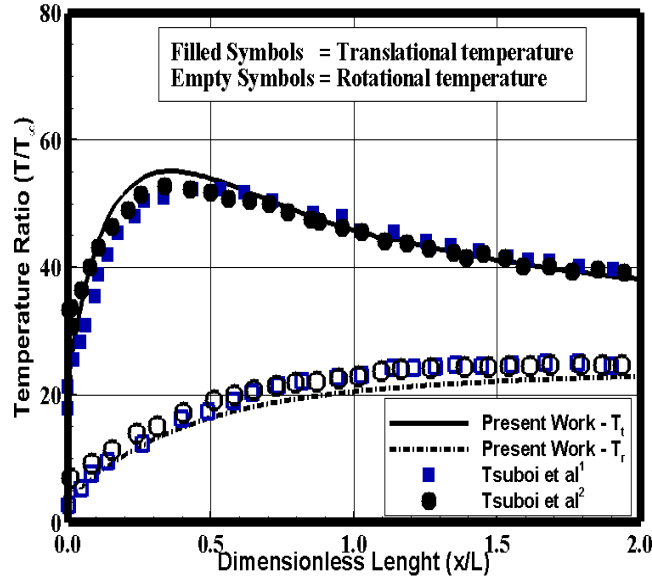
Figure 4.6 - Translational and rotational temperature distributions in the cells immediately adjacent to the flat-plate surface.

Before proceeding with the analysis, it is important to mention that the pressure on the flat-plate surface, in the present DSMC simulations, was calculated by the normal momentum exchange of simulated particles on the surface, and not by the macroscopic pressure $p$ derived from the equation of state, which uses density and temperature as a reference. It should be remarked in this context that the assumption of continuum flow is not valid for the present investigation and, as a consequence, the pressure $p$ at the surface calculated with the ideal gas equation of state does not provide an accurate result.

Looking to Figure 4.7, it is seen differences in the pressure distributions along the flat-plate surface with respect to the others investigations. These differences were probably due to the different numerical parameters used between the current DSMC test case, the experimental and numerical data given by Lengrand et al.(LENGRAND et al., 1992), and the numerical DSMC investigation given by Tsuboi et al.(TSUBOI et al., 2004). In their numerical DSMC work, Tsuboi et al. (TSUBOI et al., 2004) used a DMC gas-gas interaction model for Nitrogen molecules, and the null collision (NC) technique for collision frequency (KOURA, 1986). The DMC gas-gas interaction model, was developed by Tokumasu and Matsumoto (TOKUMASU; MATSUMOTO, 1999). This model accurately predict the non-equilibrium between molecular internal degrees of freedom in a rarefied gas flow at temperature bellow 2000 K. This model is based on the cross sections and energy distributions after the collisions obtained by

71
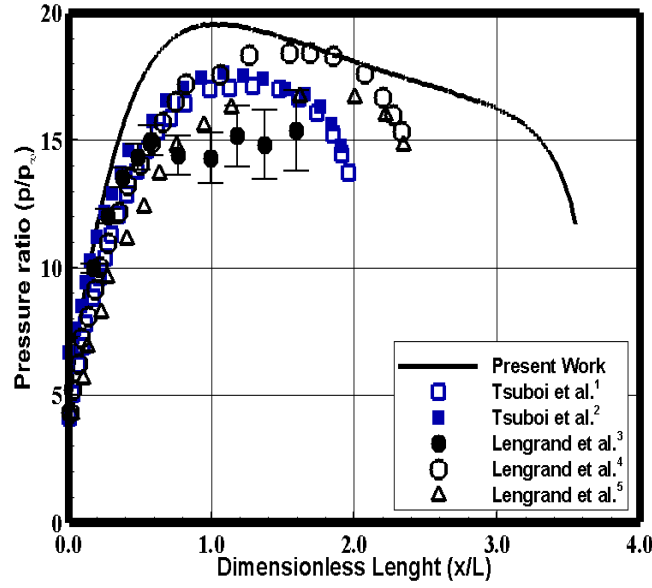
Figure 4.7 - Wall pressure along the flat-plate surface.

the molecular dynamics (MD) simulations for diatomic molecules. It is important to emphasize that the present DSMC solution employed the Larsen-Borganakke (LB) model as the gas-gas interaction model, and the no-time-counter (NTC) technique (BIRD, 1989) for collision frequency. In the same sense, Lengrand et al. (LENGRAND et al., 1992) used in his numerical work the time-counter (TC) by Bird (BIRD, 1976) for collision frequency, and two different values for the fraction of inelastic collisions, $f$. The fraction $f = 0.5$ (DSMC B4[4]) was considered to be consistent with a realistic value of the rotational collision number $Z_r$ equal to a few units. The fraction $f$ = 1 (DSMC B5[5]) was used in order to be more favorable to the Navier-Stokes hypothesis, since the translational and rotational temperatures are equal to a some value (thermodynamic equilibrium, where $T_t = T_r$). In addition, since was impossible to make VHS model to reproduce the correct viscosity in the whole temperature range involved (13-1100 K), two sets of VHS parameters were used by Lengrand et al.(LENGRAND et al., 1992), VL and VH, where VL (DSMC B4[4]) refers to fitting in a low-temperature range $(T_\infty, T_w)$, and VH (DSMC B5[5]) refers to fitting $\sigma_{ref}$ and $\omega$ to the gas viscosity in a high-temperature range $(T_w, T_0)$.

It is also important to remark that, in the present DSMC solution, the intermolecular collision model used for the whole temperature range was the Variable Hard Sphere-VHS, and the rotational collision number $Z_r$ was set to be energy dependent, as suggested by Boyd (BOYD, 1990). Therefore, the difference in the pressure ratio profiles might be attributed to the differences in these parameters.

Figure 4.8 illustrates the Stanton number, $St$, distributions on the flat-plate surface. The Stanton number can be merely compared with the skin friction ($C_f$) coefficient by the relation of St $= C_f/2$. According to this plot, one has: 1) solid line represents the present DSMC results; 2) circle, triangle, and diamond empty symbols represent the numerical DSMC B4[4], DSMC B5[5], and DSMC D1[6] results obtained by Lengrand et al. (LENGRAND et al., 1992), respectively. It is important to mention that the DSMC D1[6] case considered the full accommodation parameter, the fraction of inelastic collisions $f = 0.5$, and the VH molecular model, which refers to the fitting $\sigma_{ref}$ and $\omega$ to the gas viscosity in a high temperature range, as discussed earlier. Quite similar to the pressure distributions, the Stanton number along the flat-plate surface presents good agreement between the present DSMC results and the DSMC results obtained by Lengrand et al. (LENGRAND et al., 1992).
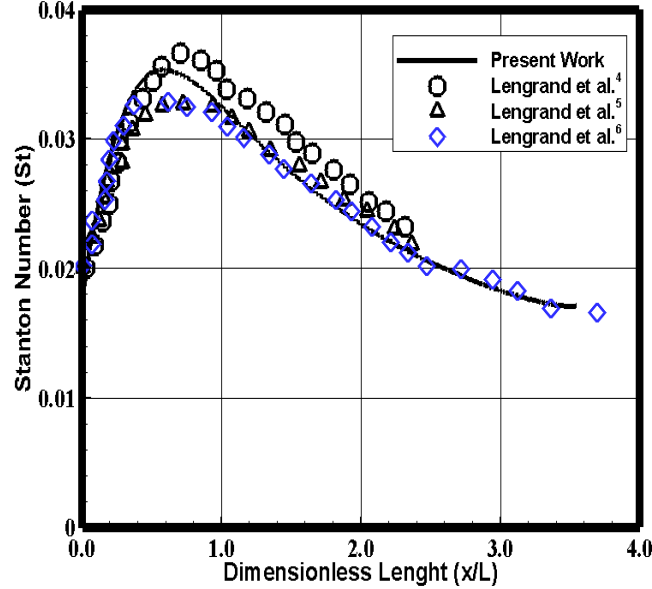


Figure 4.8 - Stanton number along the flat plate surface.

#### 4.5.4.2 Second Test Case

A second test case was simulated in order to reproduce the results for a rarefied hypersonic flow over a flat-plate that was conducted experimentally by Tsuboi and Matsumoto (TSUBOI; MATSUMOTO, 2005), and reproduced numerically using a Unified gas-kinetic scheme (UGKS), developed by Liu et al. (LIU et al., 2014). The Unified gas-kinetic scheme was constructed for both continuum and rarefied flow

---

[6]correspond to the *Lengrand et al.*[6] legend in Figure 4.8

computations. According to Liu et al. (LIU et al., 2014), this scheme is more efficient than that in the traditional DSMC method in the low transition and continuum flow computations. In addition, the UGKS scheme has been validated extensively (LIU et al., 2014) through numerical tests in comparison with DSMC solutions in the transition flow regime. The freestream flow conditions and the simulation conditions used in this test case are tabulated in Tab.4.3.

Table 4.3 - Comparison of freestream flow conditions for numerical simulations given by the second DSMC code, by Liu et al. (LIU et al., 2014) and experimental data obtained by Tsuboi and Matsumoto (TSUBOI; MATSUMOTO, 2005)

| Work | Gas | $M_\infty$ | $T_\infty$ (K) | $p_\infty$ (Pa) | N.M.* |
|---|---|---|---|---|---|
| (LIU et al., 2014) | $N_2$ | 4.89 | 116 | 2.12 | UGKS |
| (TSUBOI; MATSUMOTO, 2005) | $N_2$ | 4.89 | 116 | 2.12 | Experimental |
| Test Case | $N_2$ | 5.0 | 116 | 2.12 | DSMC |

* N.M. = Numerical method
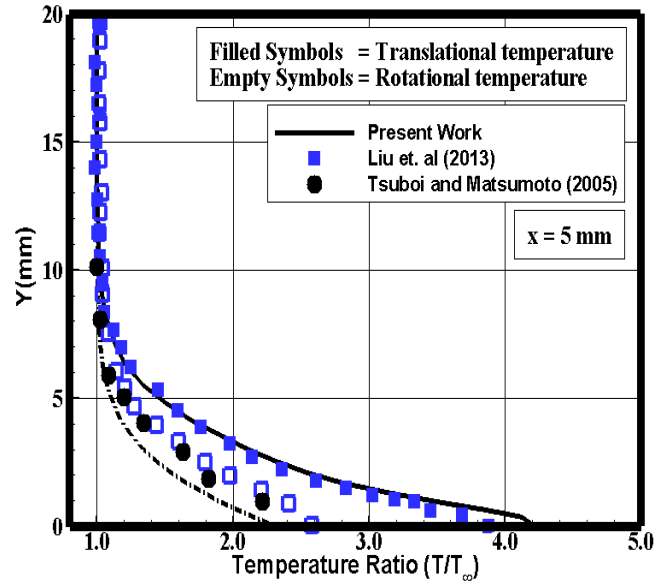


Figure 4.9 - Temperature profiles along vertical lines at x = $5mm$

Figures 4.9, and 4.10 display the translational and rotational temperature profiles, normalized by the freestream temperature, for two sections along the flat-plate surface. In this set of plots, solid and dashed lines represent the second DSMC test case for the translational and rotational temperatures, respectively; square symbols
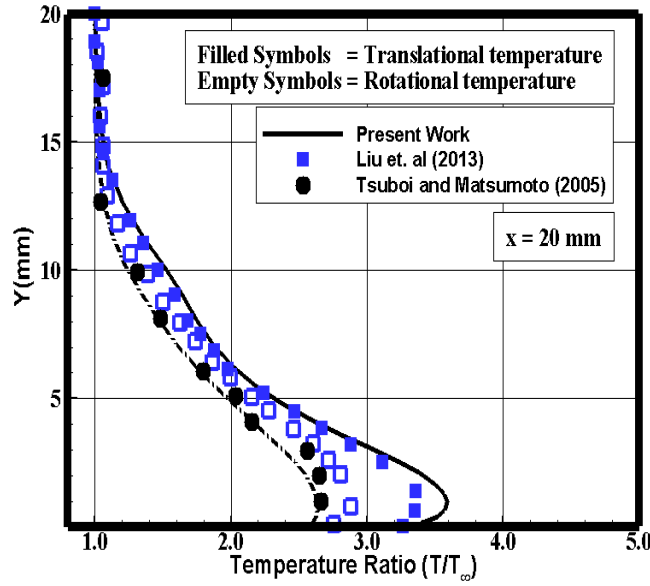
Figure 4.10 - Temperature profiles along vertical lines at (a) x = $20mm$

represent the numerical UGKS study given by Liu et al.(LIU et al., 2014), and finally circle symbols represent the experimental results (Run number 34) for rotational temperature given by Tsuboi and Matsumoto (TSUBOI; MATSUMOTO, 2005), with uncertainty of 0.5%.

According to the Figures 4.9 and 4.10, it is seen that the non-equilibrium between the translational and rotational temperatures in the vicinity of the flat-plate surface is quite large, and even by the differences between the numerical methods used in the investigations, and tabulated in Tab.4.3, data obtained from the present DSMC results agree fairly well with the numerical UGKS, and experimental investigations given by Liu et al. (LIU et al., 2014) and Tsuboi and Matsumoto (TSUBOI; MATSUMOTO, 2005).

## 4.6 Gap/step case

This section presents the analysis in order to do the verification of the mesh resolution and the number of simulated particles influence on the aerodynamic surface quantities – heat transfer ($C_h$), pressure ($C_p$), and skin friction ($C_f$) coefficients – in the gap/step case for the length to depth ($L/H$) ratio of 1/4 and the step dimensionless height $h^*$ of 3.23. It should be remarked that the gap/step case with $L/H = 1/4$, and $h^* = 3.23$ was used as a reference case. A similar procedure was employed in the grid independence study for the other cases.

### 4.6.1 Effect of the Mesh Resolution

Analogous to the numerical DSMC analysis employed for the flat-plate case in the previous section, Figures 4.11 and 4.12 display the impact on the aerodynamic surface quantities on surfaces S1/S5 and S4 (see Fig.3.2), respectively, due to the effect of the mesh resolution in the $x-$ and $y-$ direction for a coarse and fine mesh with a half less and double more cells, respectively, in comparison to the standard mesh. Table. 4.4 tabulates the number of cells employed in the eight regions for coarse, standard, and fine meshes. Again each mesh was made on non-uniform cell spacing in both directions, particularly near to the body surface in which the flow properties are more intense.

According to figures 4.11 and 4.12 there is sufficient evidence that the standard mesh of 510 x 500 cells in $x-$ and $y-$ directions, respectively, is sufficient for the present numerical investigation.

Table 4.4 - Number of cells in the (x-direction) and [y-direction] for the gap/step case.

| Region | Coarse | Standart | Fine |
|--------|--------|----------|------|
| R1 | (10)[5] | (20)[10] | (40)[20] |
| R2 | (65)[20] | (130)[40] | (260)[80] |
| R3 | (20)[50] | (40)[100] | (80)[200] |
| R4 | (20)[50] | (40)[100] | (80)[200] |
| R5 | (10)[30] | (20)[60] | (40)[120] |
| R6 | (55)[30] | (110)[60] | (220)[120] |
| R7 | (10)[30] | (20)[60] | (40)[120] |
| R8 | (65)[35] | (130)[70] | (260)[140] |
| #Cells | 7875 | 31500 | 126000 |

### 4.6.2 Effect of Variation on the Number of Simulated Particles

A similar investigation was made for the number of simulated particles variations. Figures 4.13 and 4.14 demonstrate this effect on heat transfer, pressure, and skin friction coefficients along surfaces S1, S4, and S5. The standard mesh for the gap/step geometry with $L/H = 1/4$, and $h^* = 3.23$ case corresponds to, on average, a total
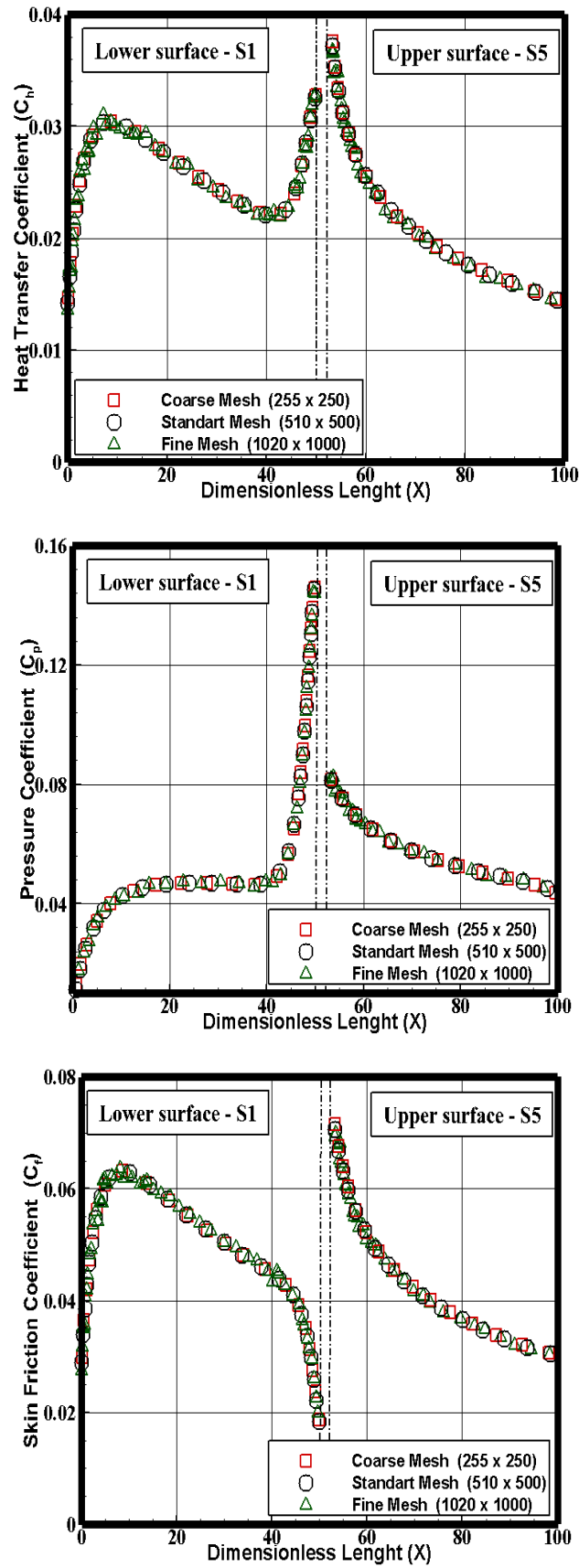
Figure 4.11 - Effect of altering the cell size in $x-$ and $y-$ direction on heat transfer (top), pressure (middle), and skin friction (bottom) coefficients along surfaces $S1$ and $S5$.

77
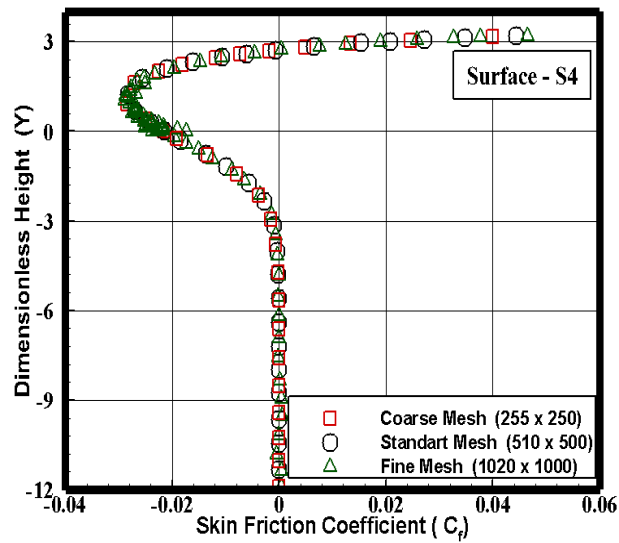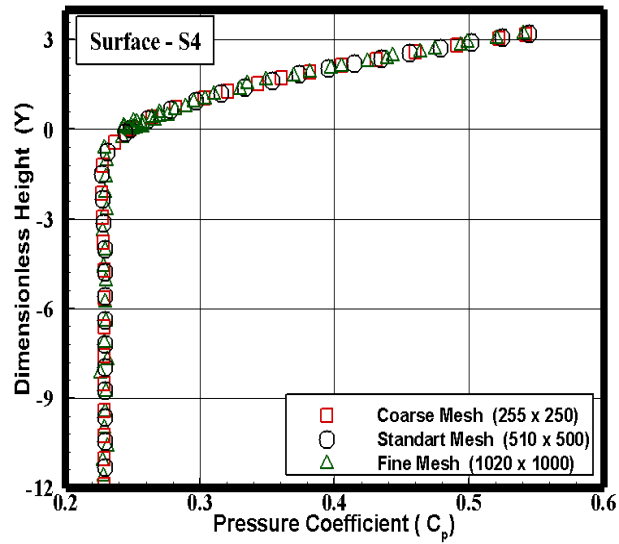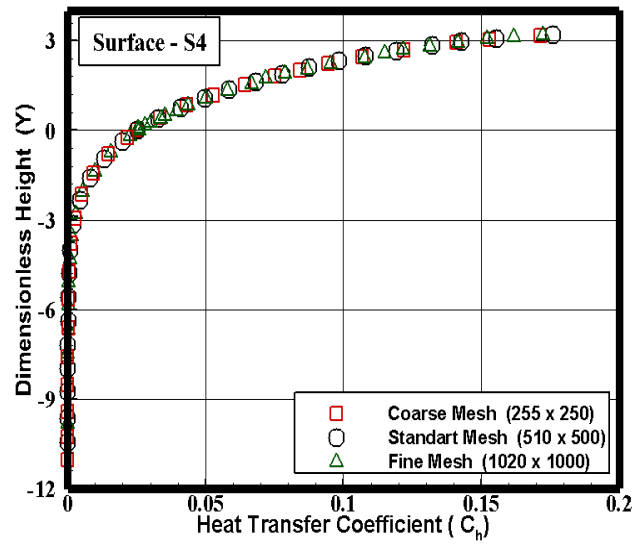
Figure 4.12 - Effect of altering the cell size in $x-$ and $y-$ direction on heat transfer (top), pressure (middle), and skin friction (bottom) coefficients along gap/step frontal face - $S4$.

78
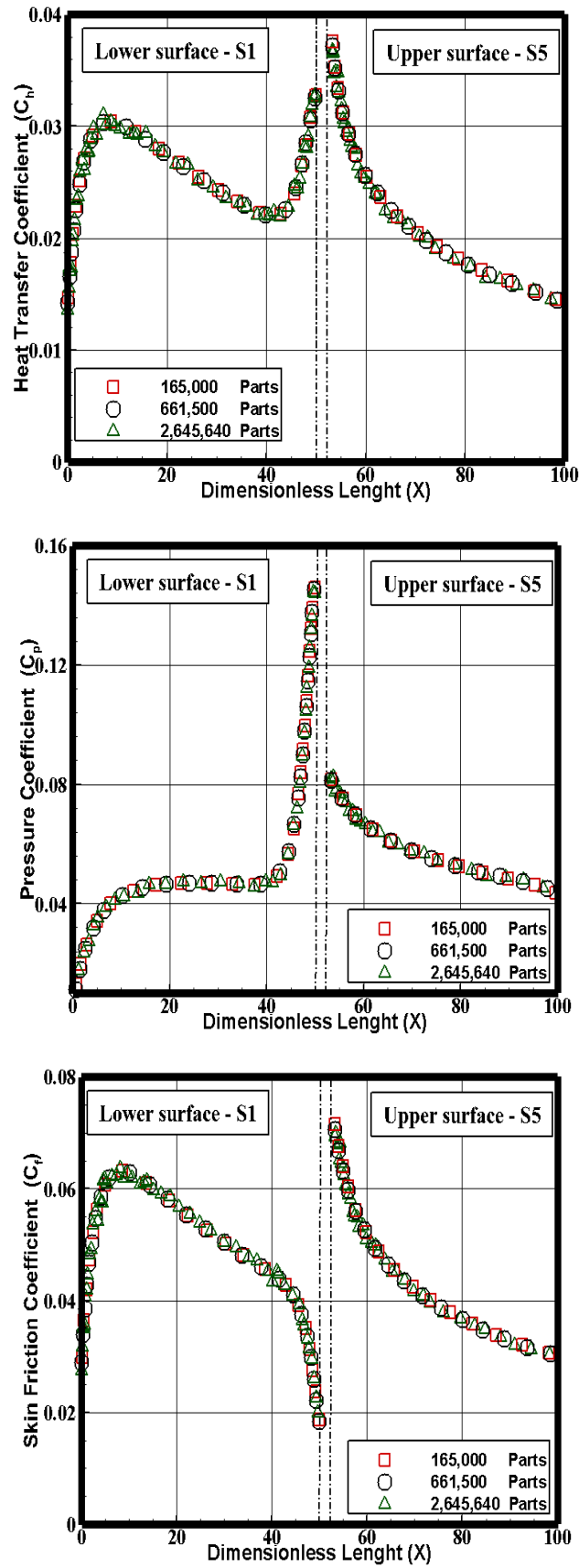
Figure 4.13 - Effect of variation on the number of simulated particles on heat transfer (top), pressure (middle), and skin friction (bottom) coefficients along surfaces $S1$ and $S5$.

79
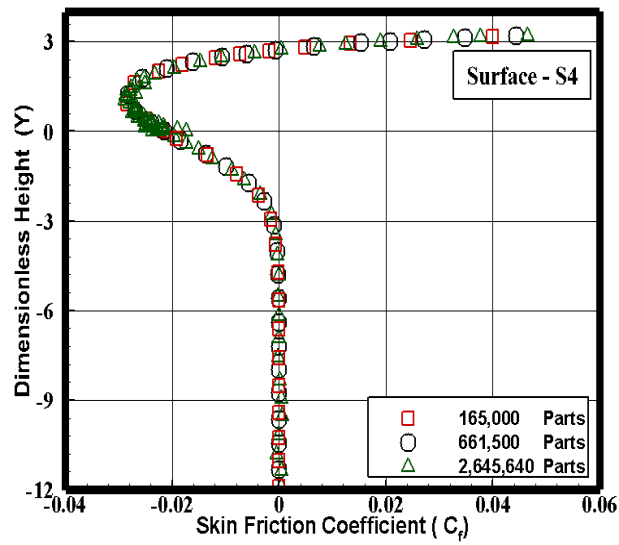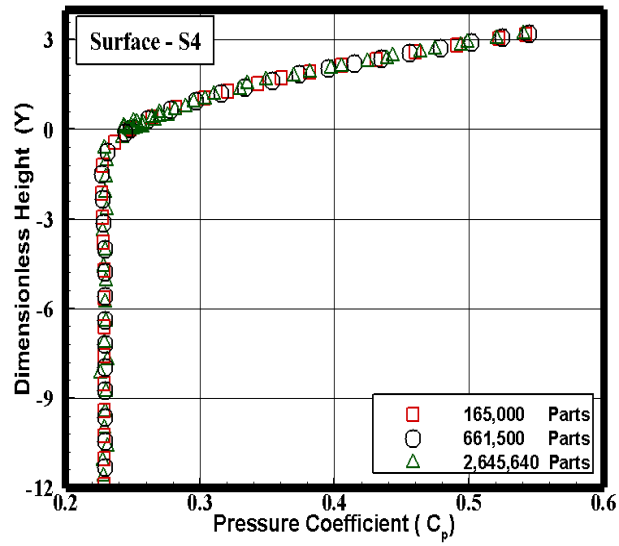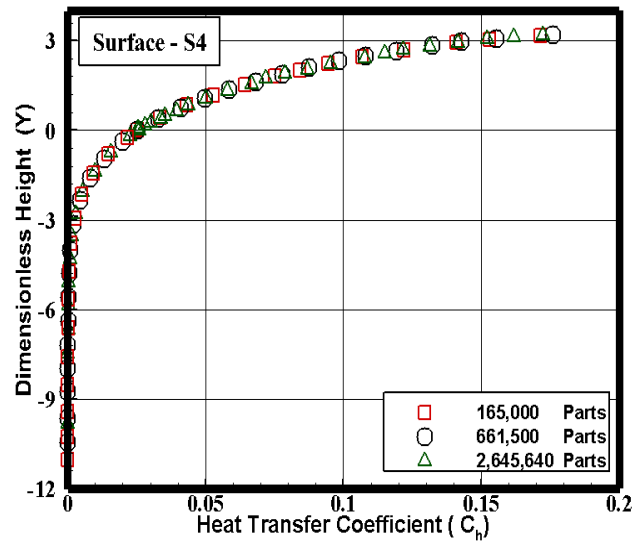
Figure 4.14 - Effect of variation on the number of simulated particles on heat transfer (top), pressure (middle), and skin friction (bottom) coefficients along gap/step frontal face - *S4*.    80

of 661,500 simulated particles. Two new cases using the same mesh were investigated. These two new cases correspond to 165,000 and 2,645,640 simulates particles in entire computational domain. Again, as the three cases presented the same results for the heat transfer $(C_h)$, pressure $(C_p)$ and skin friction $(C_f)$ coefficients, hence the standard mesh with a total of 661,500 simulated particles was considered enough for the computation of the flowfield properties. For completeness, Fig. 4.15 illustrates the standard mesh for the gap/step configuration with $L/H = 1/4$ and $h^* = 3.23$.



(a)                                    (b)
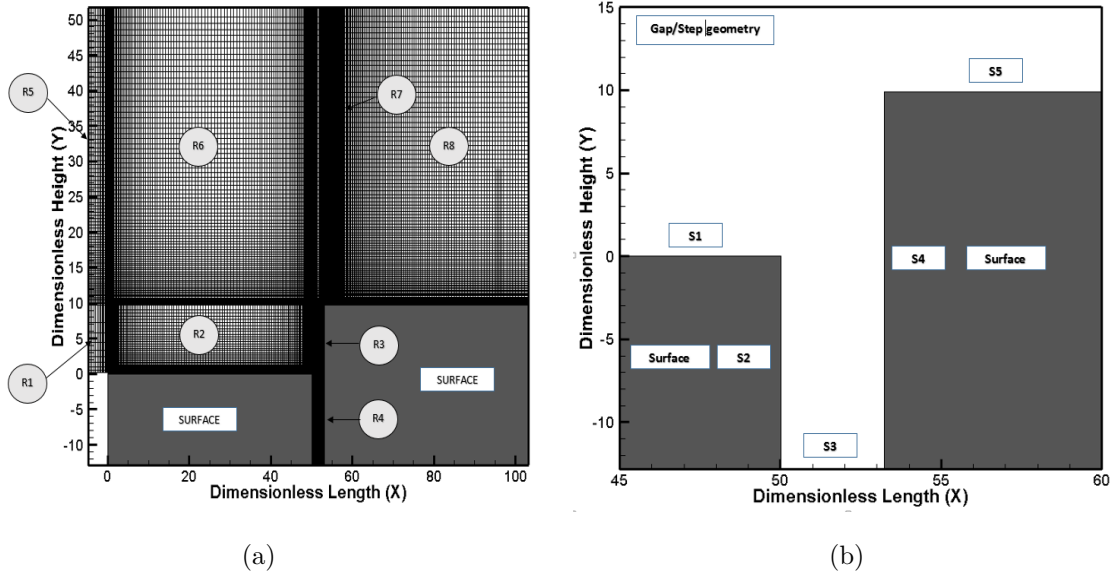
Figure 4.15 - A Drawing illustrating of the cell distribution for (a) the standard grid for the gap/step configuration with $L/H = 1/4$, and $h^* = 9.69$, and (b) the magnified view of the regions R2, R3 and R4.

# 5 COMPUTATIONAL RESULTS AND DISCUSSION

Having computed flowfield and surface properties over a wide range of simulation parameters, it proves instructive to summarize the major features of the results. Consequently, the purpose of this chapter is to discuss and compare differences in the flowfield properties, and in the aerodynamic surface quantities due to variations on the gap $L/H$ ratio and on the step frontal-face height $h$, for the combined gap/step geometry.

## 5.1 Flowfield Properties

This subsection focuses on the calculations of the primary properties obtained from DSMC results. The primary properties of particular interest in this work are velocity, density, pressure, and kinetic temperature.

### 5.1.1 Velocity Profiles

The DSMC method is essentially a statistical method. In this method, the macroscopic properties are computed as averages from the microscopic properties in each cell in the computational domain. As a result, the velocity vector is given by the following expression:

$$\mathbf{c}_0 = \frac{\sum_{j=1}^{N}(m\mathbf{c})_j}{\sum_{j=1}^{N} m_j} \tag{5.1}$$

where $N$, $m$ and $\mathbf{c}$ represent, respectively, the number of molecules, the molecular mass and the velocity vector of the molecules in each cell. It should be noted that the mean molecular velocity $\bar{\mathbf{c}}$ ($\equiv \mathbf{c}_0 = u\vec{i} + v\vec{j} + w\vec{k}$) defines the macroscopic mean velocity. It is also important to mention that the velocity of the molecule relative to the mean macroscopic velocity, defined as thermal or peculiar velocity, is denoted by $\mathbf{c'} \equiv \mathbf{c} - \mathbf{c}_0$.

Before proceeding with the analysis, it is instructive to first examine the boundary-layer thickness $\delta$ for the flat-plate case, without a combined gap/step, employed as a benchmark in this investigation. The boundary-layer thickness was obtained by considering the condition $u/U_\infty \approx 0.99$, where $u$ is the tangential velocity, i.e., the velocity component in the $x$-direction. It was found that $\delta/\lambda_\infty = 17.76$ for a distance of $53.23\lambda_\infty$ from the sharp leading edge. Consequently, the boundary-layer thickness is larger than the step height $h^*$ of 3.23, 6.46, and 9.69, a flow feature of particular interest in the present study.

### 5.1.1.1 Gap $L/H$ Ratio Effect

Figure 5.1 displays the velocity ratio $u/U_\infty$ profiles for three sections along surface S1 (upstream surface) in a combined gap/step configuration. In this set of plots, filled and empty symbols correspond to the dimensionless step height $h^*$ of 3.23 and 9.69, respectively, $X$ represents the distance $x$ from the sharp leading edge normalized by $\lambda_\infty$, and $Y$ the distance $y$ above surface S1 also normalized by $\lambda_\infty$. The combined gap/step case with the dimensionless step height $h^*$ of 6.46 is a intermediate case, and results for this case will not be shown in these plots.

According to these plots, it is clearly noticed that the gap $L/H$ ratio investigated did not affect the tangential velocity profiles along surface S1, since for each upstream section considered ($X = 39$, 44, and 48), the tangential velocity profiles ($u/U_\infty$) are quite similar.

Figure 5.2 displays the tangential velocity ratio $u/U_\infty$ profiles for three sections inside the gaps, along surface S3. In this set of plots, again filled and empty symbols correspond to the dimensionless step height $h^*$ of 3.23 and 9.69, respectively, $X'_L$ represents the distance $(x - L_u - L/2)$ normalized by the gap length $L$, and $Y_H$ is the height $y$ above surface S3 normalized by the gap depth $H$. Again, results for the case with dimensionless step height $h^*$ of 6.46 will not be shown in these plots. It is clearly seen from these figures, that changes on gap $L/H$ ratio, and on step frontal-face height $h$, affect the flowfield inside the gap in a combined gap/step configuration. It is evident from these plots that: (1) as the gap $L/H$ ratio decreases, the clockwise recirculation region that before fills the entire gap for the $L/H$ ratio of 1 do not reach the bottom surface of the gap, and (2) as the step height $h^*$ increases, the clockwise recirculation region inside the gap tends to go outside, inducing a second recirculation region in a opposite direction inside the gap.

Finally, before looking at the other flowfield properties in more detail, a brief consideration of the parameters involved is in order. It is quite apparent from Fig. 5.1 that changes on the gap $L/H$ ratio did not affect the tangential velocity profiles along surface S1, for the range of values investigated in this work. Conversely, changes in the step frontal-face $h$ is of great importance along surface S1. In this framework, in the analysis of the step frontal-face thickness effect, the gap $L/H$ of 1 will be considered as the reference case.
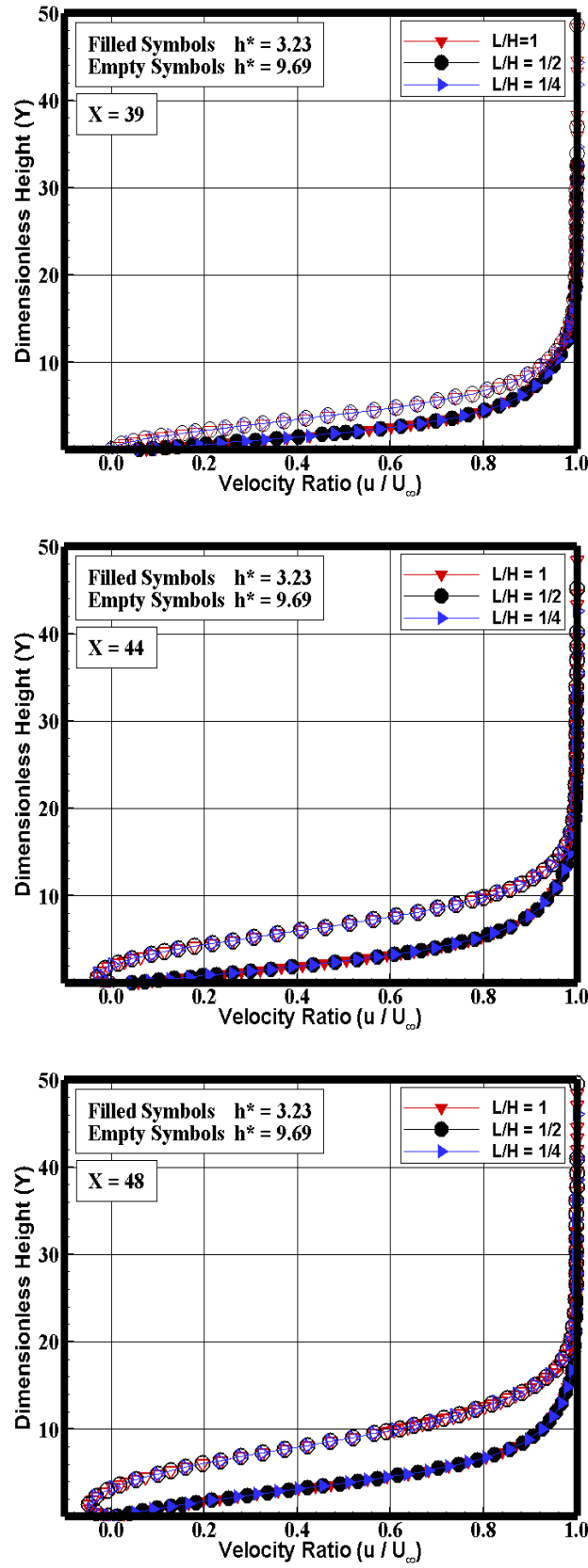
Figure 5.1 - Distribution of tangential velocity ($u/U_\infty$) profiles for three sections along surface S1, defined by section $X$ of 39 (top), 44 (middle), and 48 (bottom).
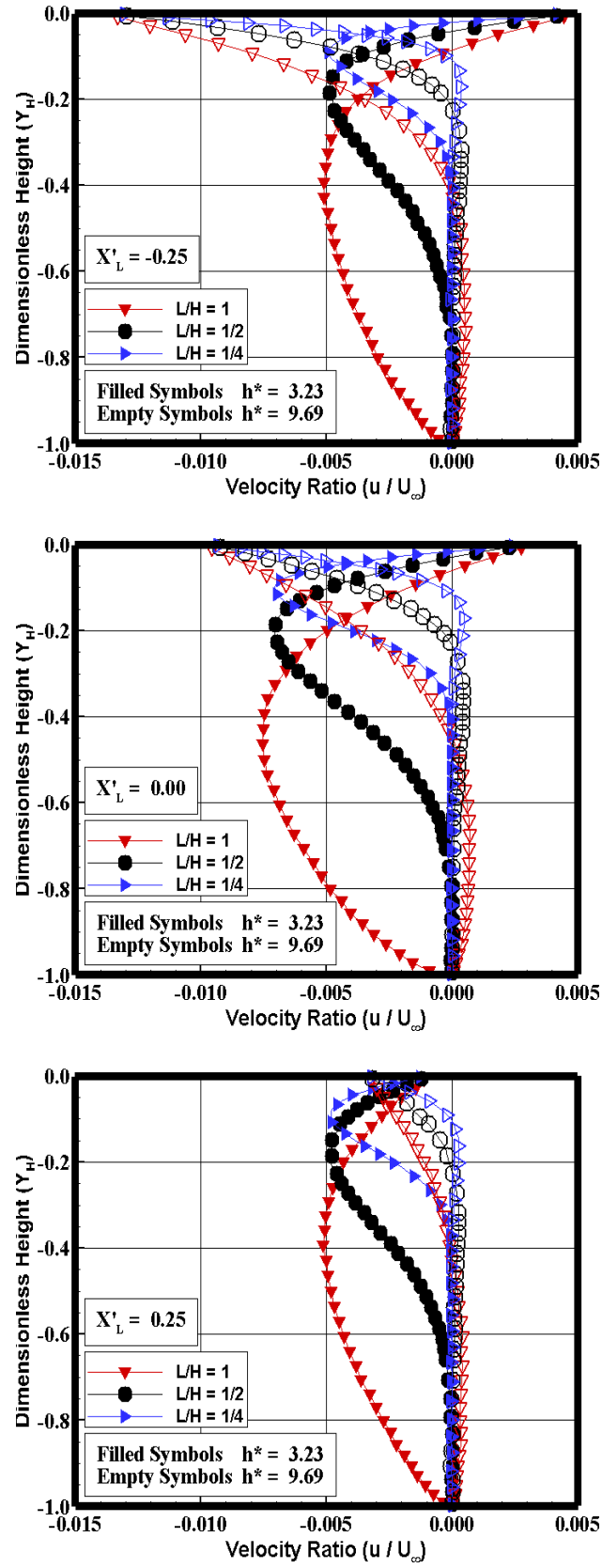
Figure 5.2 - Distribution of tangential velocity ($u/U_\infty$) profiles for three sections along surface S3, defined by section $X'_L$ of -0.25 (top), 0.00 (middle), and 0.25 (bottom).

### 5.1.1.2 Step Frontal-face Thickness Effect

The distribution of the tangential velocity ratio $u/U_\infty$ profiles for three sections along surface S1 is illustrated in Fig. 5.3 for the gap $L/H$ ratio of 1, parameterized by the dimensionless step height $h^*$. Again in these plots, filled and empty symbols correspond to the dimensionless step height $h^*$ of 3.23 and 9.69, respectively. As a basis of comparison, the tangential velocity ratio profiles for the forward-facing step (S) (LEITE, 2009), the gap (G) (PAOLICCHI, 2011), and the flat-plate (FPL) (LEITE; SANTOS, 2011) cases are also illustrated in the same set of plots. It is important to mention that the tangential velocity ratio profiles for $h^* = 6.46$ case are intermediate to the other two cases, and therefore, they will not be shown.

According to Fig. 5.3, it is observed that changes in the step height $h$ affect the flowfield far upstream, as was expected. It is found that changes in the step height for the gap/step configuration were less intense than those observed for the step case alone, i.e., the forward-facing step case. In this sense, for section $X = 39$, the velocity profiles for the gap, step, and gap/step configuration, defined by $h^* = 3.23$, are basically identical, by visual inspection, to those for the flat-plate case. It means that no effect of the presence of the step or the gap is observed up to this section. Conversely, for $h^* = 9.69$ case, the presence of the gap/step configuration is felt far upstream along surface S1. Moreover, for section $X \geq 44$, the upstream disturbance caused by the step or by the gap/step configuration is observed on the velocity profiles for the frontal-face height $h$ investigated. In addition, it is observed that the velocity profiles are affected more upstream with increasing the frontal-face height $h$. This behavior results from the diffusion of molecules that are reflected from the frontal-face of the step. Also, for sections $X \geq 44$, the velocity profiles related to the steps indicate negative velocities close to surface S1, characterizing a recirculation region at the vicinity of the step frontal-face. For section $X = 39$, negative velocity occurs only for the step height $h^* = 9.69$ case, and for section $X = 48$, for the three frontal-face heights investigated, as displayed by the magnified view shown in the right column of Fig. 5.3.

Another flow peculiarity is with respect to the tangential velocity at station $Y \approx 0$. It is clearly seen from Fig. 5.3 that $u/U_\infty \neq 0$ for $Y \approx 0$, a characteristic of a rarefied flow regime. As a result, the condition of $u/U_\infty = 0$ at the body surface, no-slip velocity in the continuum flow regime, is not applied in a rarefied flow. The slip-velocity occurs due to the relatively low number of collision experienced by a gas at high $Kn$, meaning that the average velocity at the wall has a finite value.
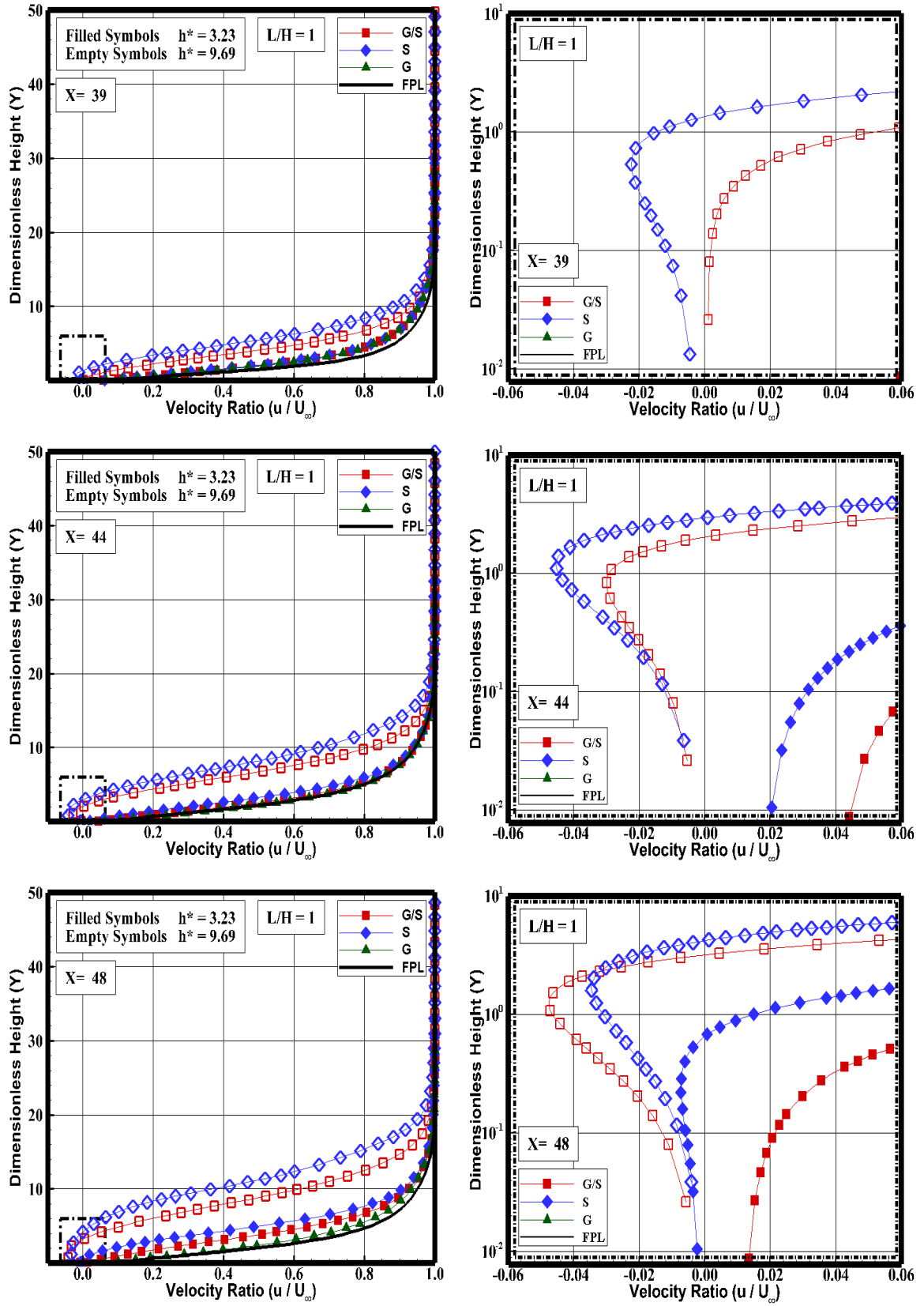
Figure 5.3 - Distribution of tangential velocity ($u/U_\infty$) profiles for three sections along surface S1 for gap/step configuration with $L/H$ ratio of 1, defined by section $X$ of 39 (top), 44 (middle), and 48 (bottom).

Consequently, this phenomenon reduces shear stress and may affect the boundary layer separation (BOYD, 2014).

Tangential velocity ratio $u/U_\infty$ profiles inside the gaps in a combined gap/step configuration are demonstrated in Fig. 5.4 for three sections $X'_L$. In this set of diagrams, the tangential velocity ratio $u/U_\infty$ is displayed as a function of the dimensionless height $Y_H$, i.e., the height $y$ normalized by the gap depth $H$. In addition, diagrams in the left column present the profiles for $L/H$ of 1, and right column profiles for $L/H$ of 1/4. For comparison purpose, profiles for the gap case investigated by Paolicchi (PAOLICCHI, 2011) are also displayed in these diagrams. The gap case with $L/H$ of 1/2 is considered as a intermediate case, and therefore, data for this case will not be shown.

On examining Fig. 5.4, it is seen that for the gap case (PAOLICCHI, 2011) with $L/H$ ratio of 1, it appears just one recirculation region in the clockwise direction and that this recirculation region fills the entire gap. Otherwise, in a gap/step configuration with the gap $L/H$ of 1, due the presence of the step, this recirculation region becomes less intense within the gap. In addition, it is also seen that, as the gap $L/H$ ratio decreases, this recirculation region did not reattach the bottom surface of the gap.

Normal velocity profiles inside the gap in a combined gap/step geometry, with the gap $L/H$ ratio of 1 and 1/4, are displayed in Fig. 5.5, for three sections as a function of the distance $X'_L$. In this set of plots, the normal velocity $v$ is normalized by the freestream velocity $U_\infty$, and the three sections $Y'_H$ correspond to the transversal sections $(y + H)$ normalized by the gap depth $H$, i.e., $Y'_H$ of 0.25, 0.50, and 0.75.

According to these plots, it is seen that the flow inside the gap, in a combined gap/step configuration and in the gap case (without a step), present positive values (moving upward) in the normal velocity ratio profiles in the first half of the gap ($X'_L < 0$), and negative values (moving downward) in the second part of the gap ($X'_L > 0$). Therefore, based on these two opposite behaviors for the normal velocity ratio, it may be inferred in passing that there is a region of clockwise recirculation flow inside the gap. Also, as the step frontal-face height $h^*$ increases to 9.69, the normal velocity ratio profiles present an opposite behavior, indicating that the flow inside the gap in a combined gap/step is in a counterclockwise direction. Finally, it is also seen that, as the gap $L/H$ decreases, the normal velocity $v$ component is zero for positions bellow $Y'_H = 0.50$, indicating that there is no recirculation region at the vicinity of the gap floor for theses cases.
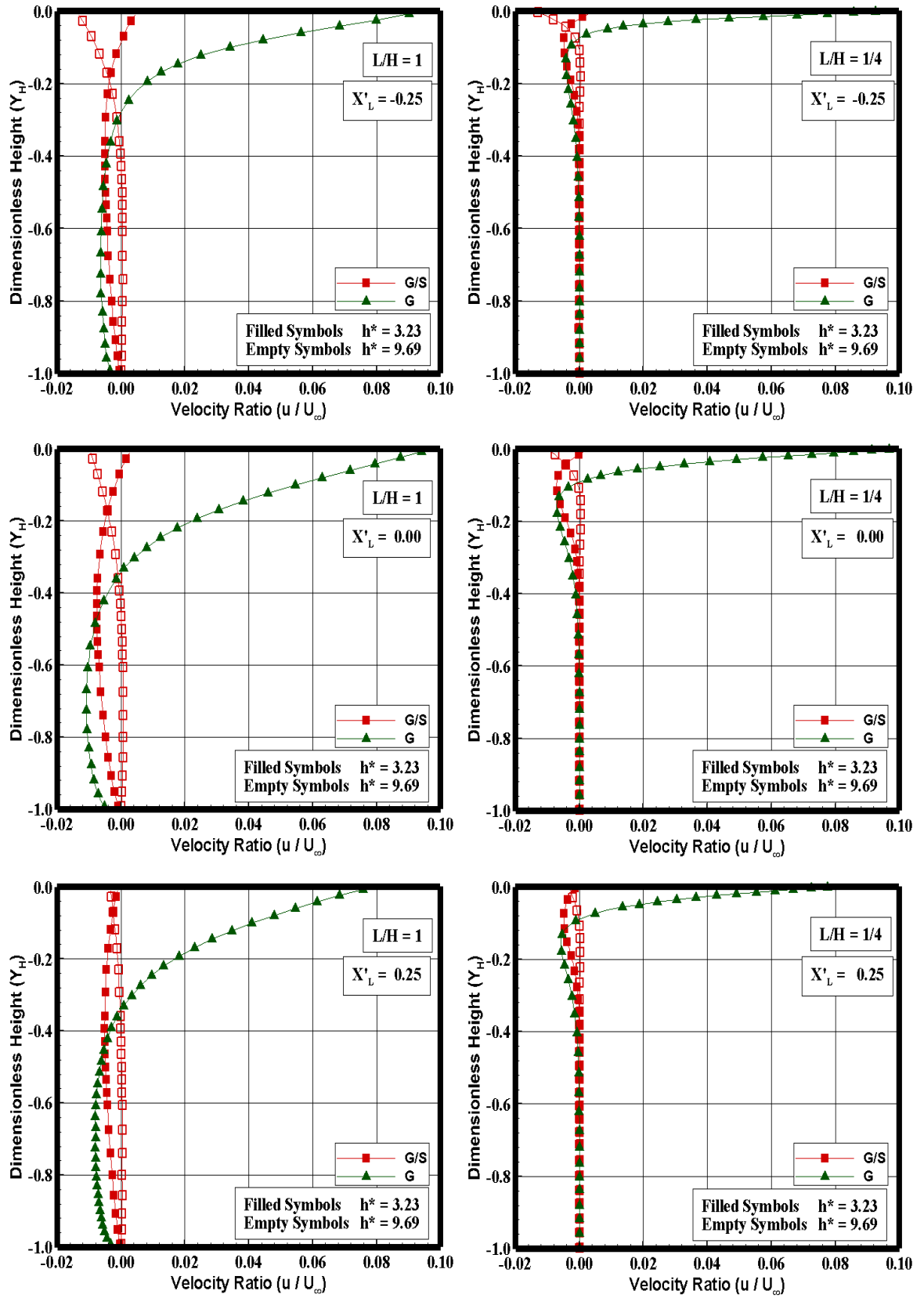
Figure 5.4 - Tangential velocity ratio ($u/U_\infty$) profiles inside the gap with $L/H = 1$ (left column), and $L/H = 1/4$ (right column), for three sections along surface S3 in a combined gap/step configuration, defined by section $X'_L$ of -0.25 (top), 0.00 (middle), and 0.25 (bottom).
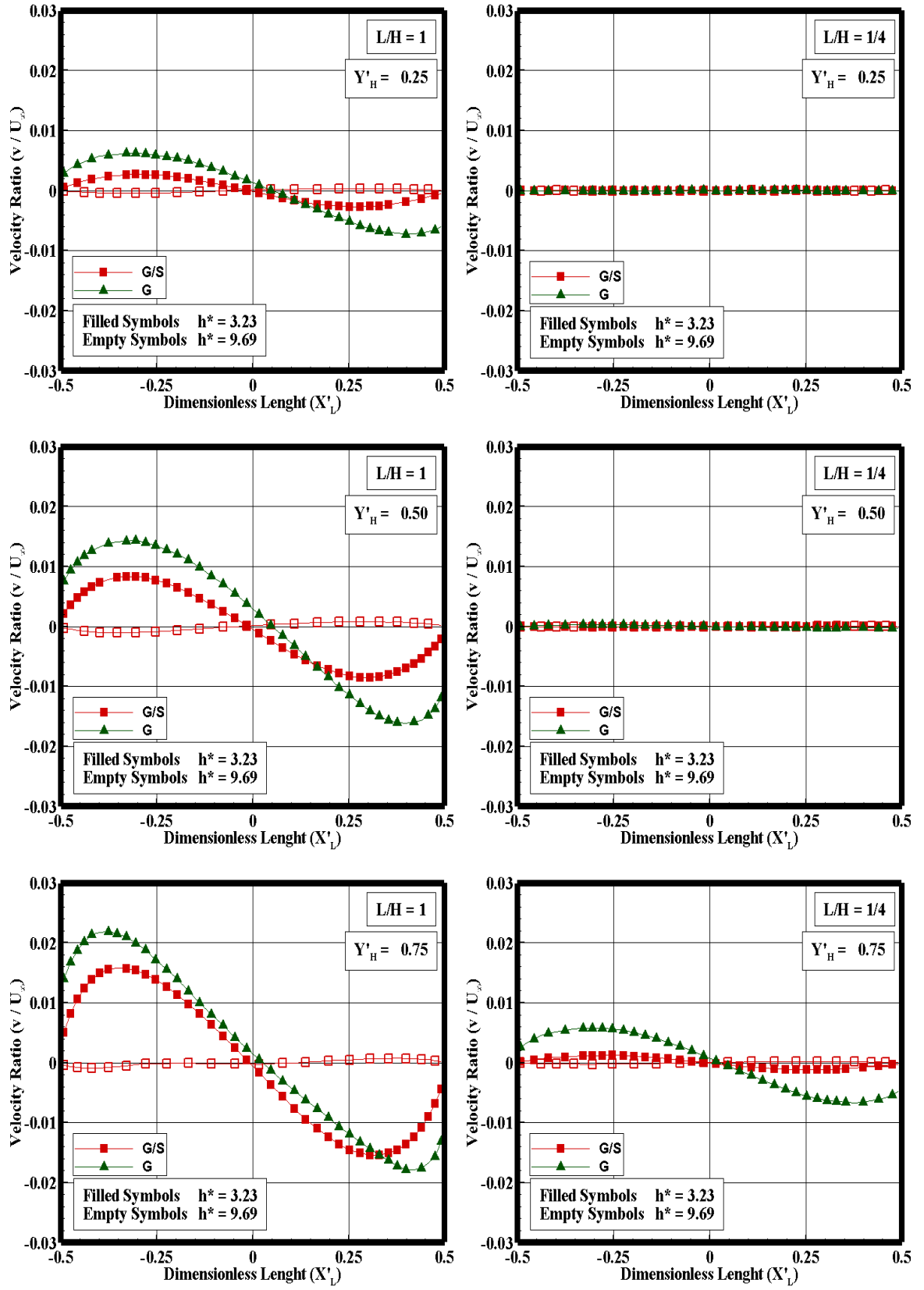
Figure 5.5 - Normal velocity ratio ($v/U_\infty$) profiles inside the gaps, with $L/H = 1$ (left column), and $L/H =$1/4 (right column), for three transversal sections in a combined gap/step configuration, defined by section $Y'_H$ of 0.25 (top), 0.50 (middle), and 0.75 (bottom).
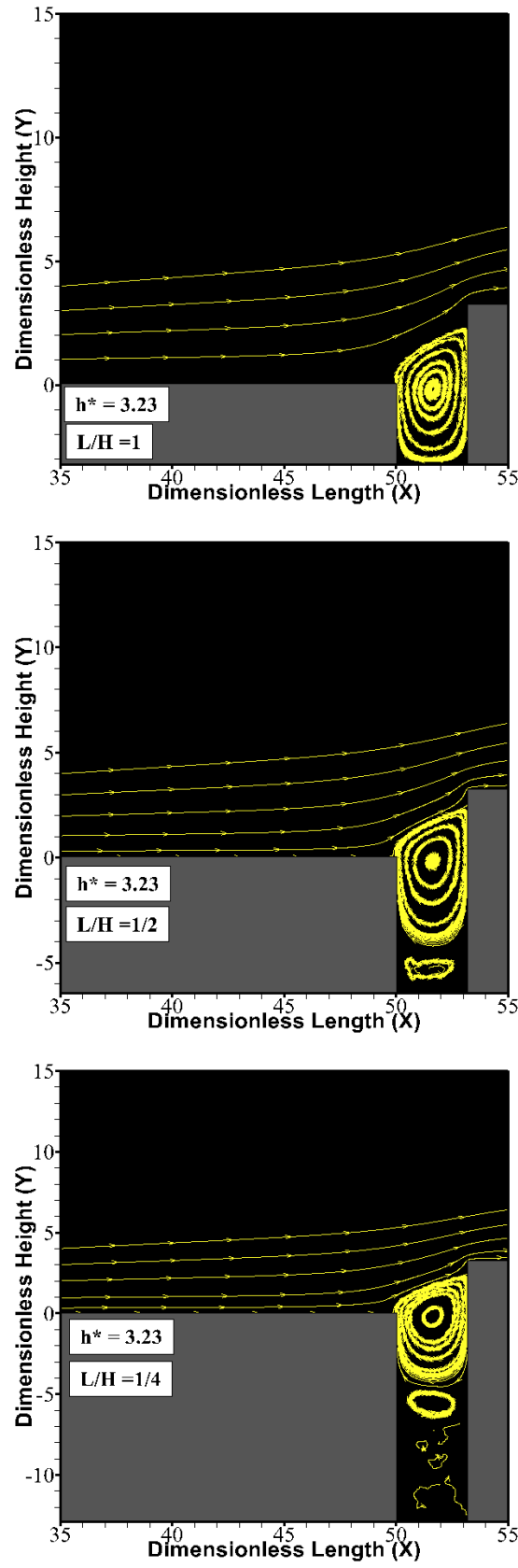
Figure 5.6 - Distribution of streamline traces around the combined gap/step geometry with frontal-face thickness $h^* = 3.23$ and $L/H$ of 1 (top), 1/2 (middle), and 1/4 (bottom).
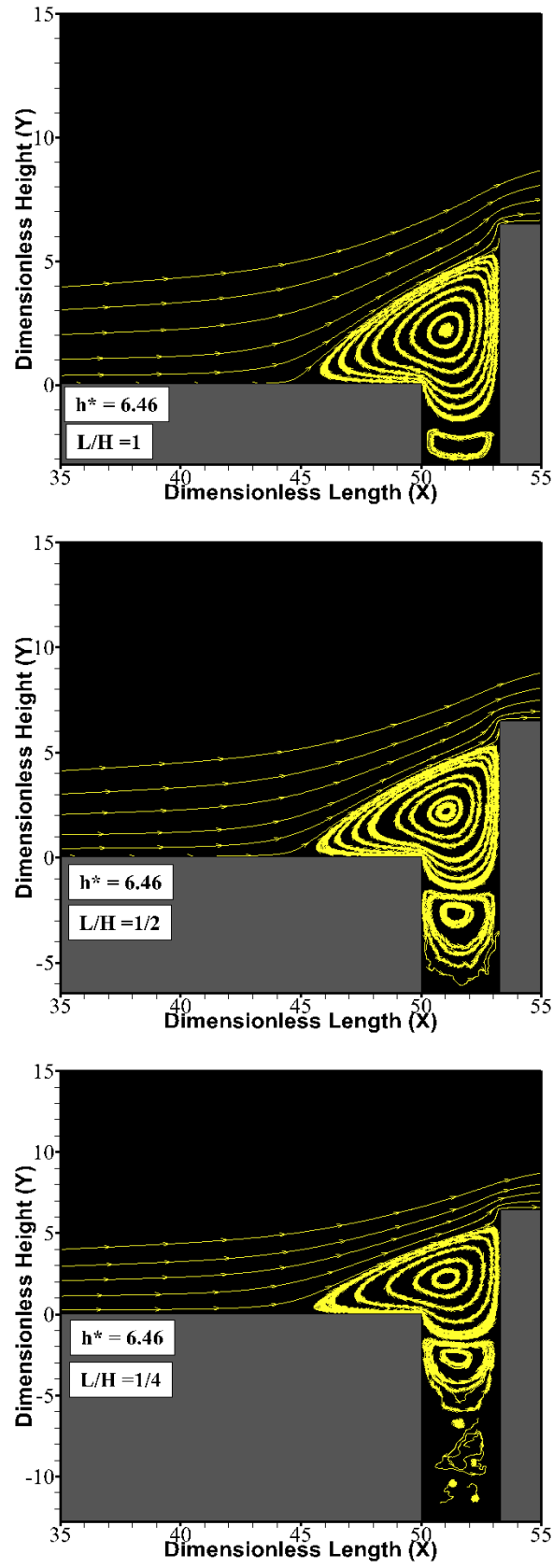
Figure 5.7 - Distribution of streamline traces around the combined gap/step geometry with frontal-face thickness $h^* = 6.46$ and $L/H$ of 1 (top), 1/2 (middle), and 1/4 (bottom).
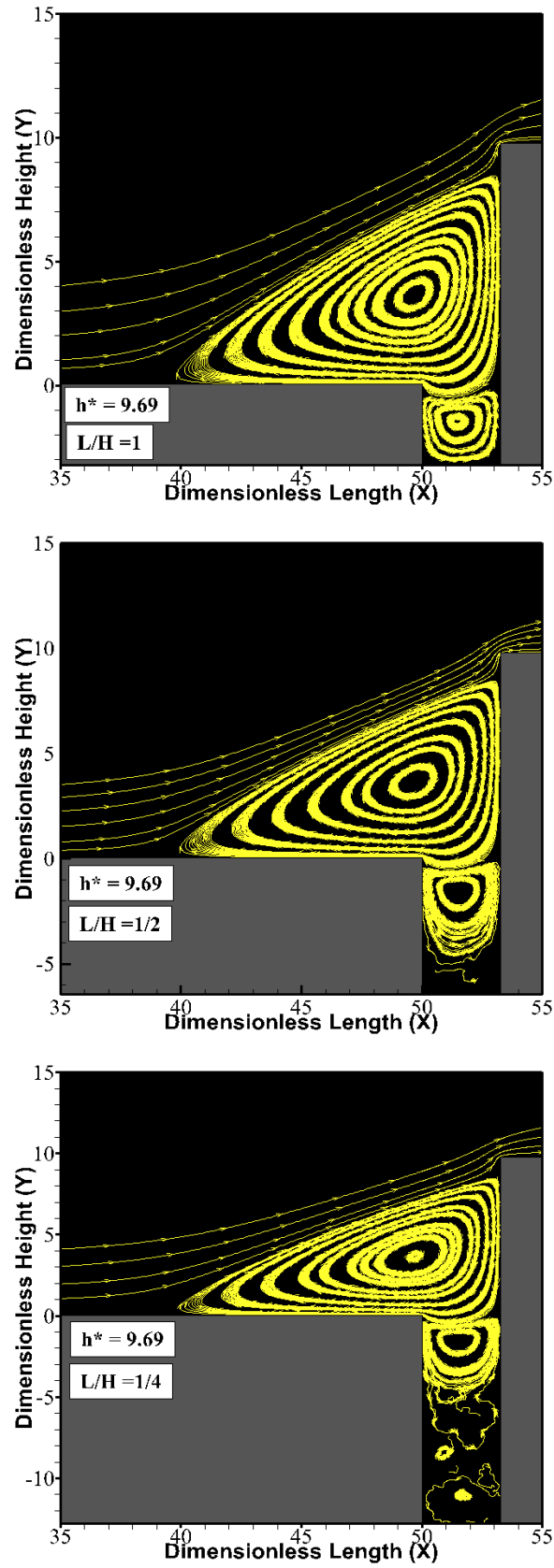
Figure 5.8 - Distribution of streamline traces around the combined gap/step geometry with frontal-face thickness $h^* = 9.69$ and $L/H$ of 1 (top), 1/2 (middle), and 1/4 (bottom).

In a effort to emphasize points of interest related to the velocity field, Figs. 5.6, 5.7, and 5.8 display the flow topology with streamline traces around the combined gap/step configuration with step frontal-face height $h^*$ of 3.23, 6.46 and 9.69, respectively, and with gap $L/H$ ratio of 1, 1/2, and 1/4. It may be recognized from this set of plots that, in general, a recirculation region appears ahead of the step, in which the flow goes in the clockwise direction, and another one inside the gap, in which the flow goes in the counterclockwise direction. For the particular gap/step case with $h^* = 3.23$ and $L/H = 1$, just one recirculation region appears inside the gap, which fills entirely the gap. In addition, as the $L/H$ ratio decreases, another recirculation region appears inside the gap with the flow in the opposite direction.

Another flow peculiarity is related to the step height effects on the recirculation region. Based on Figs. 5.6, 5.7, and 5.8, there is sufficient evidence that, as the step height $h^*$ increases from 3.23 to 9.69, the primary recirculation region (in the clockwise direction) inside the gap tends to move outside the gap, inducing another recirculation inside the gap in a counterclockwise direction. As a consequence, a recirculation region is clearly seen in front of the step frontal-face and this recirculation region increases with increasing the step height $h^*$. This behavior is quite similar to the forward-facing step (without a gap) case, that was investigated by Leite (LEITE, 2009), for the same freestream and flow conditions.

A rarefied hypersonic flow inside a gap, without a step, was investigated by Paolicchi (PAOLICCHI, 2011), considering the same freestream and flow conditions, as tabulated in Tabs. 3.1 and 3.2. For comparison purpose, streamline traces inside a gap with a $L/H$ ratio of 1, 1/2, and 1/4 are depicted in Fig. 5.9.

Looking to Fig. 5.9, it is clearly seen that flow within the gaps is characterized by a primary recirculation region. For the cases with $L/H$ ratio of 1 and 1/2, it is observed that the recirculation region fills the gaps completely. Conversely, for the $L/H$ ratio of 1/4, the recirculation region does not fill the entire gap. Furthermore, the flow exhibits an irregular or chaotic structural motion in the second half portion of the gap, more precisely for $Y < -7$. Finally, for the three cases investigated by Paolicchi (PAOLICCHI, 2011), the external stream does not reattach at the bottom surface of the gap. It should be mentioned in this context that the gap flow topology observed by Paolicchi (PAOLICCHI, 2011) in a rarefied environment differs from that usually observed in the continuum flow regime. In the continuum flow regime, the gap flow topology is defined by the development of a column of counter-rotating vortices within the gap caused by the main stream flow, where the number of vor-
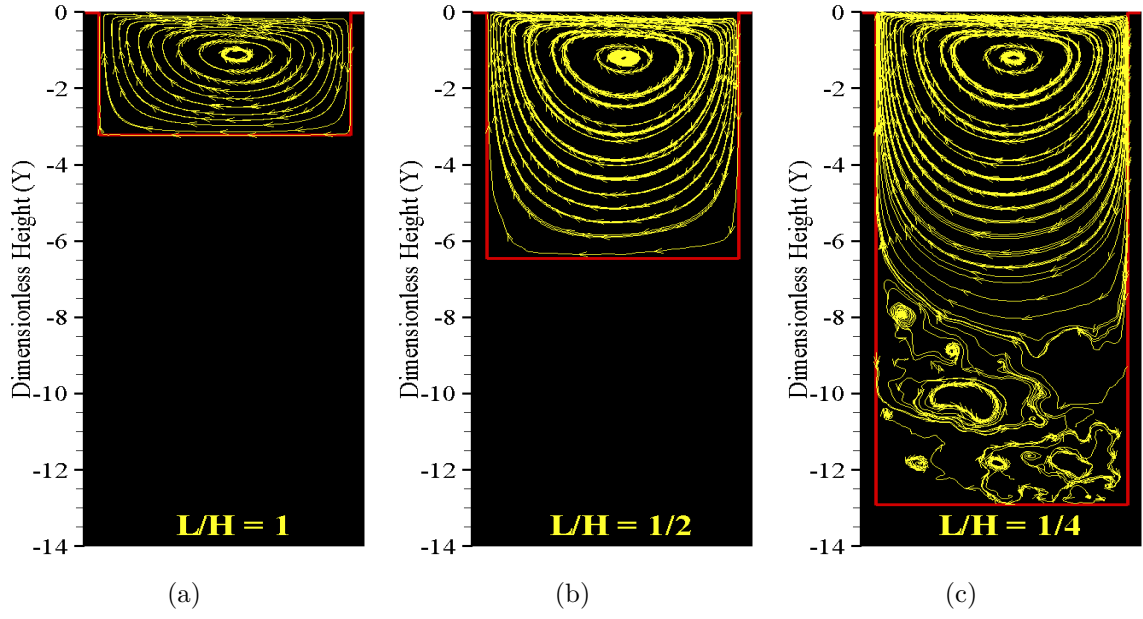
Figure 5.9 - Distribution of streamline traces inside the gaps with $L/H$ ratio of (a) 1, (b) 1/2, and (c) 1/4.

tices is approximately given by $H/L$ ratio. In addition, alternating hot spots are developed in the gap when the vortices directionally align and impinge on the gap sidewall (EVERHART et al., 2006).

In the following, as a base of comparison, forward-facing step streamlines traces of a rarefied hypersonic flow over forward-facing step with step height $h^*$ of 3.23, 6.46 and 9.69, investigated by Leite (LEITE, 2009), are displayed in Fig. 5.10. It is clearly noticed from this plots that a recirculation region appears at the vicinity of the step frontal-face surface. It may be inferred by visual inspection that the recirculation region increases with increasing the step height not only along the upstream surface, but also along the step frontal-face surface.

By the time being, it is instructive to examine the differences between the separation and reattachment points for a gap/step configuration (Figs. 5.6, 5.7, and 5.8), from those for the forward-facing step (Fig. 5.10). From this set of plots, by visual inspection, it is seen the recirculation region increases in front of the frontal-face. As a consequence, the separation point on surface S1 ahead the gap/step configuration is strongly influenced by the step frontal-face height $h$. On the other hand, the reattachment point on the step frontal-face, surface S4, of the combined gap/step geometry has small differences in comparison with that for the step case alone. Also, both the separation and the reattachment points on these surfaces did not change
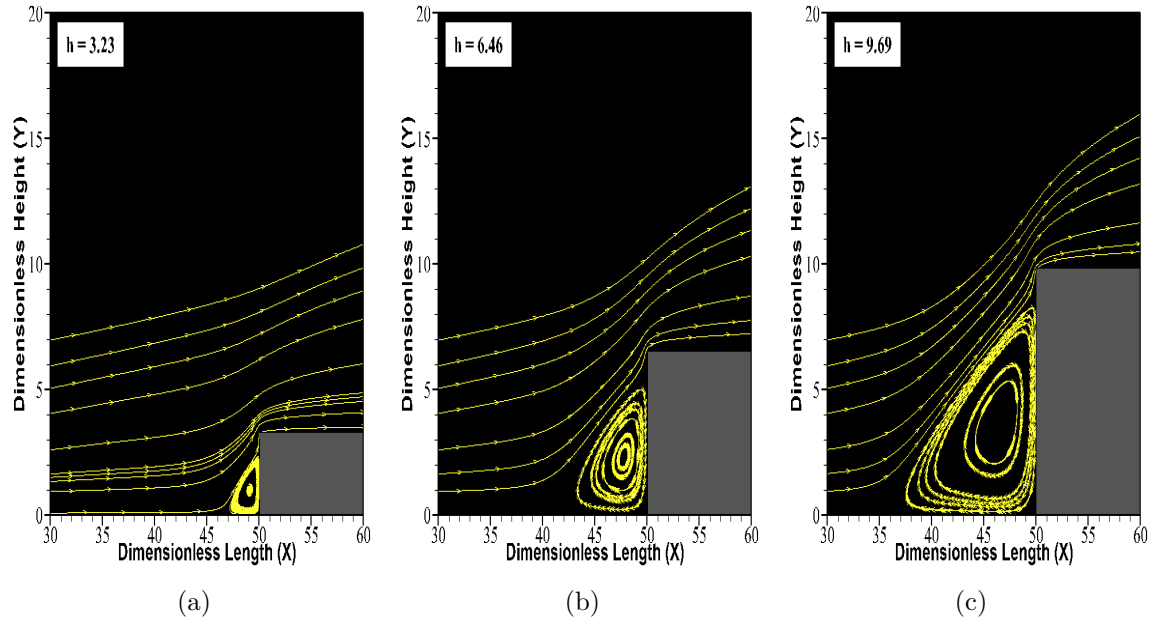
Figure 5.10 - Distribution of streamline traces around the steps with frontal-face thickness $h^*$ of (a) 3.23, (b) 6.46 and (c) 9.69.

for the range of the gap $L/H$ ratio investigated.

For comparison purpose, Tab. 5.1 tabulates the separation point on surface S1, and the reattachment point on the step frontal-face, surface S4, by considering the gap $L/H$ ratio and the step height $h^*$ of a combined gap/step geometry. In Tab.5.1, $X_s$ and $Y_r$ represent, respectively, the distances $x$ and $y$, normalized by the mean free path $\lambda_\infty$, and the subscripts $s$ and $r$ refer to the separation and reattachment points, respectively.

According to this table, it is noticed that the separation point $X_s$ for the gap/step configuration increases in comparison with that for the forward-facing step. In addition, $X_s$ decreases by increasing the step height $h$. The reason for that is because the upstream disturbance increases with increasing the step height. Conversely, no appreciable changes are observed for the reattachment point $Y_r$ for the gap/step configuration when compared to that for the forward-facing step.

Finally, it is seen from Tab. 5.1 that the recirculation region ahead of the combined gap/step is less intense in comparison with the recirculation region of the step case alone. The results show that the separation point moved away from the step as the step height increased, as observed by Rogers and Berry (ROGERS; BERRY, 1965).

97

It is important to remark that the separation point $X_s$ and the reattachment point $Y_r$ were obtained on the basis of zero skin friction coefficient, $C_f = 0$ (or wall shear stress $\tau_w = 0$). The reason for that is because the skin friction coefficient along a surface changes from a positive value to a negative value at separation and vice-versa at reattachment, as pointed out by Kim and Setoguchi (KIM; SETOGUCHI, ) and Deepak et al. (DEEPAK et al., ), and employed by Schafer et al. (SCHÄFER et al., 2009), Ji and Wang (JI; WANG, 2010), and Ji and Wang (JI; WANG, 2012). Hence, it is a good indication of the position of separation at the upstream surface and reattachment at the step frontal-face surface.

Table 5.1 - Comparison of separation and reattachment points for the gap $L/H$ ratio of $[L/H = 1],(L/H = 1/2)$, and $<L/H = 1/4>$ in a gap/step configuration (G/S) and forward-facing step (S), as a function of the step frontal-face height ($h^*$).

| $h^*$ | $X_s$ (G/S) | $X_s$ (S) | $Y_r$ (G/S) | $Y_r$ (S) |
|-------|-------------|-----------|-------------|-----------|
| 3.23 | [50.00] (50.00) <50.00> | 48.33 | [2.73] (2.72) <2.73> | 2.63 |
| 6.46 | [46.37] (46.38) <46.38> | 42.86 | [5.59] (5.59) <5.60> | 5.61 |
| 9.69 | [40.61] (40.62) <40.62> | 37.34 | [8.68] (8.68) <8.68> | 8.70 |

### 5.1.2 Density Field

The density in each cell in the computational domain is obtained by the following expression,

$$\rho = \frac{1}{V_c} \sum_{j=1}^{N} m_j \qquad (5.2)$$

where $N$ is the number of molecules in the cell, $m$ is the molecular mass and $V_c$ is the volume of the cell.

#### 5.1.2.1 Gap $L/H$ Ratio Effect

Density ratio ($\rho/\rho_\infty$) profiles for three sections along surface S1 in a combined gap/step configuration are demonstrated in Fig. 5.11. Due to the large range of variation for the ratio $\rho/\rho_\infty$ along surface S1, the scale in the x-direction differs from one plot to another. It is firmly established from Fig. 5.11 that the gap $L/H$ ratio changes do not affect the density ratio profiles ahead the combined gap/step geometry, since for each section considered, the density ratio profiles are quite similar.
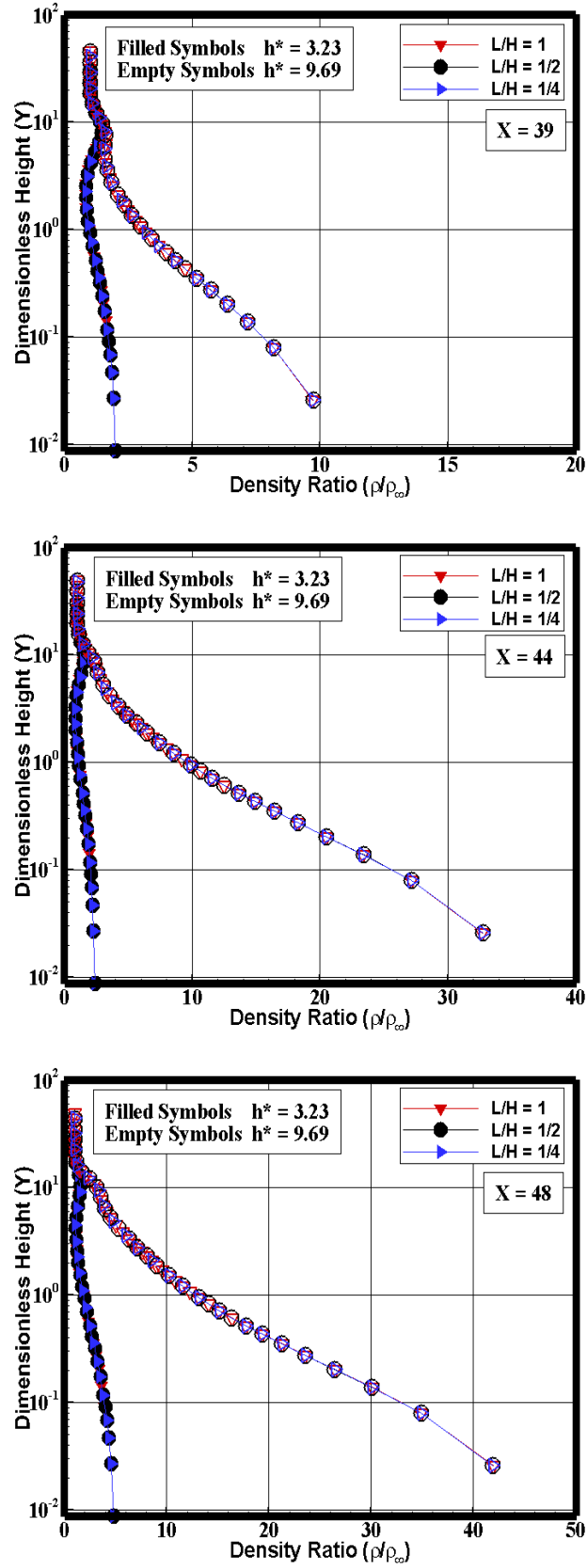
Figure 5.11 - Density ratio ($\rho/\rho_\infty$) profiles for three sections along surface S1 in a combined gap/step configuration, defined by section $X$ of 39 (top), 44 (middle), and 48 (bottom).

Figure 5.12 displays the density ratio $\rho/\rho_\infty$ profiles for three sections $X'_L$ along surface S3, parameterized by the gap $L/H$ ratio. Again $Y_H$ is the height $y$ above surface S3 normalized by the gap depth $H$. From these plots, it may be recognized that the density inside the gap increases from the top to the bottom of the gaps for the $L/H$ ratio investigated. It is quite apparent that the density ratio tends to a constant value at the bottom of the gap with decreasing the $L/H$ ratio. It is also seen that the density inside gap dramatically increases with the step height increase. For comparison purpose, the density ratio at the bottom surface of the gap is approximately 25 and 70 times the freestream density for the step height $h^*$ of 3.23 and 9.69, respectively.

### 5.1.2.2 Step Frontal-face Thickness Effect

The distribution of density ratio ($\rho/\rho_\infty$) profiles for three sections along surface S1 in a combined gap/step configuration is displayed in Fig. 5.13, parameterized by the step frontal-face height $h^*$. In this group of plots, for comparison purpose, density ratio profiles for the forward-facing step (S) (LEITE, 2009), for the gap (G) (PAOLICCHI, 2011), and for the flat-plate (FPL) (LEITE; SANTOS, 2011) cases are also presented in the same plots. Again, due to the large range of variation for the ratio $\rho/\rho_\infty$ along surface S1, the scale in the $x$-direction differs from one plot to another.

According to Fig. 5.13, it is observed that the upstream disturbance imposed by the combined gap/step configuration, and by the step for the $h^* = 9.69$ case, is felt by the density profile at section $X = 39$. In contrast, there is no indication that the density profile be affected by the presence of the combined gap/step or by the step with $h^* = 3.23$. As expected, by increasing the step frontal-face $h$, the disturbance caused by the step is felt more upstream in the flow.

Another flow peculiarity is observed in Fig. 5.13. It is noted that density dramatically increases as the flow approaches the step frontal-face, i.e., the density $\rho$ increased at least by an order of magnitude when compared to the freestream density $\rho_\infty$, as illustrated in the profiles for section $X = 48$. For comparison purpose, the density ratio $\rho/\rho_\infty$ for step cases (LEITE, 2009) is around 14.09, 36.75 and 51.94 for $h^*$ of 3.23, 6.46, and 9.69, respectively, for section $X = 48$. On the other hand, the density ratio for the gap/step configuration at the same section is smaller than that for step case alone, around 4.83, 22.37, and 41.87, for $h^*$ of 3.23, 6.46, and 9.69, respectively. The reason for that is because, at the vicinity of the step frontal-face, the flow enters into the gap, decreasing the density at the vicinity of surface S1/S2 junction.

Figure 5.12 - Density ratio ($\rho/\rho_\infty$) profiles for three sections along surface S3 inside the gap in a combined gap/step configuration, defined by section $X'_L$ of -0.25 (top), 0.00 (middle), and 0.25(bottom).
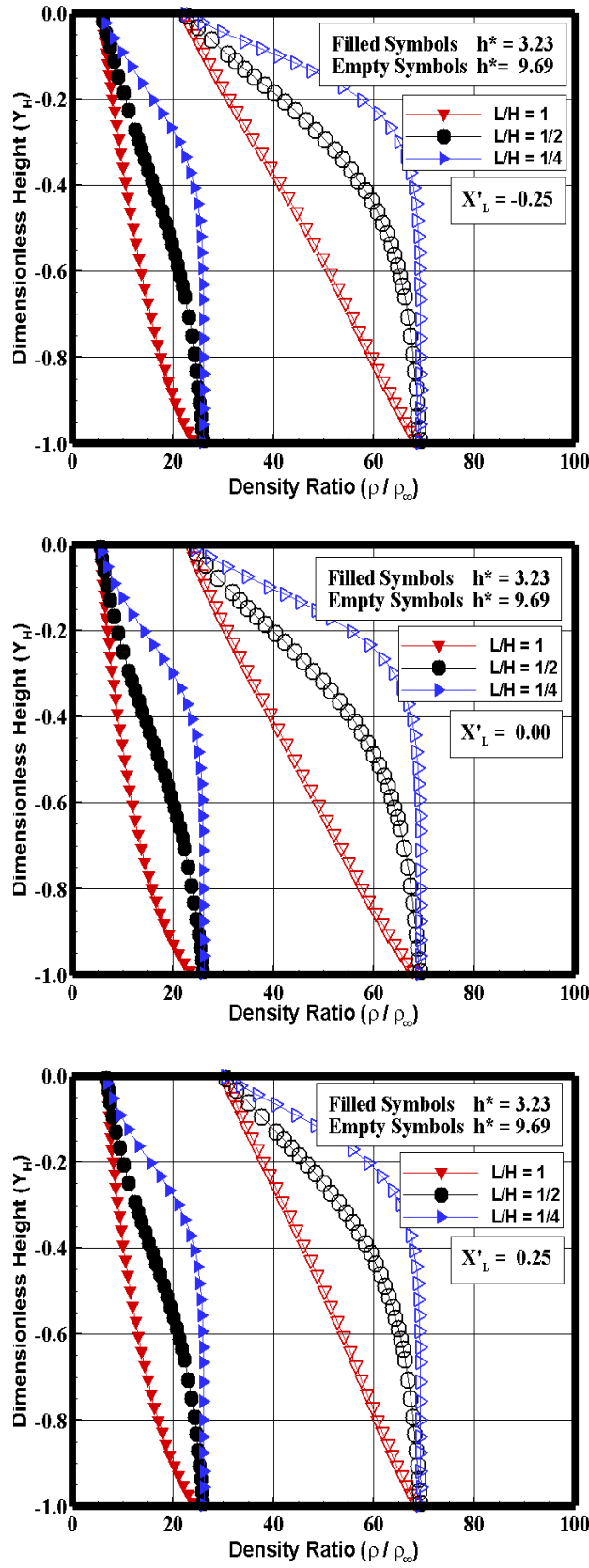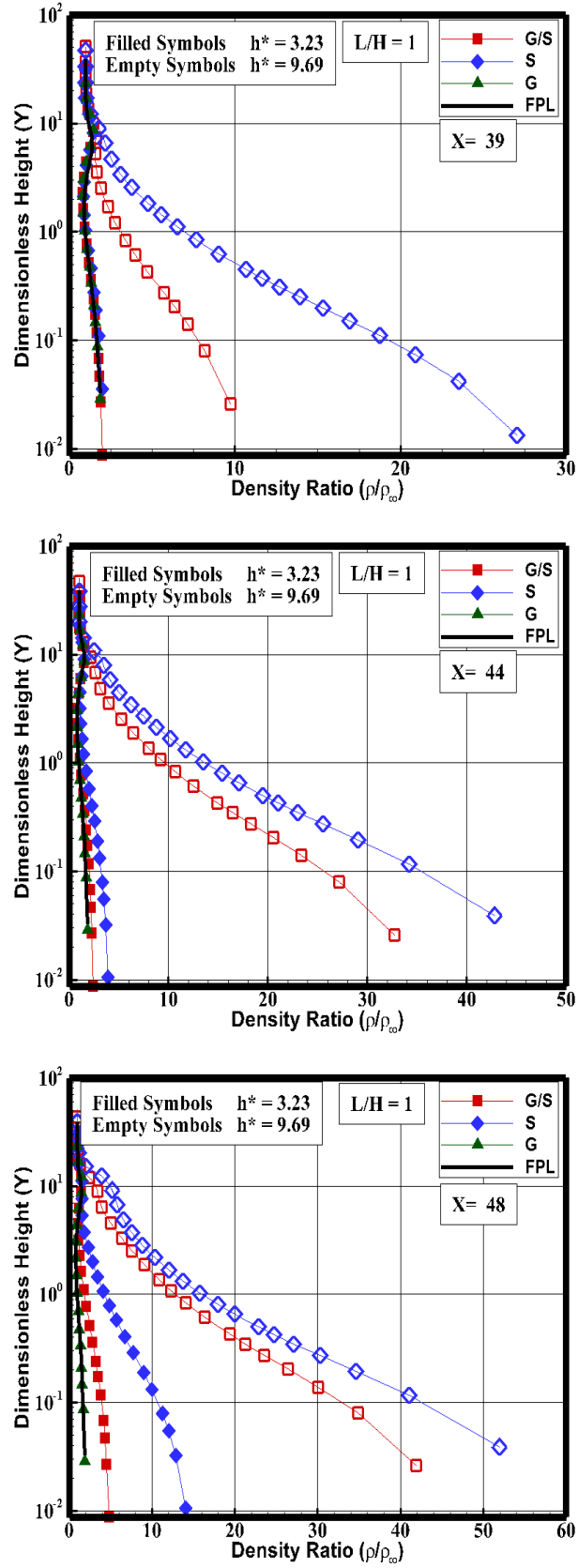
Figure 5.13 - Density ratio ($\rho/\rho_\infty$) profiles for three sections along surface S1 in a combined gap/step configuration, defined by section $X$ of 39 (top), 44 (middle), and 48 (bottom).

It is also seen in Fig. 5.13 that the density ratio experiences significant changes in the perpendicular direction as the flow moves downstream along surface S1. The density ratio is high adjacent to the surface, Y $\approx$ 0, and rapidly decreases inside the boundary layer. This behavior is observed when the body surface is very much cooler than the stagnation temperature of the oncoming gas. As a result, the gas near the body surface is very much cooler than the gas in the rest of the boundary layer. Finally, as Y $\rightarrow \infty$, the density tends to recover the freestream density.

Density ratio ($\rho/\rho_\infty$) profiles for three sections $X'_L$ inside the gap, in a combined gap/step configuration, are illustrated in Fig. 5.14. In this set of plots, plots in the left and right columns correspond to the gap $L/H$ ratio of 1 and 1/4, respectively. In addition, for comparison purpose, density ratio profiles for the gap case (PAOLICCHI, 2011) are also illustrated in the same plots. Based on these plots, it is seen that the density ratio inside the gap dramatically increases from the upper to the bottom of the gaps for the gap $L/H$ ratio and the step height $h$ investigated. It is also noticeable that the density ratio increases inside the gap by increasing the step frontal-face height $h$, and tends to a constant value at the bottom of the gap with decreasing the $L/H$ ratio. The maximum values for density inside the gap with $L/H$ of 1/4 are about 25, 44, and 68 times the freestream density for step frontal-face height $h^*$ of 3.23, 6.46 and 9.69, respectively. As a base of comparison, for the gap case (PAOLICCHI; SANTOS, 2010) with $L/H$ ratio of 1, 1/2, and 1/4, the density inside the gap was around 3 times the freestream density, for the same flow conditions. Consequently, the step frontal-face acts as a barrier in the sense that part of the flow enters into the gap.

Finally, in an attempting to bring out the essential features of the density behavior inside the combined gap/step configuration, Figs. 5.15, 5.16, and 5.17 depict contour maps for the density ratio distribution in the vicinity of the gap/step configuration. It may be recognized from this set of plots that density ratio increases inside the gap by increasing the step frontal-face height $h^*$, for the conditions investigated.
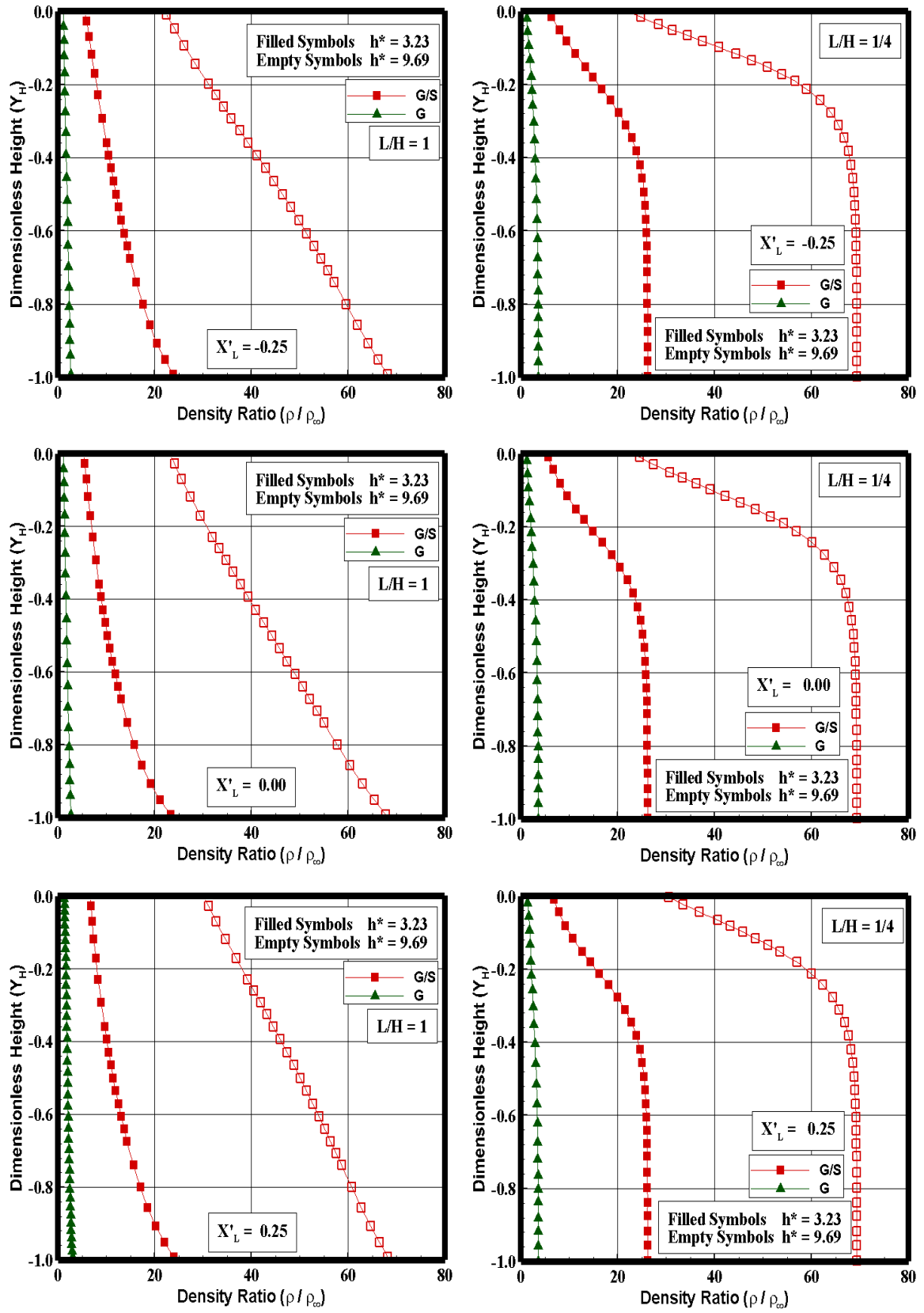
Figure 5.14 - Density ratio ($\rho/\rho_\infty$) profiles inside the gap with $L/H$ of 1 (left column), and 1/4 (right column), for three sections in a combined gap/step configuration, defined by section $X'_L$ of -0.25 (top),0.00 (middle), and 0.25 (bottom).

104
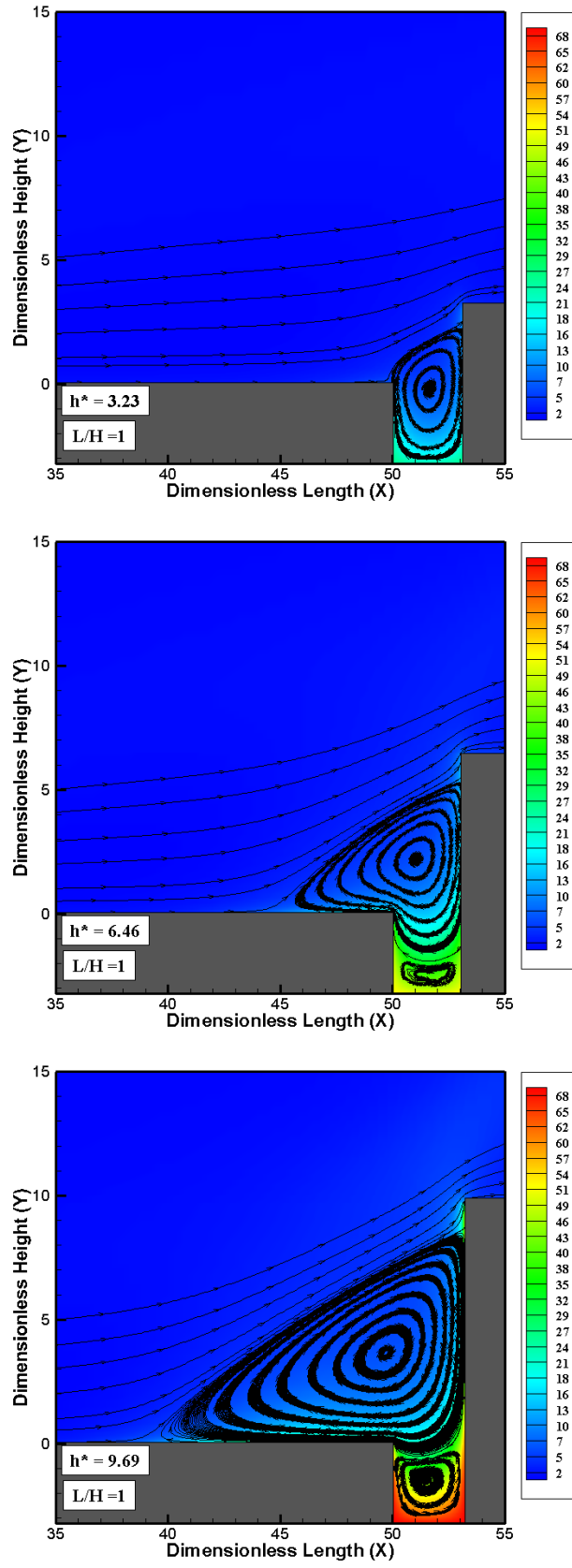
Figure 5.15 - Density ratio ($\rho/\rho_\infty$) contour maps around the combined gap/step configuration, with $L/H$ ratio of 1 and frontal-face thickness $h^*$ of 3.23 (top), 6.46 (middle), and 9.69 (bottom).
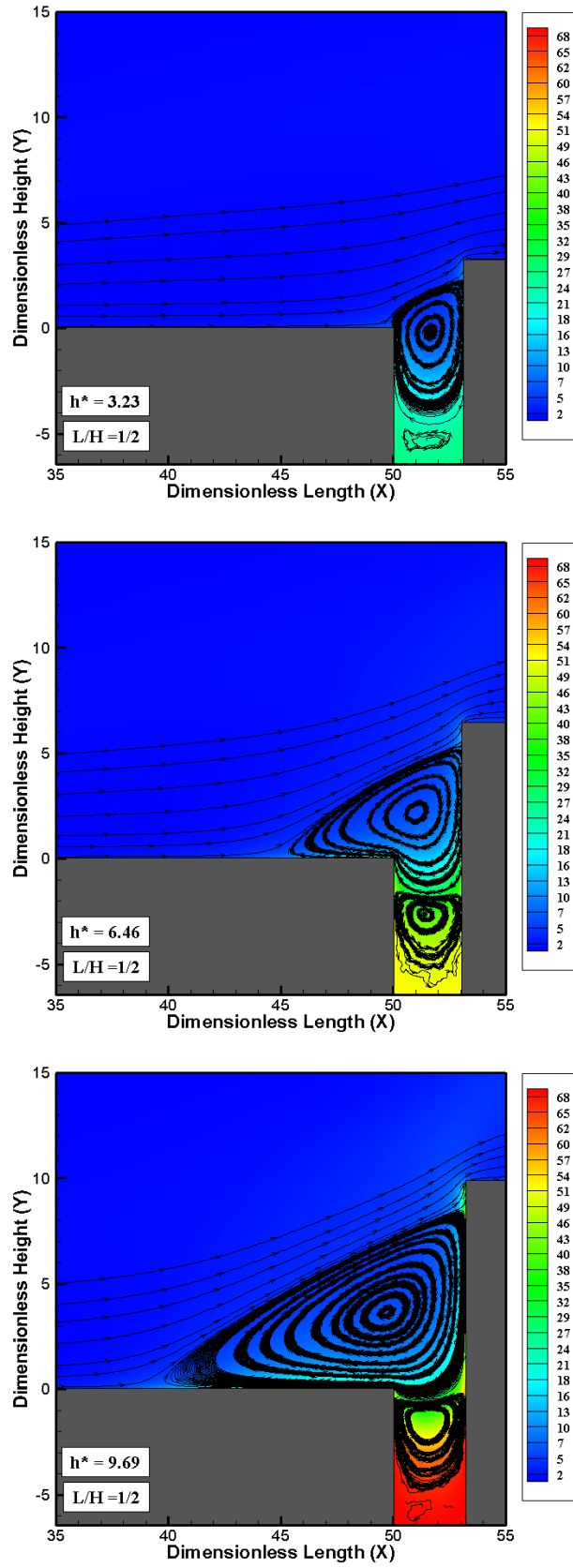
Figure 5.16 - Density ratio ($\rho/\rho_\infty$) contour maps around the combined gap/step configuration, with $L/H$ ratio of 1/2 and frontal-face thickness $h^*$ of 3.23 (top), 6.46 (middle), and 9.69 (bottom).

106
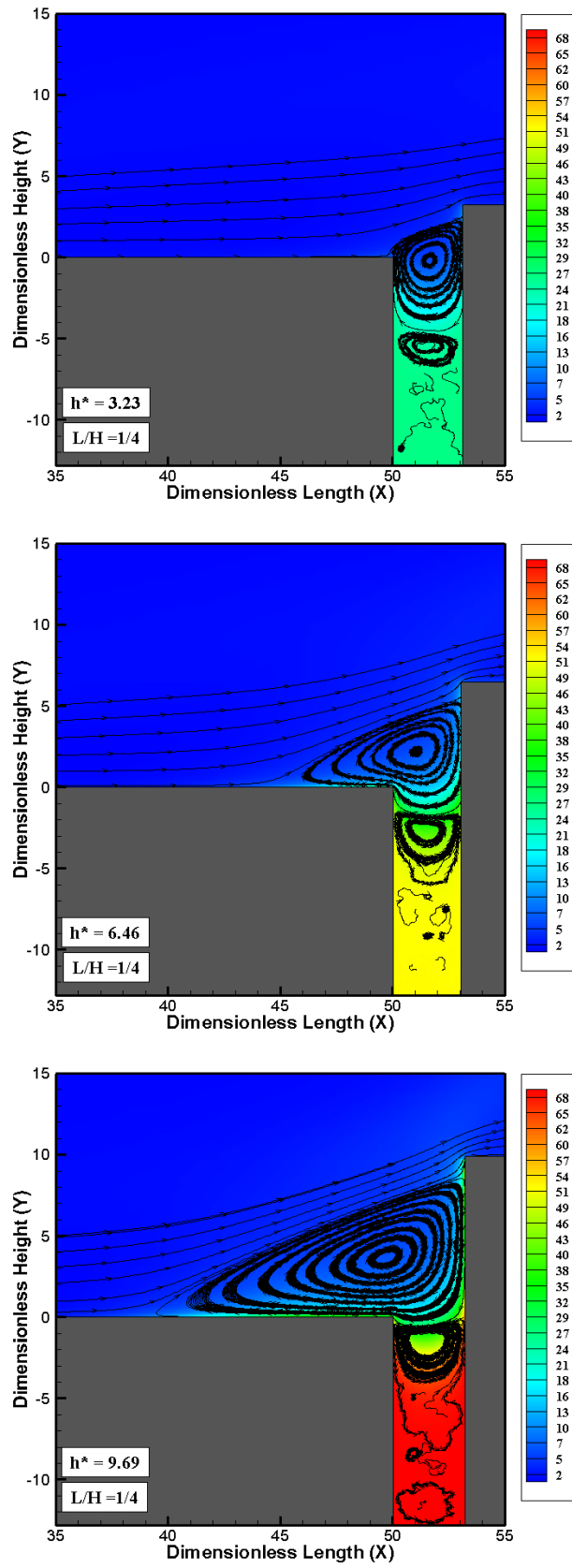
Figure 5.17 - Density ratio ($\rho/\rho_\infty$) contour maps around the combined gap/step configuration, with $L/H$ ratio of 1/4 and frontal-face thickness $h^*$ of 3.23 (top), 6.46 (middle), and 9.69 (bottom).

107

### 5.1.3 Pressure Field

The pressure in each cell inside the computational domain is obtained by the following equation,

$$p = \frac{1}{3V_c} \sum_{j=1}^{N} \frac{(mc'^2)_j}{N} \qquad (5.3)$$

where $N$ is the number of molecules in the cell, $m$ is the molecular mass and $V_c$ is the volume of the cell and $c'$ is the thermal velocity of the molecules.

#### 5.1.3.1 Gap $L/H$ Ratio Effect

Pressure ratio ($p/p_\infty$) profiles for three sections along surface S1 in a combined gap/step configuration are depicted in Fig. 5.18 parameterized by the gap $L/H$ ratio. It is clearly seen from these plots that the gap $L/H$ ratio changes do not affect the pressure ratio ahead the combined gap/step geometry along surface S1. Conversely, the pressure field is affected by the presence of the step. It is found that, at the vicinity of the step frontal-face, the pressure $p$ increased two orders of magnitude as compared to the freestream pressure $p_\infty$. The maximum value for the pressure occurs near to the step corner, at position $X = 48$.

Pressure ratio ($p/p_\infty$) profiles inside the gaps, in a combined gap/step geometry, are demonstrated in Fig. 5.19 for three sections $X'_L$. It is seen from these plots that the gap $L/H$ ratio affects the pressure inside the gap in a combined gap/step configuration, in the sense that the pressure ratio tends to a constant value at the bottom surface of the gaps with decreasing the $L/H$ ratio. In addition, as the step height $h$ changed from 3.23 to 9.69, the pressure dramatically increased inside the gaps.

#### 5.1.3.2 Step Frontal-face Thickness Effect

Pressure ratio ($p/p_\infty$) profiles for three sections along surface S1 in a combined gap/step configuration are illustrated in Fig. 5.20, for step frontal-face height $h^*$ of 3.23 and 9.69. For comparison purpose, pressure ratio profiles for the forward-facing step (LEITE, 2009), the gap (PAOLICCHI, 2011), and the flat-plate (LEITE; SANTOS, 2011) are also exhibited in these plots.

According to these plots, it is noticed that pressure ratio profiles follow a similar behavior as that presented by the density ratio profiles in the sense that, at section $X$

Figure 5.18 - Pressure ratio ($p/p_\infty$) profiles for three sections along surface S1 in a combined gap/step configuration, defined by section $X$ of 39 (top), 44 (middle), and 48 (bottom).

Figure 5.19 - Pressure ratio ($p/p_\infty$) profiles for three sections inside the gap in a combined gap/step configuration, defined by section $X'_L$ of -0.25 (top), 0.00 (middle), and 0.25(bottom).

110
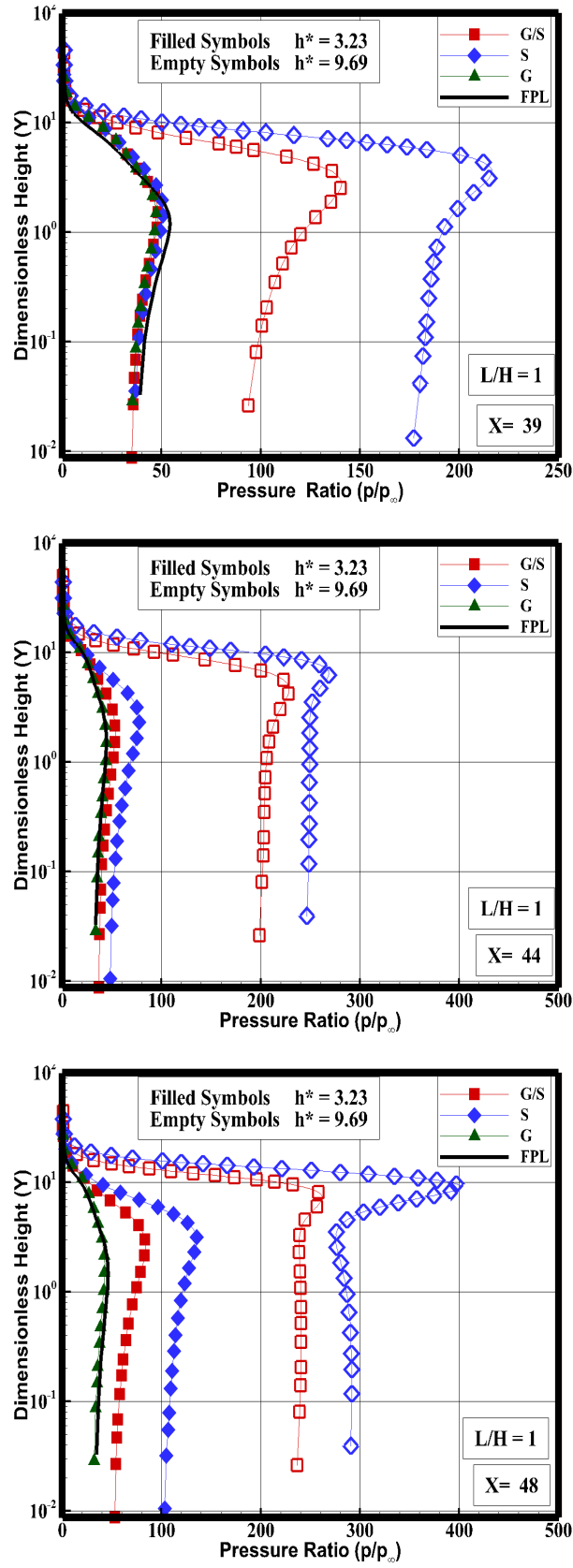
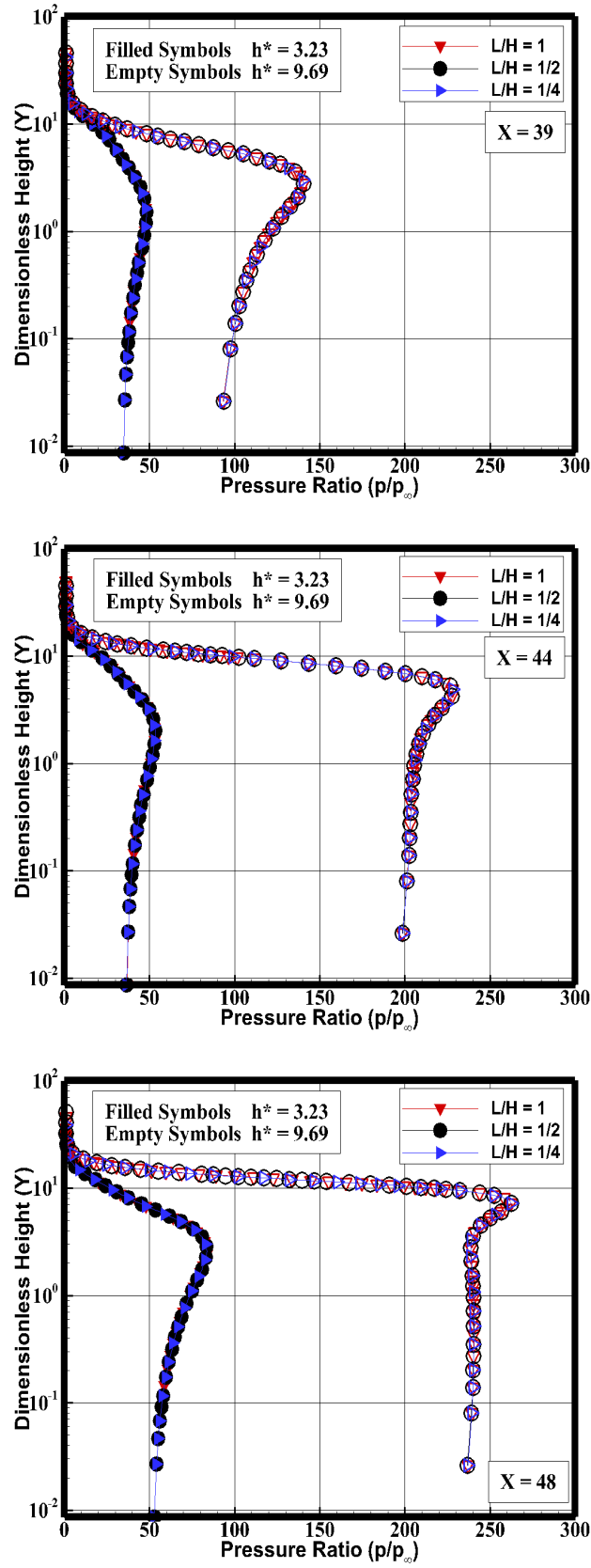Figure 5.20 - Pressure ratio ($p/p_\infty$) profiles for three sections along surface S1 in a combined gap/step configuration, defined by section $X$ of 39 (top), 44 (middle), and 48 (bottom).
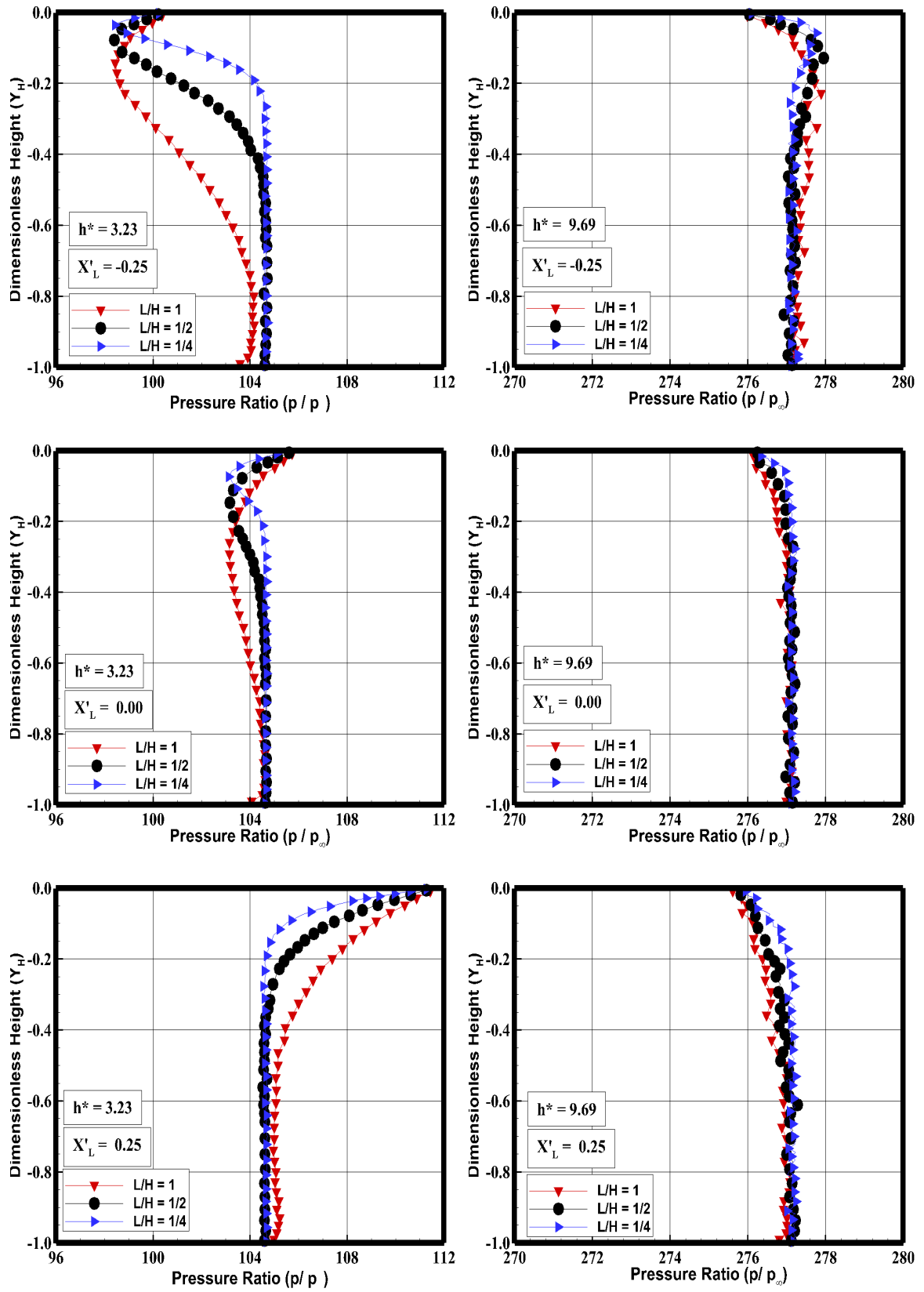
111

= 39, the pressure ratio for the gap, the combined gap/step, and the forward-facing step with $h^* = 3.23$ case is basically identical to that for the flat-plate case. This is an indication that pressure field has not been affected yet by the presence of the gap/step, step, and the gap configuration. However, by increasing the frontal-face thickness $h^*$, from 3.23 to 9.69, the upstream disturbance increases not only for the forward-facing step but also for the gap/step configuration. As the flow approaches the step frontal-face, at section $X = 44$, the pressure profile is already affected by the presence of the forward-facing step with $h^* = 3.23$ case. In contrast, no effect is observed yet in the pressure profile due to the presence of the gap/step configuration with $h^* = 3.23$ case. It may be inferred that the presence of the gap in a combined gap/step configuration attenuates the upstream disturbances. In the following, at section $X = 48$, pressure profiles for the step cases and for the gap/step cases differ considerable from that for the flat-plate case. It is also noticed that the pressure ratio dramatically increases as the flow approaches the step frontal-face. It is seen that the pressure $p$ increased two orders of magnitude as compared to the freestream pressure $p_\infty$. As an illustrative example, for the forward-facing step, at the step base, the pressure ratio $p/p_\infty$ is 142, 230, and 293 for dimensionless step height $h^*$ of 3.23, 6.46, and 9.69, respectively. Consequently, particular attention should be paid to the step base in terms of pressure loads, since the vicinity of the step base represents a zone of strong compression. In a combined gap/step configuration due the presence of a gap, the molecules that were before confined in the recirculation region in front of the step, drops inside the gap, increasing the pressure loads inside the gap as seen in Fig. 5.19.

Effects of the step frontal-face height $h$ changes on pressure ratio $p/p_\infty$ profiles inside the gaps in a combined gap/step configuration are demonstrated in Fig. 5.21 as a function of the dimensionless height $Y_H$, for three sections defined by $X'_L$ of -0.25, 0, and 0.25. In this group of plots, similar to the density ratio profiles, the left-column plots correspond to $p/p_\infty$ for $L/H$ ratio of 1, and the right-column plots correspond to $p/p_\infty$ for $L/H$ ratio of 1/4. According to these plots, it is observed that the pressure ratio inside the gap in a combined gap/step is about one order of magnitude greater than the values reached in the gap case alone. As a base of comparison, the gap case (PAOLICCHI, 2011) presented values of $p/p_\infty \approx 13$ near to the bottom surface of the gap with $L/H$ ratio of 1 and 1/4. For the gap in a combined gap/step case, the pressure ratio $p/p_\infty$ is about 110 and 280 for the step frontal-face dimensionless height $h^* = 3.23$ and 9.69, respectively.
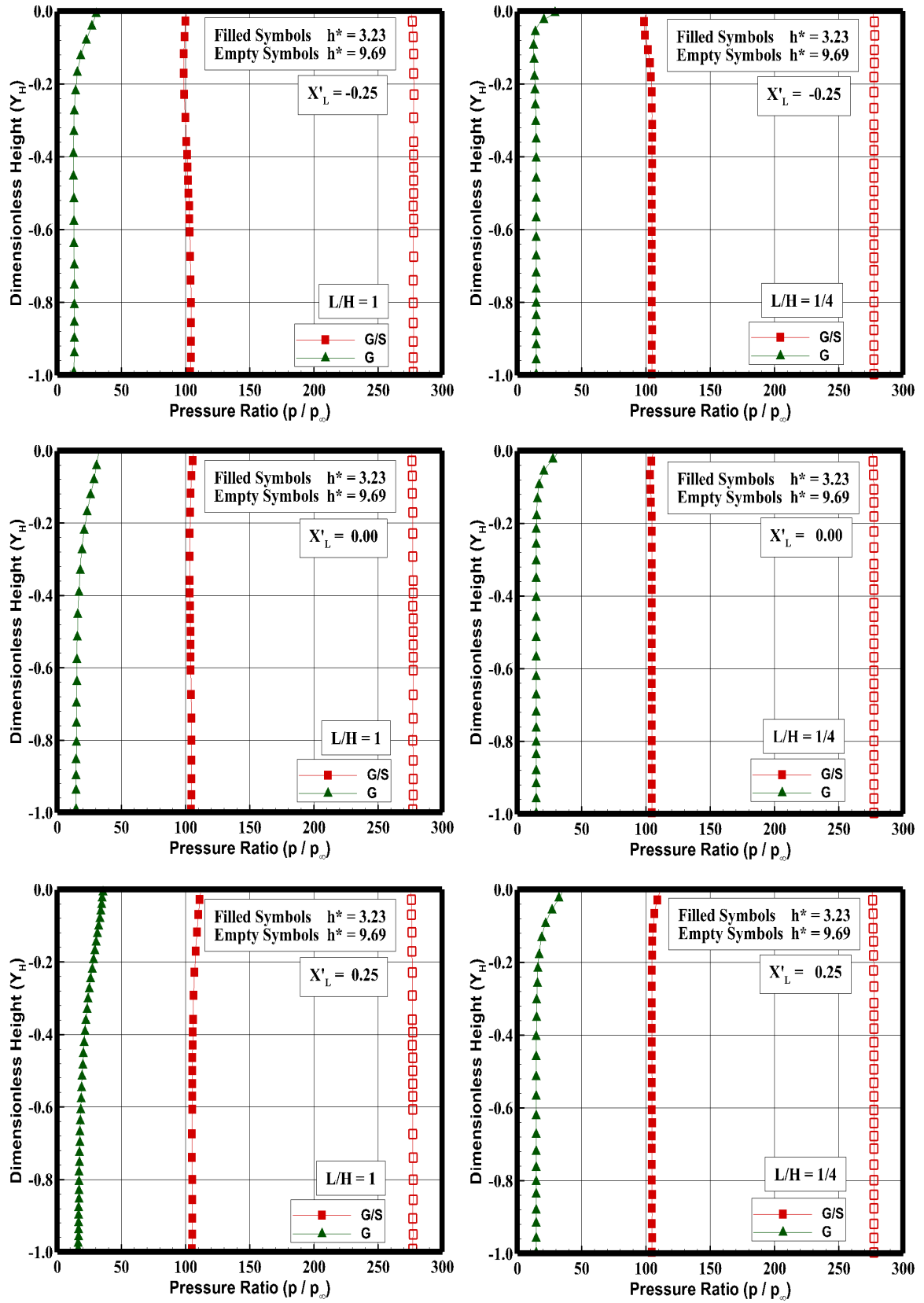
Figure 5.21 - Pressure ratio ($p/p_\infty$) profiles inside the gap with $L/H$ ratio of 1(left column), and 1/4 (right column), for three sections inside the gap in a combined gap/step configuration, defined by section $X'_L$ of -0.25 (top), 0.00 (middle), and 0.25 (bottom).

113

In a effort to highlight points of interest, pressure ratio contour maps around the gap/step configuration are demonstrated in Figs 5.22, 5.23, and 5.24, for gap $L/H$ ratio of 1, 1/2 and 1/4, respectively. On examining these figures, two interesting features are noticed. One of them is related to the peak value for pressure ratio close to the shoulder at the step frontal-face. It is clearly seen that this peak value increases by increasing the step frontal-face height $h$. Indeed the reason for that is because the location of these peak values is related to the flow reattachment point on the step frontal-face surface (see Tab.5.1). The other one is the pressure rise inside the gap due to the presence of the step. For instance, in the combined gap/step case with the gap $L/H$ ratio of 1/4, Figs. 5.21 and 5.24, the pressure ratio is about 110, 208 and 280 at the bottom of the gap, for step height $h^*$ of 3.23, 6.46 (not shown) and 9.69, respectively. In contrast, to the gap case alone (PAOLICCHI, 2011), the pressure ratio for $L/H = 1/4$ case basically changes from 29 (at the top) to 12 (at the bottom). In this fashion, it is firmly established that the combination of a step with a gap increases the pressure ratio inside the gap around one order of magnitude, when compared to that for the gap case alone.
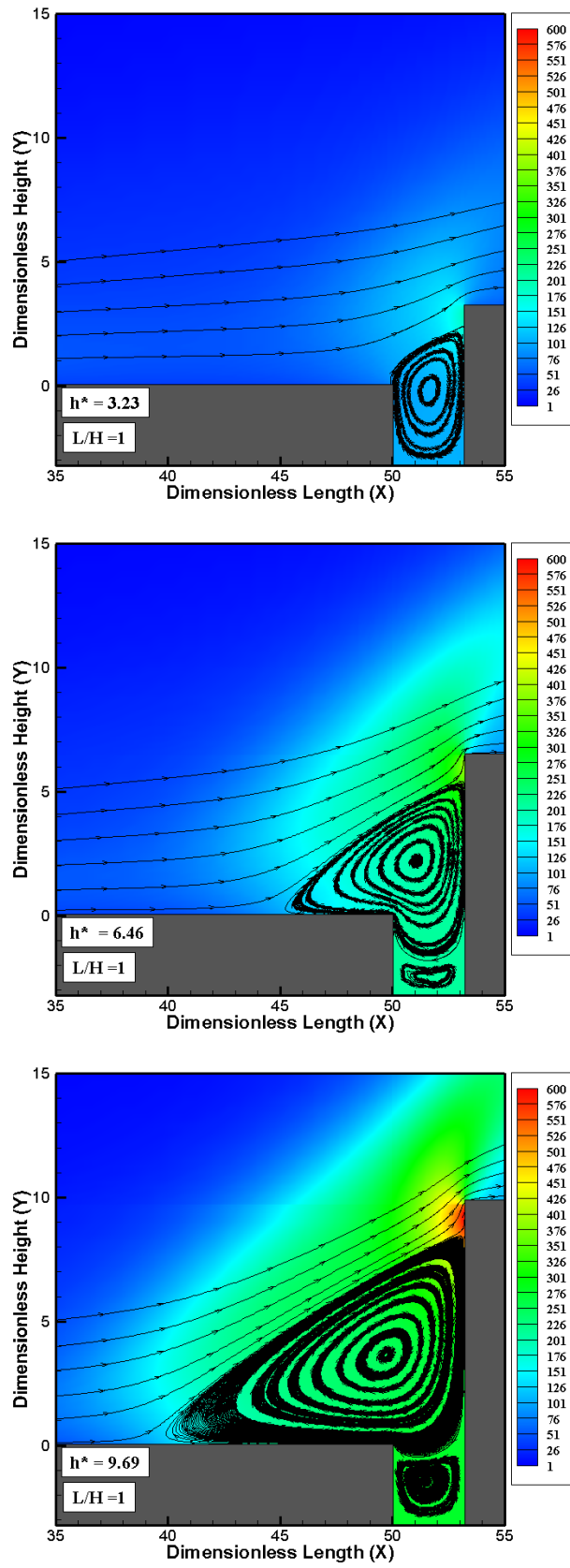
Figure 5.22 - Pressure ratio ($p/p_\infty$) contour maps around the combined gap/step geometry with $L/H$ ratio of 1 and frontal-face thickness $h^*$ of 3.23 (top), 6.46 (middle), and 9.69 (bottom).
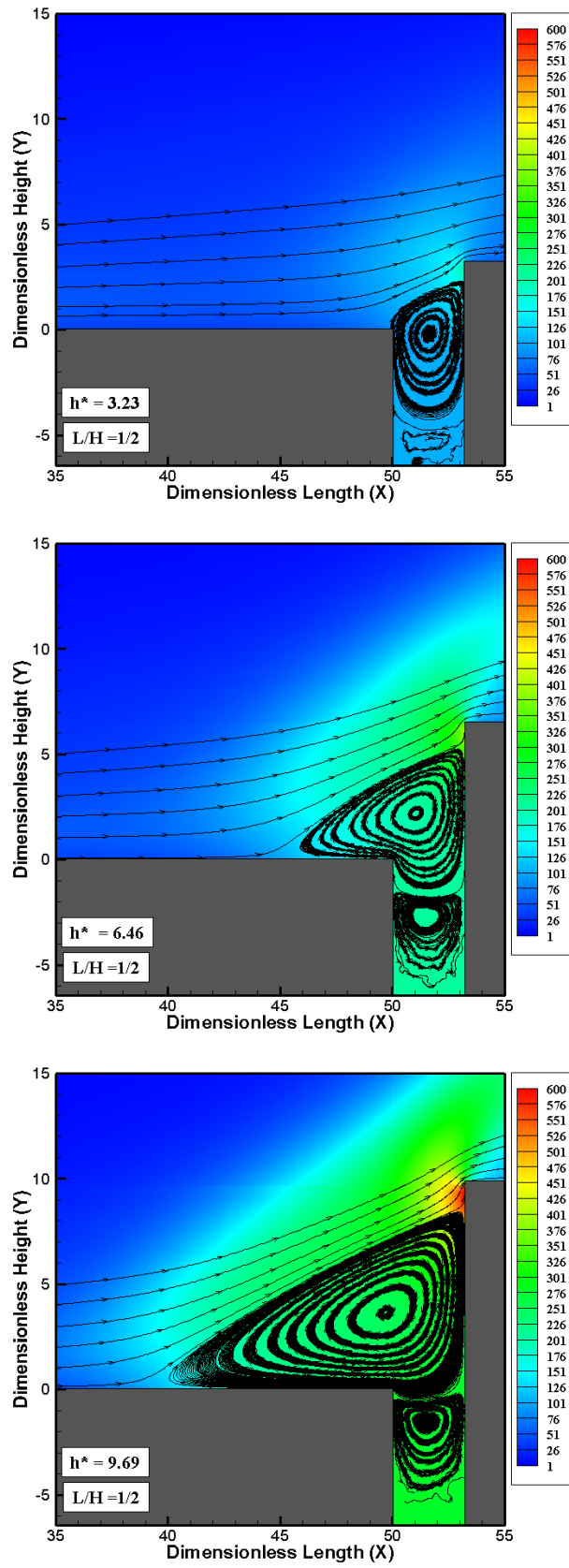
Figure 5.23 - Pressure ratio ($p/p_\infty$) contour maps around the combined gap/step geometry with $L/H$ ratio of 1/2 and frontal-face thickness $h^*$ of 3.23 (top), 6.46 (middle), and 9.69 (bottom).

116
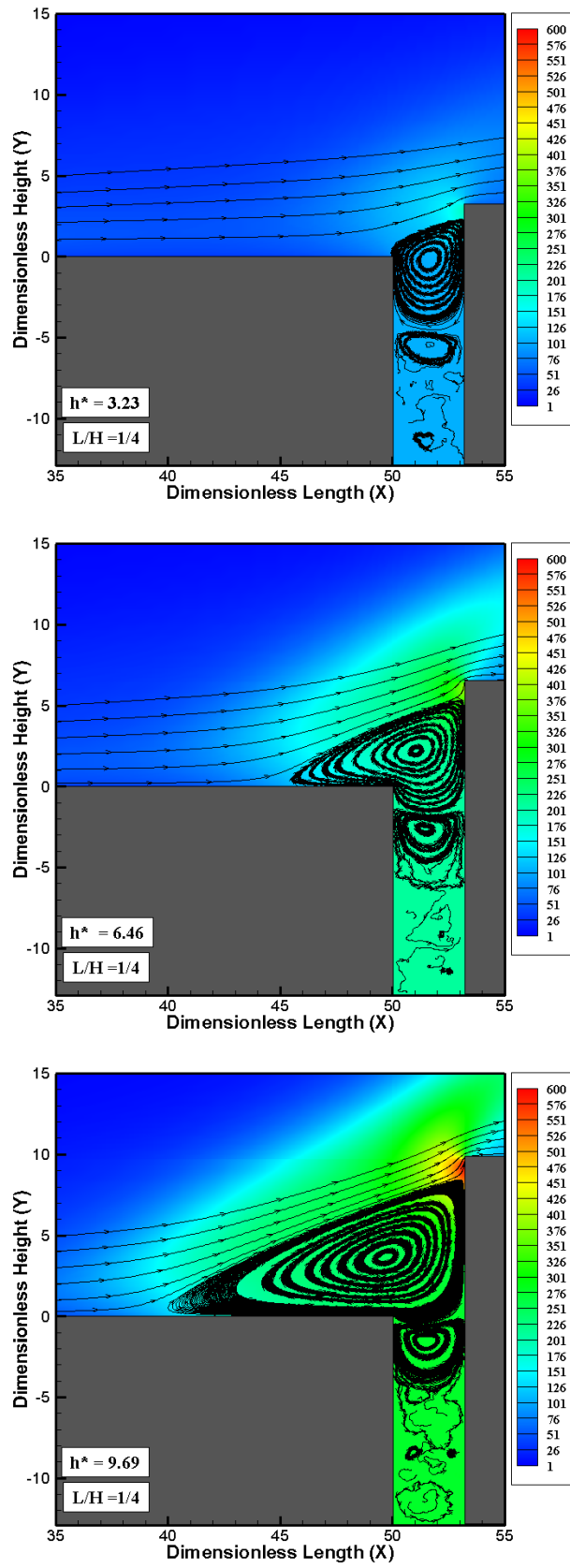
Figure 5.24 - Pressure ratio ($p/p_\infty$) contour maps around the combined gap/step geometry with $L/H$ ratio of 1/4 and frontal-face thickness $h^*$ of 3.23 (top), 6.46 (middle), and 9.69 (bottom).

### 5.1.4 Kinetic Temperature Field

In a diatomic or polyatomic gas in complete thermodynamic equilibrium, the translational temperature is equal to the temperature related to the internal modes, i.e., rotational, vibrational, or electronic temperatures, and it is identified as thermodynamic temperature. When the equilibrium is disturbed, relaxation processes arise in the system that attempt to return it to the state of the total statistical equilibrium.

In a thermodynamic non-equilibrium gas, an overall kinetic temperature is defined as the weighted mean of the translational and internal temperatures (BIRD, 1994) as follows,

$$T_o = \frac{\zeta_t T_t + \zeta_r T_r + \zeta_v T_v}{\zeta_t + \zeta_r + \zeta_v} \tag{5.4}$$

were $\zeta$ is the molecular degree of freedom and subscript $t$, $r$ and $v$ stand for translation, rotation and vibration, respectively.

Translational, rotational, and vibrational temperatures are obtained to each cell in the computational domain by the following equations,

$$T_t = \frac{1}{3k} \sum_{j=1}^{N} \frac{(mc'^2)_j}{N} \tag{5.5}$$

$$T_r = \frac{2}{k} \frac{\bar{\varepsilon}_r}{\zeta_r} \tag{5.6}$$

$$T_v = \frac{\Theta_V}{ln(1 + \frac{k\Theta_v}{\bar{\varepsilon}_v})} \tag{5.7}$$

where $k$ is the Boltzmann constant, $\Theta_v$ is the characteristic temperature of vibration, and $\bar{\varepsilon}_r$ and $\bar{\varepsilon}_v$ are, respectively, rotation and vibration average energies in each cell.

#### 5.1.4.1 Gap $L/H$ Ratio Effect

Overall temperature ratio $(T_o/T_\infty)$ profiles, for three sections along surface S1, are displayed in Fig. 5.25, parameterized by the gap $L/H$ ratio. According to this set of plots, changes on the gap $L/H$ ratio did not affect overall temperature profiles upstream the gap, for the $L/H$ ratio investigated. In contrast, changes on the step frontal-face height $h$ affected the overall temperature upstream the gap. Nevertheless, this effect will be discussed in the subsequent subsection.
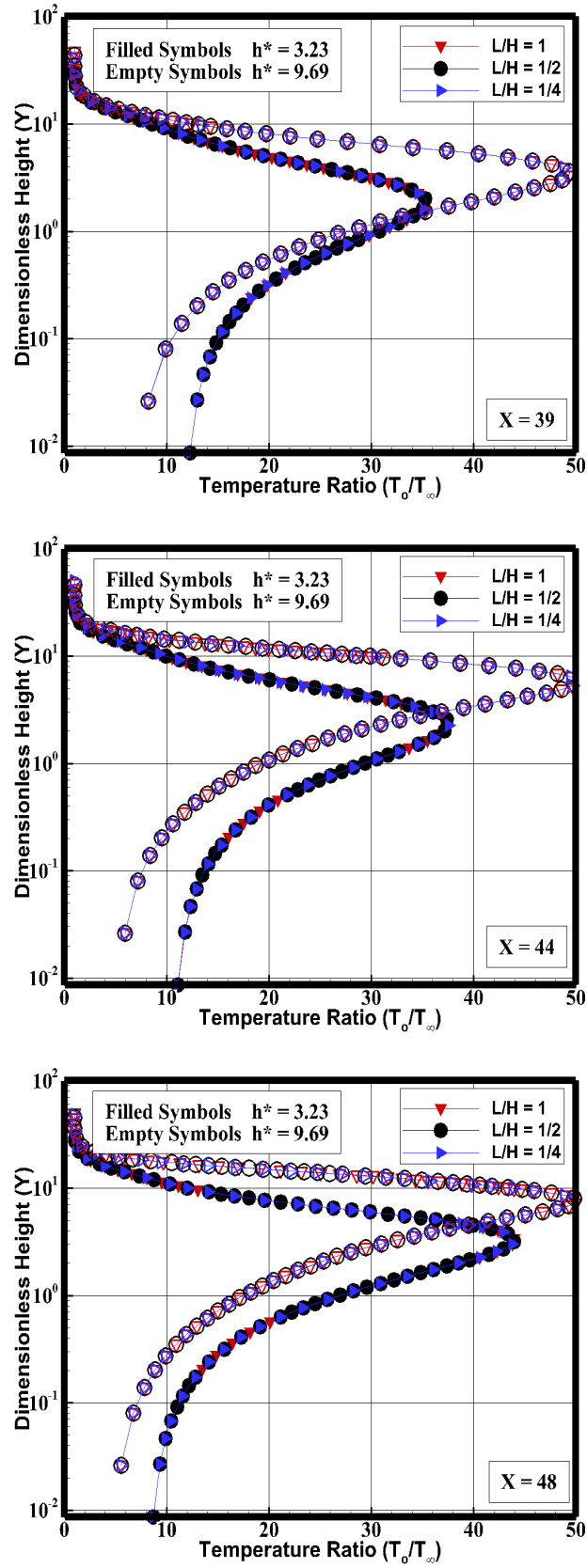
Figure 5.25 - Overall temperature ratio ($T_o/T_\infty$) profiles for three sections along surface S1 in a combined gap/step configuration, defined by section $X$ of 39 (top), 44 (middle), and 48 (bottom).

Overall temperature ratio $(T_o/T_\infty)$ profiles inside the gaps in a combined gap/step geometry are demonstrated in Fig. 5.26, for three sections $X'_L$, parameterized by the gap $L/H$ ratio. It is seen from these plots that the gap $L/H$ ratio and the step frontal-face height $h$ affect the overall temperature ratio profiles inside the gap. As the gap $L/H$ ratio decreases, the overall temperature inside the gap tends to a constant value at the bottom surface. The overall temperature is high at the top of the gap, section $Y_H = 0$, and decreases inside the gap up to reach the wall temperature $(T_w \approx 4T_\infty)$ at the gap bottom surface, $Y_H = $ -1. In addition, the overall temperature for $h^*$ = 3.23, at section $Y_H = 0$, is greater than that observed for $h^* = 9.69$ case. As a matter of fact, the density at the vicinity of the step base for the $h^* = 9.69$ case is greater than the values observed for the $h^* = 3.23$ case, as seen in Fig. 5.14. In this sense, in the vicinity of the step base in a gap/step configuration with $h^* = 9.69$, the flow tends to achieve the thermodynamic equilibrium. Since a large number of collisions is needed to excite the vibrational modes of the molecules, the vibrational temperature is seen to increase much more slowly than other temperature modes. In this scenario, the overall temperature tends the same value of the vibrational temperature, since the flow is tending to the thermodynamic equilibrium in this region.

### 5.1.4.2 Step Frontal-face Thickness Effect

In order to have a clear qualitative picture of the temperature field, it is instructive to examine separately translational, rotational, and vibrational kinetic temperature profiles instead of the overall kinetic temperature $T_o$, as defined by Eq. 5.4. In this fashion, step height effects on translational, rotational, and vibrational kinetic temperatures are illustrated in Figs. 5.27, 5.28, and 5.29, respectively, for three sections along surface S1. In this group of plots, temperature ratio stands for translation temperature $T_t$, rotational temperature $T_r$, and vibrational temperature $T_v$, normalized by the freestream temperature $T_\infty$. Again, for comparison purpose, temperature profiles for the forward-facing step (S) (LEITE; SANTOS, 2011), for the gap (G) (PAOLICCHI, 2011), and for the flat-plate case (FPL) (LEITE; SANTOS, 2011), are also illustrated in the same set of plots.

On examining this set of plots, it is quite apparent that thermodynamic non-equilibrium occurs throughout the shock layer, as shown by the lack of equilibrium of the translational and internal kinetic temperatures. In addition, it is clearly noted that, in the undisturbed freestream far from surface S1, $Y \to \infty$, the translational and internal kinetic temperatures have the same value and are equal to the thermo-
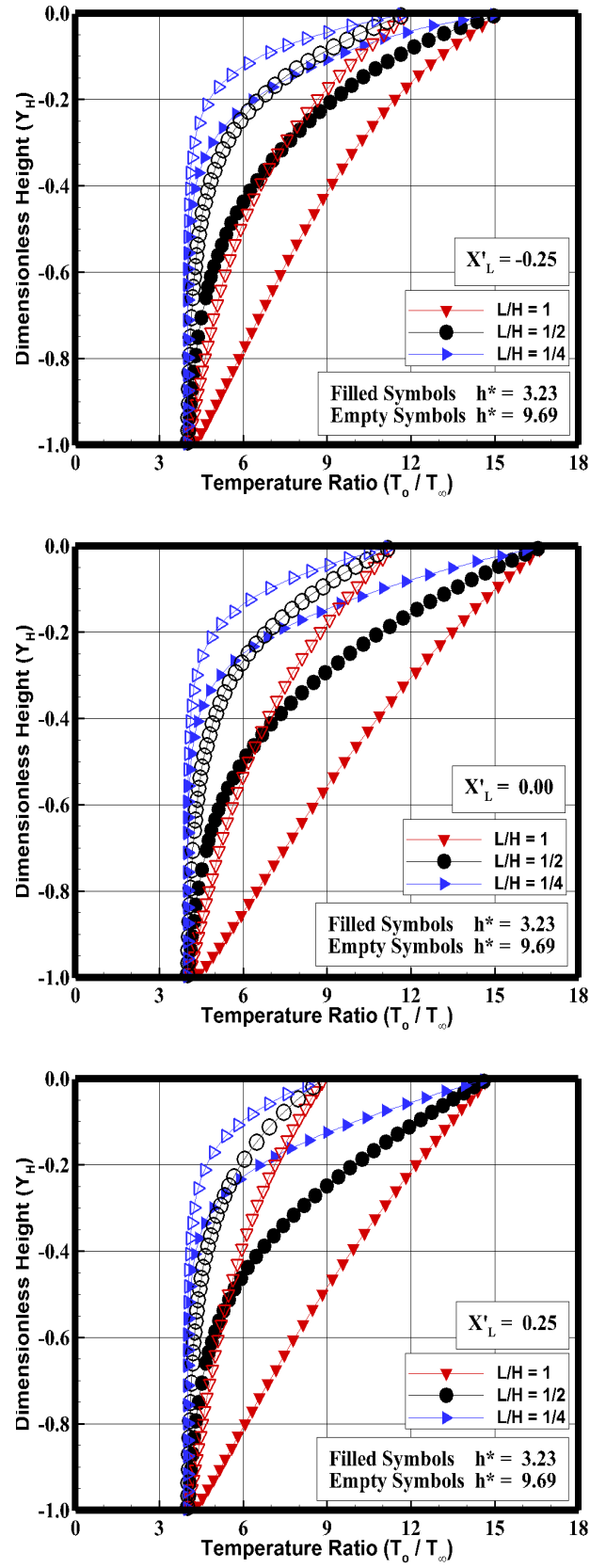
Figure 5.26 - Overall temperature ratio ($T_o/T_\infty$) profiles for three sections inside the gap in a combined gap/step configuration, defined by section $X'_L$ of -0.25 (top), 44 (middle), and 48 (bottom).

121

Figure 5.27 - Translational temperature ratio $(T_t/T_\infty)$ profiles for three sections along surface S1 in a combined gap/step configuration, defined by section $X$ of 39 (top), 44 (middle), and 48 (bottom).

Figure 5.28 - Rotational temperature ratio $(T_r/T_\infty)$ profiles for three sections along surface S1 in a combined gap/step configuration, defined by section $X$ of 39 (top), 44 (middle), and 48 (bottom).
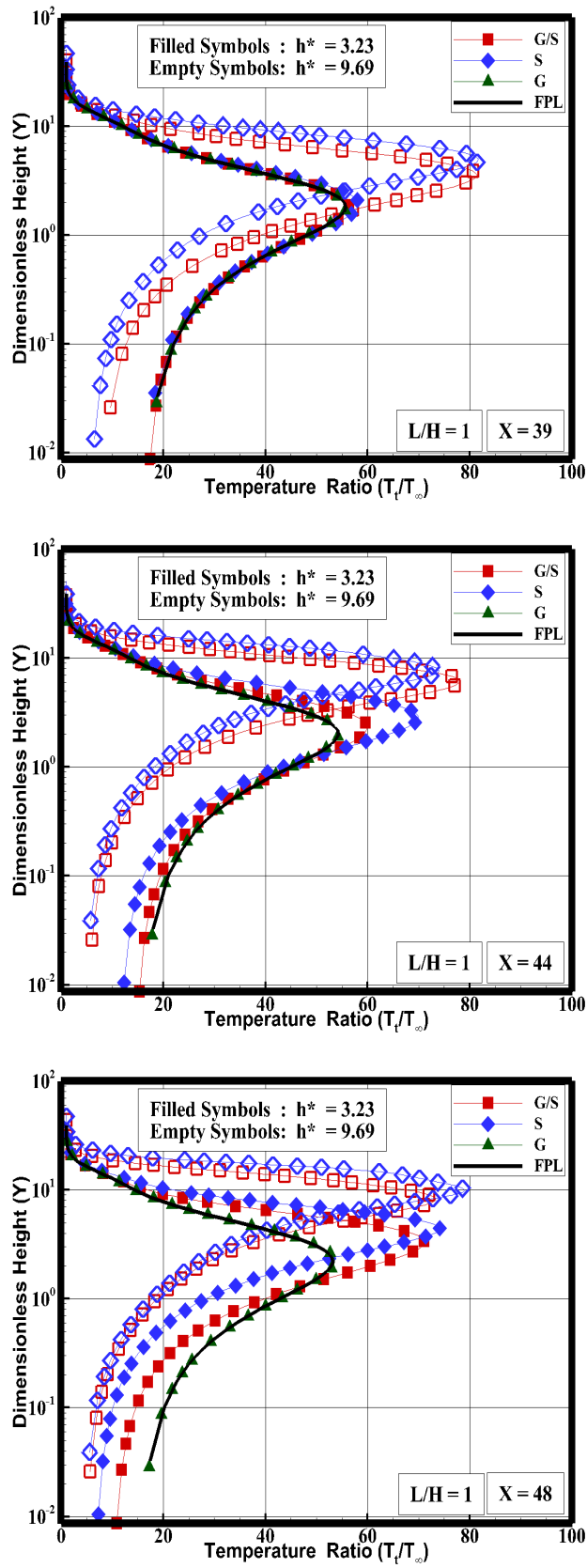
123

Figure 5.29 - Vibrational temperature ratio $(T_v/T_\infty)$ profiles for three sections along surface S1 in a combined gap/step configuration, defined by section $X$ of 39 (top), 44 (middle), and 48 (bottom).
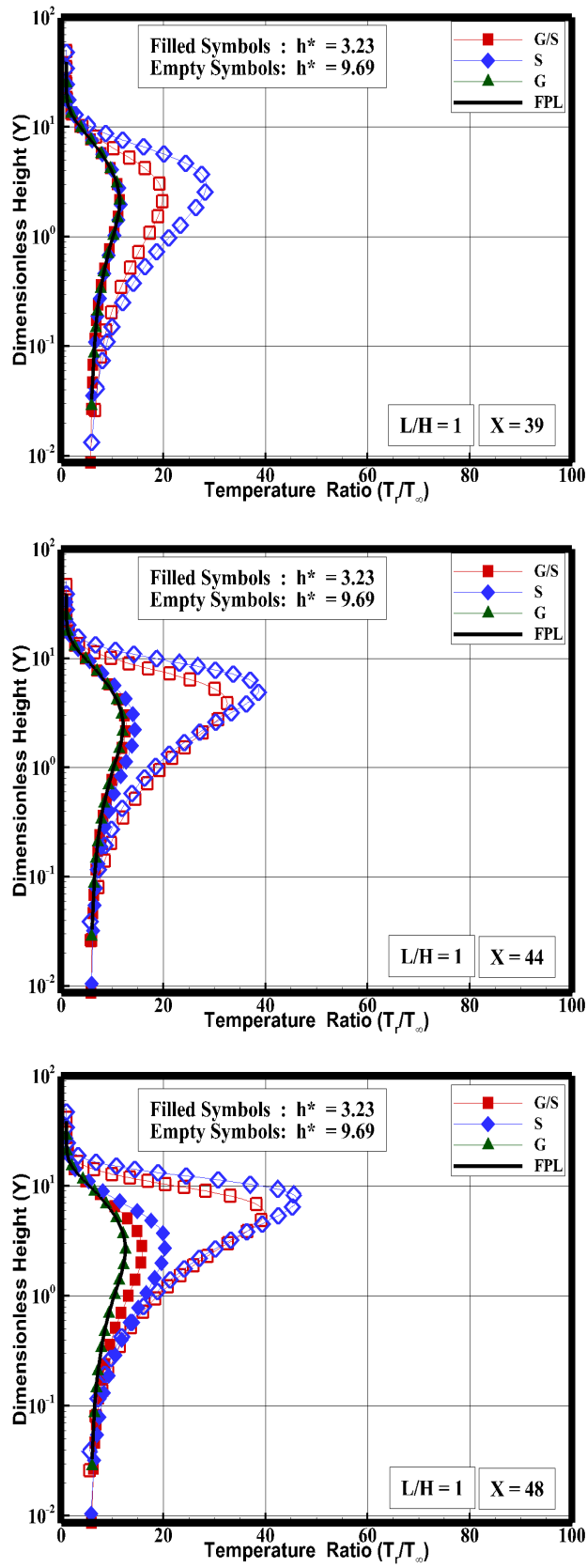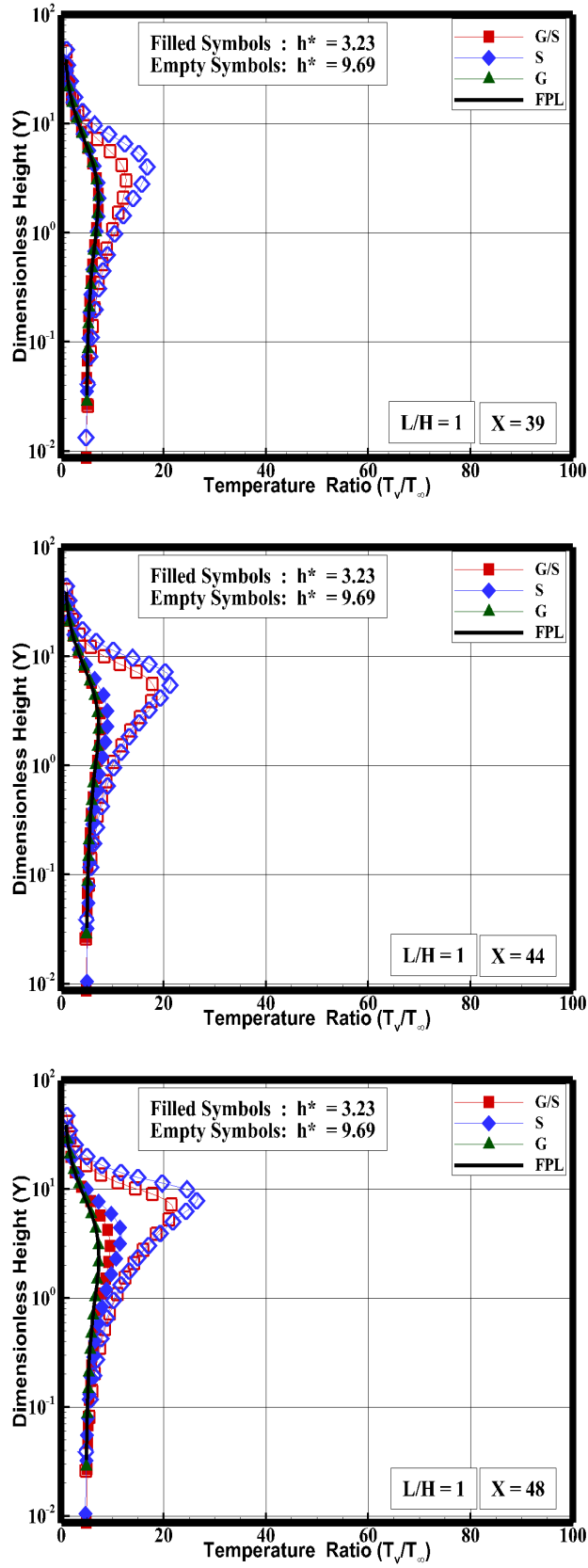
124

dynamic temperature. Approaching to the lower surface (Surface S1), in the range, $2 < Y < 10$, the translational kinetic temperature rises to well above the rotational and vibrational temperatures, and reaches a maximum value that relies on the geometry, i.e., gap/step configuration, forward-facing step, gap, or flat plate. In addition, this maximum value depends on section $X$. Since a large number of collisions is needed to excite vibrational modes of the molecules, from the ground state to the upper state, the vibrational temperature is seen to increase much more slowly than rotational temperature. Still further toward the lower surface S1, $Y \approx 0$, the translational, rotational, and vibrational temperatures decrease, and reach values that depend on the section $X$. For section $X = 39$, kinetic temperatures reach values on the wall that are above the wall temperature $T_w(\approx 4T_\infty)$, resulting in a temperature jump as defined in a continuum formulation. For section X = 44, the difference between translational temperature and internal temperatures for the $h^* = 9.69$ case indicates that the thermodynamic equilibrium is achieved close to surface S1. Finally, for section $X = 48$, the kinetic temperatures basically reach the wall temperature $T_w$, and the thermodynamic equilibrium is achieved for the $h^*$ of 9.69 case.

Proceeding in a manner analogous to the earlier primary properties, effects of the step height $h$ and the $L/H$ ratio on kinetic temperature ratio profiles inside the gaps in a combined gap/step configuration are demonstrated in Fig. 5.30, for three sections defined by $X'_L$ of -0.25, 0, and 0.25. In this set of plots, solid lines represents the gap alone, investigated by Paolicchi (PAOLICCHI, 2011). Also, the left column plots correspond to the gap $L/H$ ratio of 1, and the right column plots the gap $L/H$ of 1/4. According to these plots, it is quite apparent that the kinetic temperature ratio (translation, rotation, and vibration) decreases and reaches a constant value along the bottom surface, which corresponds to the wall temperature $T_w$ ($\approx 4T_\infty$). Particularly to the gap/step case with $L/H$ ratio of 1/4, at the bottom surface, it is seen that the flow is in thermal equilibrium, since the internal temperatures are equal to the translational temperature. It is important to recall that the density dramatically increased at the vicinity of the gap bottom surface, as shown earlier in Fig. 5.14. Consequently, the local mean free path decreased and the mean collision frequency increased and, therefore, the flow reaches the thermal equilibrium.

In what follows, it proves convenient to present contour maps for temperature at the vicinity of the gap/step configuration. In doing so, Figs. 5.31, 5.32, and 5.33 demonstrate the overall temperature ratio, $T_o/T_\infty$, for step frontal-face height $h^*$ of 3.23, 6.46, and 9.69. Of particular interest in this set of plots is the impact of the
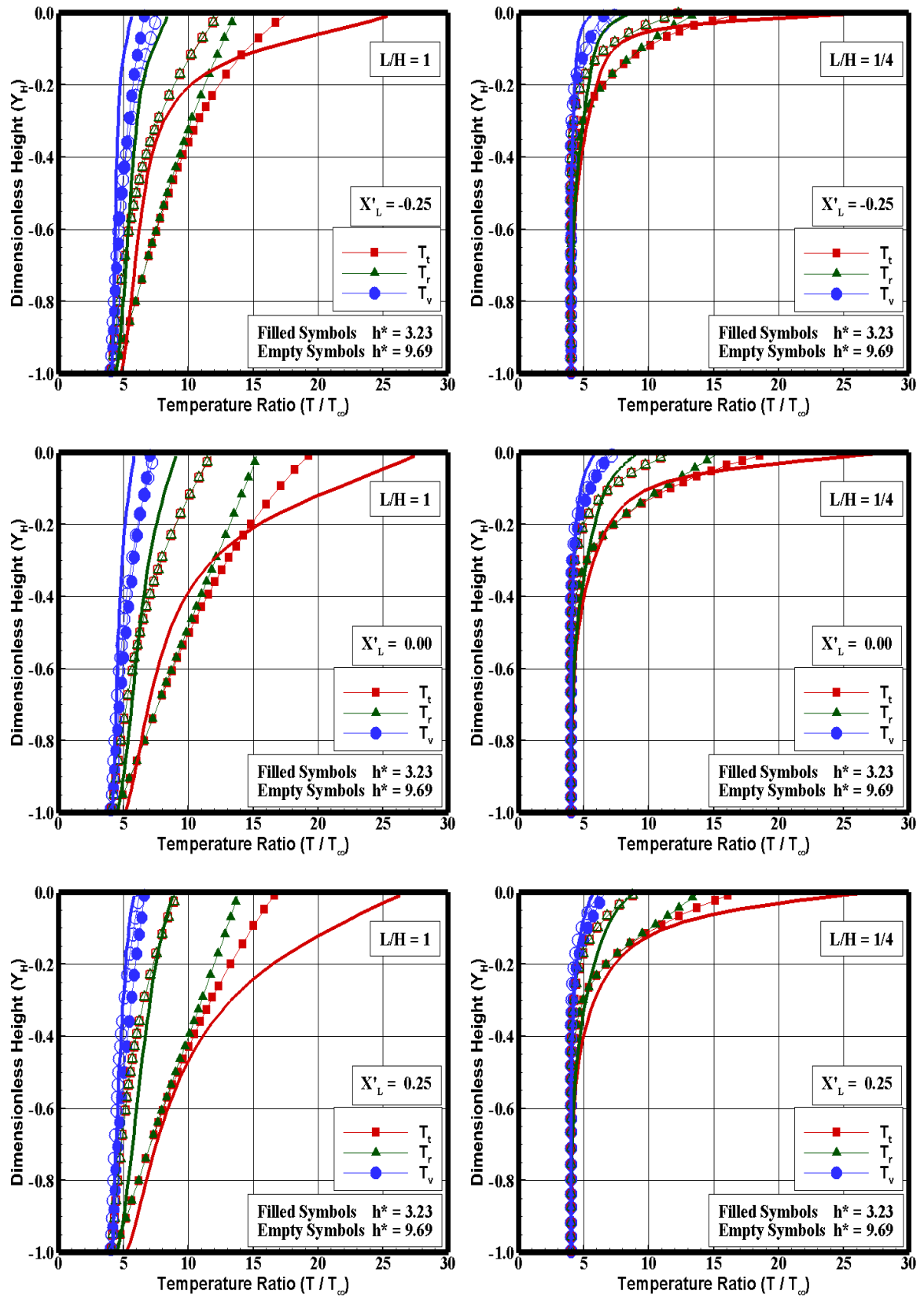
Figure 5.30 - Temperature ratio ($T/T_\infty$) inside the gap with $L/H$ of 1 (left column), and 1/4 (right column), for three sections inside the gap in a gap/step configuration, defined by section $X'_L$ of -0.25 (top), 0.00 (middle), and 0.25 (bottom).
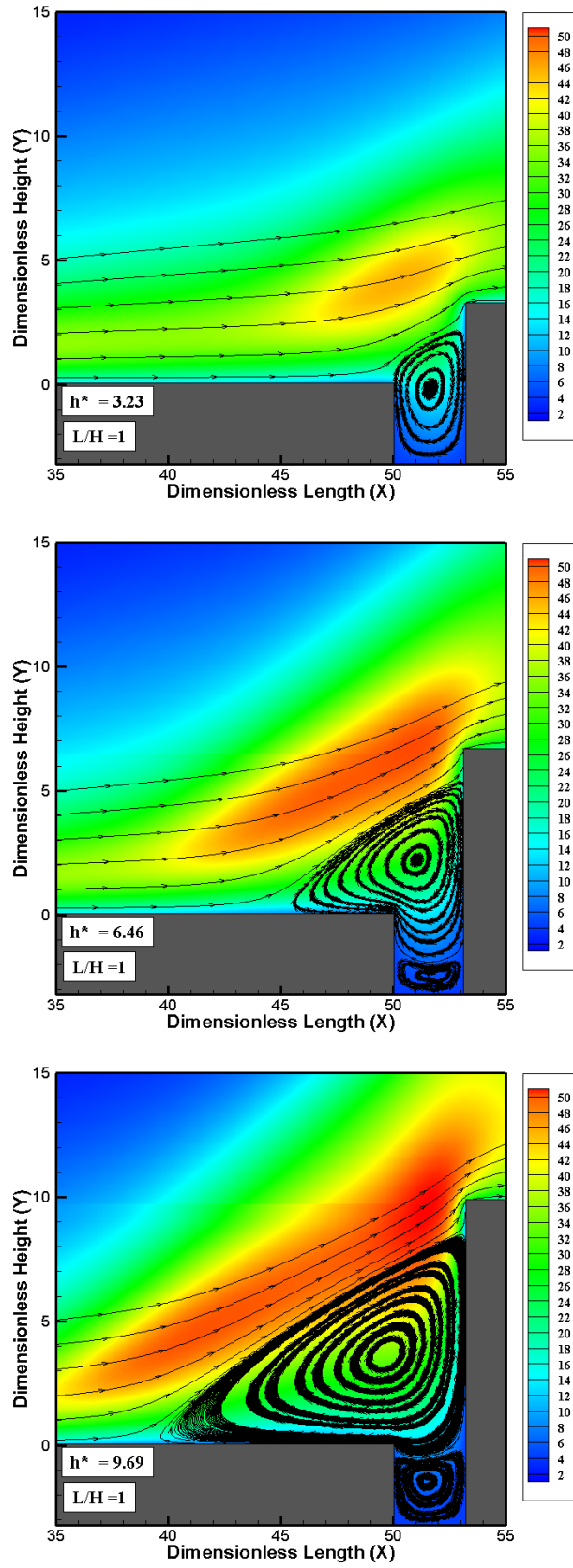
Figure 5.31 - Overall temperature ratio $(T_o/T_\infty)$ contour maps around the combined gap/step geometry with $L/H$ ratio of 1 and frontal-face thickness of $h^* = 3.23$ (top), 6.46 (middle), and 9.69 (bottom).
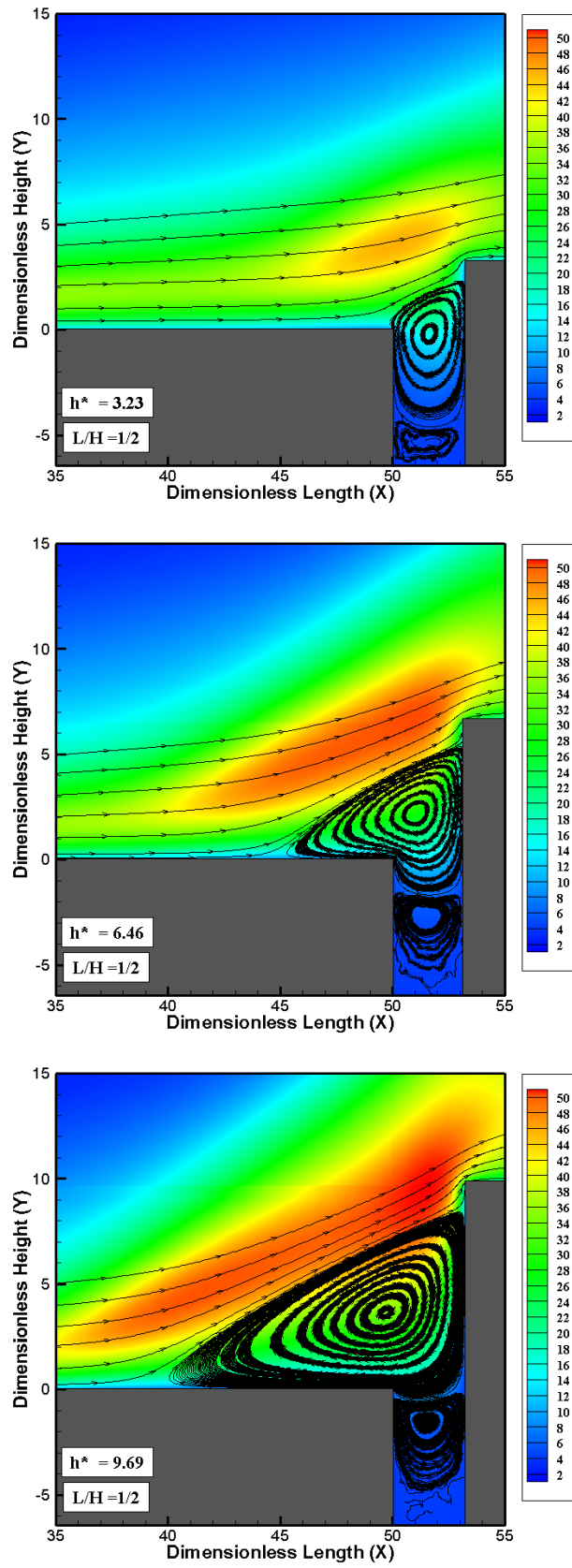
Figure 5.32 - Overall temperature ratio $(T_o/T_\infty)$ contour maps around the combined gap/step geometry with $L/H$ ratio of $1/2$ and frontal-face thickness of $h^* = 3.23$ (top), 6.46 (middle), and 9.69 (bottom).
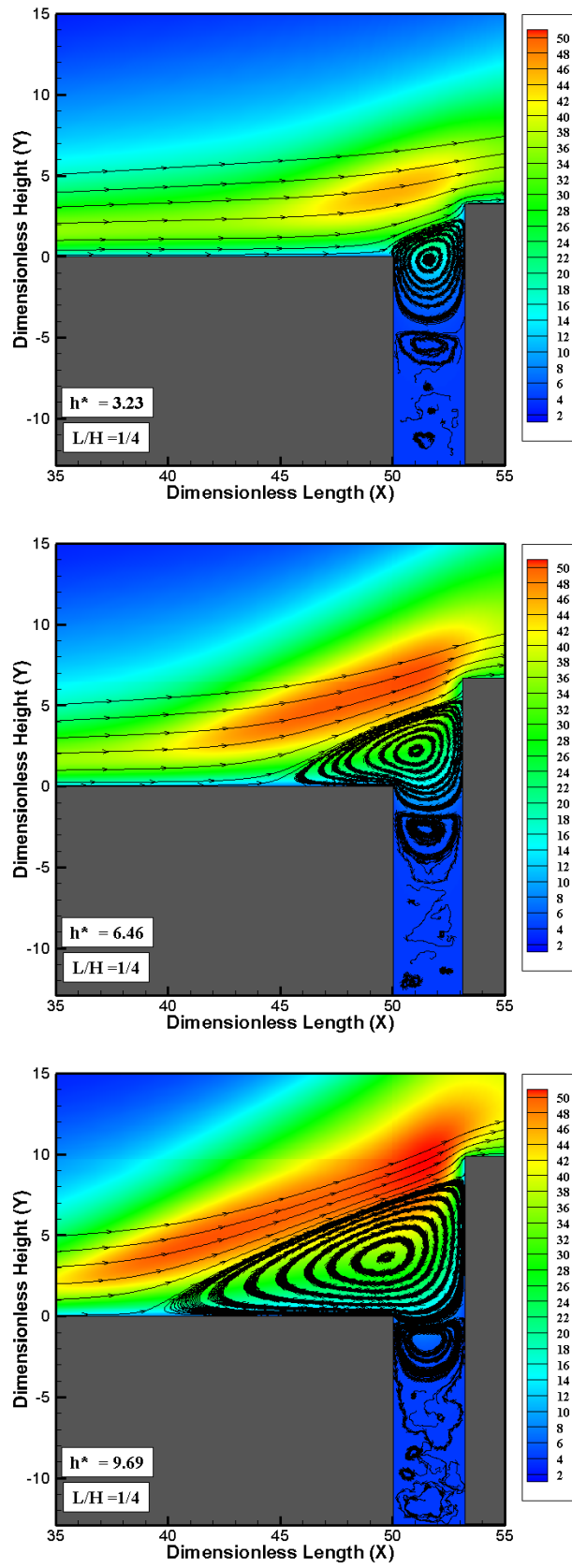
Figure 5.33 - Overall temperature ratio $(T_o/T_\infty)$ contour maps around the combined gap/step geometry with $L/H$ ratio of $1/4$ and frontal-face thickness of $h^* = 3.23$ (top), 6.46 (middle), and 9.69 (bottom).

step frontal-face height on the temperature behavior ahead of the step. It is clearly seen that temperature in this region increases with increasing the step frontal-face.

## 5.2 Aerodynamic Surface Quantities

The purpose of this section is to discuss and to compare differences in the aerodynamic surface quantities due to variations on the the gap $L/H$ ratio, and on the step frontal-face height $h$ in a combined gap/step geometry. The aerodynamic surface properties of particular interest in this work are the number flux, pressure, skin friction and heat transfer coefficients. Before proceeding with this analysis, it is important to emphasise that the thermal and pressure loads of special relevance in this study, are discussed only for surfaces S1, S4, and S5. As these loads are irrelevant to the other surfaces, they will not be shown.

### 5.2.1 Number Flux

The number flux, $N$, is calculated by sampling the molecules impinging on the surface by unit of time and unit of area. The effect of the gap $L/H$ ratio and the step frontal-face height $h$ on the number flux along surfaces S1, S4, and S5 in a combined gap/step geometry is discussed in the subsequent subsections.

#### 5.2.1.1 Gap $L/H$ Ratio Effect

Number flux along surfaces S1, S4 and S5 is illustrated in Fig. 5.34, parameterized by the gap $L/H$ ratio. In this set of plots, $N_f$ represents the number flux $N$ normalized by $n_\infty U_\infty$, where $n_\infty$ is the freestream number density, and $U_\infty$ is the freestream velocity. Filled and empty symbols correspond to the dimensionless step height $h^*$ of 3.23, and 9.69, respectively. Also, $X$ and $Y$ are the length $x$ and height $y$ normalized by the freestream mean free path $\lambda_\infty$. According to these plots, it is observed that the gap $L/H$ ratio changes do not affect the number flux along these surfaces for the gap $L/H$ ratio investigated. With this perspective in mind, the analysis of the step frontal-face effect in the subsequent subsection will consider just one gap $L/H$ ratio, say $L/H = 1/4$.

#### 5.2.1.2 Step Frontal-face Thickness Effect

The distribution of the number flux along the combined gap/step surfaces – upstream (surface S1), downstream (surface S5), and frontal-face (surface S4) – is illustrated in Fig. 5.35 for dimensionless step height $h^*$ of 3.23, and 9.69. As a basis of comparison, the dimensionless number flux $N_f$ for the forward-facing step (LEITE,

Figure 5.34 - Distribution of dimensionless number flux $N_f$ along surfaces (a) S1/S5 and (b) S4 for dimensionless step height $h^*$ of 3.23 and 9.69, and gap $L/H$ ratio of 1, 1/2, and 1/4 in a gap/step configuration.

2009), the gap (PAOLICCHI, 2011), and for the flat-plate (LEITE; SANTOS, 2011) case are also illustrated in Fig. 5.35. In addition, the combined gap/step case with $h^* = 6.46$ is a intermediate case, and it will not be shown in these plots. It is important to remark that the flat-plate case corresponds to a flat-plate without a gap/step configuration, i.e., a smooth surface.

Looking first at Fig. 5.35(a), it is seen that the dimensionless number flux $N_f$ along surface S1 depends on the step frontal-face height $h$, for the conditions investigated. From the leading edge up to a station close to the separation point $X_s$, the number flux behavior for the combined gap/step, the forward-facing step, and the gap case, is similar to that for the flat-plate case. This is an expected behavior in the sense that this region is not affected by the presence of the combined gap/step, the forward-facing step, or the gap. As a base of comparison, the separation point $X_s$, for the combined gap/step configuration with the gap $L/H$ ratio of 1/4, takes place at section 50.0, 46.38, and 40.62 (see tab.5.1), for dimensionless step height $h^*$ of 3.23, 6.46, and 9.69, respectively. In addition, for the forward-facing step case, the separation point is located at section 48.33, 42.86, and 37.34, for dimensionless step height $h^*$ of 3.23, 6.46, and 9.69, respectively.

As the flow develops downstream along surface S1, it is observed that the presence of the step frontal-face is felt first in the forward-facing step, followed by the combined
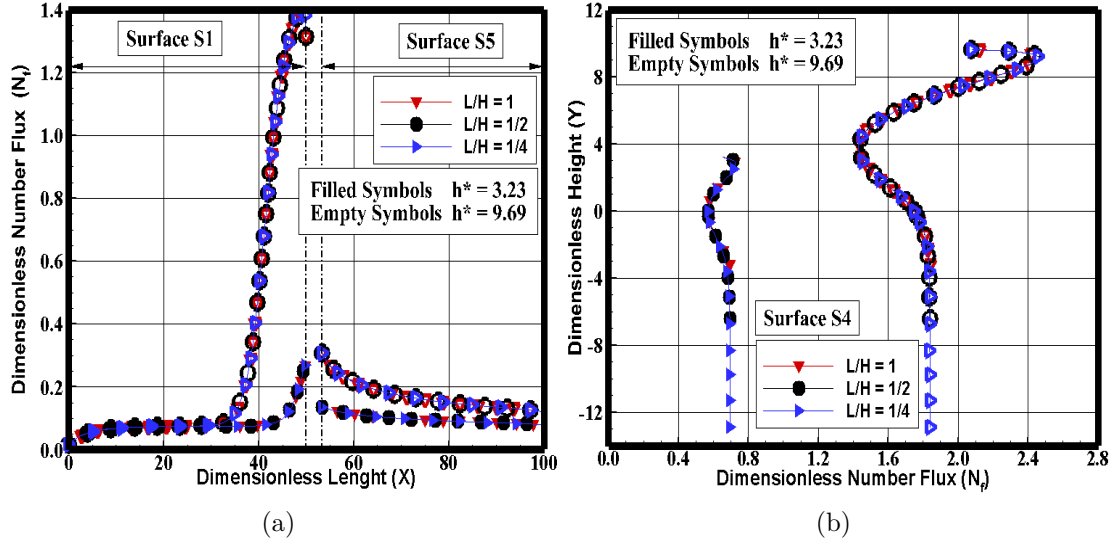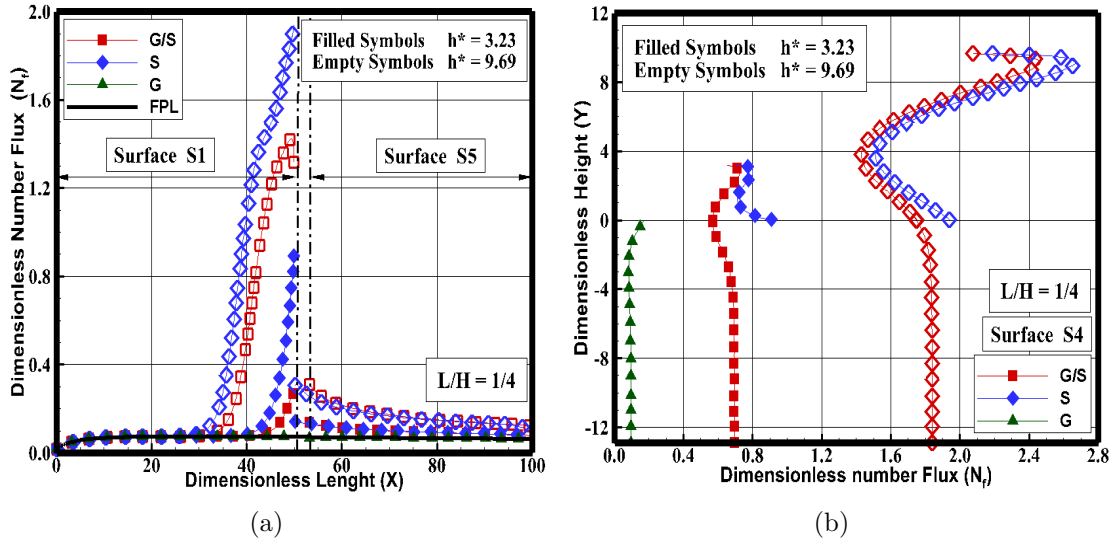
Figure 5.35 - Distribution of the dimensionless number flux $N_f$ along surfaces (a) S1/S5, and (b) S4 for dimensionless step height $h^*$ of 3.23 and 9.69, and gap $L/H$ of 1/4.

gap/step configuration. In addition, in the vicinity of the step face, the number flux to surface S1 dramatically increases in comparison to the number flux observed for the flat-plate case. Moreover, the number flux rise for the forward-facing step is larger than that for the combined gap/step configuration. Therefore, one of the effects of a gap in the combined gap/step configuration is to reduce significantly the number flux in this region. This behavior is explained by the fact that, for the forward-facing step, the density ratio $\rho/\rho_\infty$ presents its maximum value at the step concave corner, i.e., at the step base. In contrast, for the combined gap/step configuration, $\rho/\rho_\infty$ presents its maximum value inside the gap, as was shown in Figs. 5.15, 5.16, and 5.17.

Still referring to Fig. 5.35(a), it is noticed that, along surface S5, the number flux behavior for the gap/step configuration is similar to that for the forward-facing step case. The number flux $N_f$ presents high values in the vicinity of the surface-S4/surface-S5 junction, and then it approaches the values for the flat-plate and the gap cases downstream along the surface, for the step height $h$ investigated.

Turning next to Fig. 5.35(b), it is seen that the number flux to the frontal-face surface, surface S4, is more intense than that observed to the upstream surface, surface S1. Similar to that for the upstream surface, the number flux to the frontal-face is a function of the step height $h$, i.e, it increases with increasing the step

frontal-face height. It may be recognized from these plots that the number flux distribution presents a peak value at the vicinity of the step corner, i.e., in the vicinity of the surface-S4/surface-S5 junction. These peak values for the gap/step configuration take place at section $Y$ equal to 2.77, 5.90, and 9.13 for step height $h^*$ of 3.23, 6.46, and 9.69, respectively. As a matter of fact, the flow reattachment point, $Y_r$, on the frontal-face of the gap/step configuration, occurs at section $Y$ equal to 2.73, 5.60 and 8.68 for $h^*$ of 3.23, 6.46, and 9.69, respectively (see Tab. 5.1). In this sense, it is noteworthy to emphasize that the peak values in the number flux is related to the reattachment point at the step frontal-face in a combined gap/step configuration.

### 5.2.2 Pressure Coefficient

The pressure coefficient $C_p$ is defined as follows,

$$C_p = \frac{p_w - p_\infty}{\frac{1}{2}\rho_\infty U_\infty^2} \tag{5.8}$$

where $p_w$ is the wall pressure.

The wall pressure $p_w$ on the body surface is calculated by the sum of the normal momentum fluxes of both incident and reflected molecules at each time step as follows,

$$p_w = p_i - p_{rf} = \frac{F_N}{A\Delta t} \sum_{j=1}^{N} \{[(mv)_j]_i - [(mv)_j]_{rf}\} \tag{5.9}$$

where $F_N$ is the number of real molecules represented by a single simulated molecule, $\Delta t$ is the time step, $A$ stands for the surface area, $N$ is the number of molecules colliding with the surface by unit time and unit area, $m$ is the mass of the molecules, and $v$ is the velocity component of the molecule $j$ in the surface normal direction. Subscripts $i$ and $rf$ refer to incident and reflect molecules.

#### 5.2.2.1 Gap $L/H$ Ratio Effect

The impact on the pressure coefficient $C_p$, along surfaces S1, S4, and S5 in a gap/step configuration, due to changes in the gap $L/H$ ratio, is displayed in Fig. 5.36. Based

Figure 5.36 - Distribution of pressure coefficient $C_p$ along surfaces (a) S1/S5 and (b) S4 for dimensionless step height $h^*$ of 3.23 and 9.69, and gap $L/H$ ratio of 1, 1/2, and 1/4 in a gap/step configuration.

on these plots, it is noticed that, similar to the dimensionless number flux, the pressure coefficient along these surfaces is not affected by changes on the gap $L/H$ ratio, for the range investigated.

### 5.2.2.2 Step Frontal-face Thickness Effect

The effect on the pressure coefficient $C_p$, along surfaces S1, S4, and S5 in a combined gap/step, due to the variation in the step frontal-face height $h^*$ is depicted in Fig. 5.37. Again in this set of plots, results for the step (LEITE, 2009), the gap (PAOLICCHI, 2011), and the flat-plate (LEITE; SANTOS, 2011) cases are also displayed.

Referring to Fig. 5.37(a), it is observed that the pressure coefficient $C_p$ follows the same trend as that presented by the dimensionless number flux $N_f$ in the sense that, along surface S1, the pressure coefficient displays the same behavior as that for the forward-facing step, the gap, and the flat-plate case up to the corresponding separation point. In the vicinity of the step face, the pressure coefficient along surface S1 increases in comparison to the pressure coefficient observed for the flat-plate case. In addition, similar to the number flux behavior, the pressure coefficient rise for the forward-facing step is larger than that for the combined gap/step configuration. This behavior is explained by the fact that, for the gap/step configuration, the flow expands at the gap convex corner, i.e., at the surface-S1/surface-S2 junction. As a
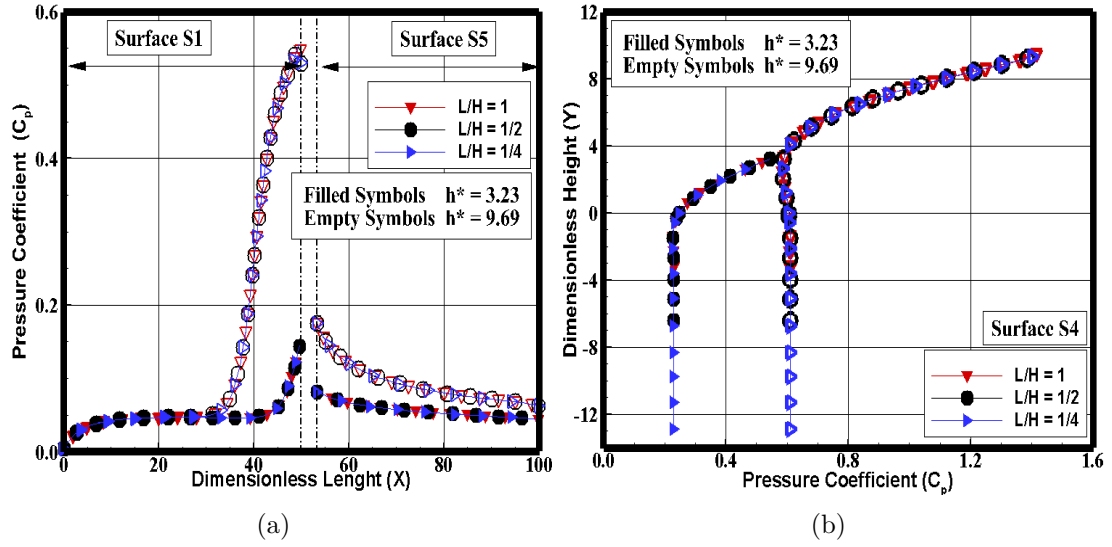
134

Figure 5.37 - Distribution of pressure coefficient $C_p$ along surfaces (a) S1/S5 and (b) S4 for dimensionless step height $h^*$ of 3.23 and 9.69, and gap $L/H$ ratio of 1/4.

result, this flow expansion reduces the pressure coefficient close to the gap corner. Along surface S5, the pressure coefficient behavior for the gap/step configuration is similar to that for the forward-facing step case. $C_p$ presents high values in the vicinity of the surface-S4/surface-S5 junction and then it approaches the flat-plate case values downstream along the surface for the step height $h$ investigated.

According to Fig. 5.37(b), it is clearly seen that the pressure coefficient $C_p$ for the combined gap/step configuration follows the same behavior as that shown for the forward-facing step case. The pressure coefficient $C_p$ increases by increasing the step frontal-face $h$. Similar to the forward-facing step case, peak values for the gap/step configuration take place in the vicinity of the step convex corner, i.e., close to the surface-S4/surface-S5 junction. In addition, it is also observed that peak values on the step frontal-face are larger than those on surface S1. For comparison purpose, maximum values for $C_p$ on the frontal-face of a combined gap/step configuration are around 0.55, 0.97 and 1.41 for dimensionless height $h^*$ of 3.23, 6,46 and 9.69, respectively. Conversely, the maximum value of $C_p$ for the flat-plate case, i.e., a flat plate without a gap/step configuration, is around 0.047 at section $X = 27.13$ on surface S1. Therefore, $C_p$ of 0.55, 0.97 and 1.41 correspond respectively to 11.7, 20.6 and 30.0 times the peak value for the flat-plate case, which corresponds to a smooth surface.

Still referring to Fig. 5.37(b), inside the gap, the pressure coefficient presents a lower

value at surface-S3/surface-S4 junction, and increases monotonically upward along the surface, reaching the peak value at the step shoulder (surface-S4/surface-S5 junction). Similar to the number flux behavior, this is an expected behavior, since these peak values are related to the reattachment point of the flow near to the step corner. The reason for that is because of the molecules that are confined in the clockwise recirculation region in front of the frontal-face surface collide with the wall at the reattachment point.

### 5.2.3  Skin Friction Coefficient

The skin friction coefficient $C_f$ is defined as follows,

$$C_f = \frac{\tau_w}{\frac{1}{2}\rho_\infty U_\infty^2} \tag{5.10}$$

The shear stress $\tau_w$ on the body surface is calculated by the sum of the tangential momentum fluxes of both incident and reflected molecules impinging on the surface at each time step by the following expression,

$$\tau_w = \tau_i - \tau_{rf} = \frac{F_N}{A\Delta t} \sum_{j=1}^{N} \{[(mu)_j]_i - [(mu)_j]_{rf}\} \tag{5.11}$$

where $u$ is the velocity component of the molecule $j$ in the surface tangential direction. Subscripts $i$ and $rf$ refer to incident and reflect molecules.

It is worthwhile to note that, for the special case of diffuse reflection, the gas-surface interaction model adopted in present work, the reflected molecules have a tangential moment equal to zero, since the molecules essentially lose, on average, their tangential velocity components. In this fashion, the contribution of $\tau_{rf}$ in Eq. 5.11 is equal to zero.

### 5.2.3.1  Gap $L/H$ Ratio Effect

Figure 5.38 presents the impact on the skin friction coefficient $C_f$ along surfaces S1, S4, and S5, due to changes in the gap $L/H$ ratio in a combined gap/step configuration. It is seen from these plots, that the gap $L/H$ ratio changes do not affect the skin friction coefficient along these surfaces.
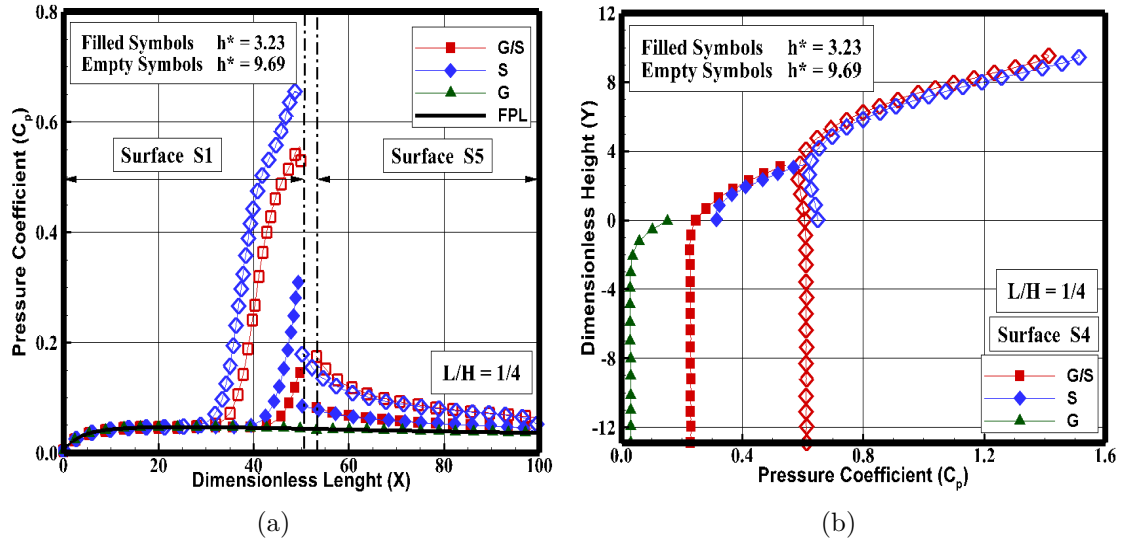
Figure 5.38 - Distribution of skin friction coefficient $C_f$ along surfaces (a) S1/S5 and (b) S4 for dimensionless step height $h^*$ of 3.23 and 9.69, and gap $L/H$ ratio of 1, 1/2, and 1/4 in a gap/step configuration.

### 5.2.3.2 Step Frontal-face Thickness Effect

The impact on the skin friction coefficient $C_f$ due to changes on the step height $h^*$ is demonstrated in Fig. 5.39, for surfaces S1, S4, and S5 in a combined gap/step geometry. Looking first to Fig. 5.39(a), it is observed that the upstream disturbances in the gap/step configuration, due to the presence of the step frontal-face, are felt in the skin friction coefficient $C_f$ close to the separation point. From this position up to the gap position, $X = 50$, the skin friction coefficient $C_f$ decreases, when compared to that for the flat-plate case, and reaches zero for section $X$ of 46.4 and 40.6 for dimensionless step height $h^*$ of 6.46 (not shown) and 9.69, respectively. After that, as a result of the recirculation region, the skin friction coefficient $C_f$ continues to decrease up to the end of surface S1. This behavior is in contrast to that for forward-facing step (LEITE, 2009), as shown in Fig. 5.39(a). For the forward-facing step, the skin friction coefficient reaches zero for section $X$ of 48.3, 42.8, and 37.3, for dimensionless step height $h^*$ of 3.23, 6.46, and 9.69, respectively. After that, as a result of the recirculation region, the skin friction coefficient $C_f$ continues to decrease up to a minimum point. After the minimum point, $C_f$ increases again and reaches positive values at the base of the step.

Along surface S5, similar to the pressure coefficient, it is noticed that the skin friction coefficient $C_f$ is larger than that for the flat-plate case, especially in the
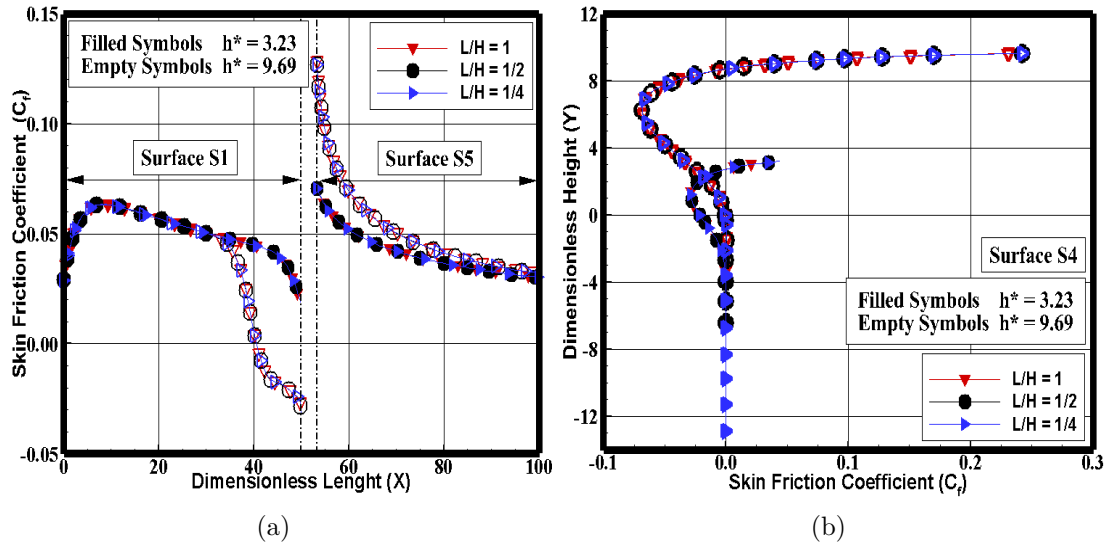
137

Figure 5.39 - Distribution of skin friction coefficient $C_f$ along surfaces (a) S1/S5 and (b) S4 for dimensionless step height $h^*$ of 3.23 and 9.69, and gap $L/H$ ratio of 1/4.

vicinity of the step convex corner, defined by the surface-S4/surface-S5 junction. However, as the flow moves downstream along the surface, the skin friction coefficient $C_f$ basically tends to the value observed for the flat-plate case. In addition, no appreciable differences are observed in the skin friction coefficient for the gap/step configuration in comparison to that for the forward-facing step. Finally, it is observed that the peak values for the skin friction coefficient $C_f$ along surfaces S1 and S5 are lower than those observed for the pressure coefficient (see Fig. 5.37). As a result, tangential forces, associated to the shear stress, are lower than normal forces, related to the wall pressure.

Focusing next on Fig. 5.39(b), it is clearly seen that the skin friction coefficient $C_f$ for the gap/step configuration follows the same trend as that exhibited by the forward-facing step, where the peak values take place at the step convex corner.

Usually, as $C_f$ changes from positive to negative value, the condition $C_f = 0$ may indicate the presence of a backflow, an attachment or reattachment point in the flow. In the present account, these changes are directly related to the clockwise and counterclockwise recirculation region in front of the step and inside the gaps, respectively, in the combined gap/step geometry.

### 5.2.4  Heat Transfer Coefficient

The heat transfer coefficient $C_h$ is defined as follows,

$$C_h = \frac{q_w}{\frac{1}{2}\rho_\infty U_\infty^3} \tag{5.12}$$

where $q_w$ is the heat flux to the body surface.

The heat flux $q_w$ is calculated by the net energy flux of the molecules impinging on the surface. A flux is regarded as positive if it is directed toward the body surface. The net heat flux $q_w$ is related to the sum of the translational, rotational and vibrational energies of both incident and reflected molecules as defined by,

$$q_w = q_i - q_{rf} = \frac{F_N}{A\Delta t}\{\sum_{j=1}^{N}[\frac{1}{2}m_j c_j^2 + e_{rj} + e_{vj}]_i - \sum_{j=1}^{N}[\frac{1}{2}m_j c_j^2 + e_{rj} + e_{vj}]_{rf}\} \tag{5.13}$$

where $c$ is the velocity of the molecules, $e_r$ and $e_v$ stand for rotational and vibrational energies, respectively.

#### 5.2.4.1  Gap $L/H$ Ratio Effect

Figure 5.40 presents the influence on the heat flux coefficient $C_h$ along surfaces S1, S4 and S5, due to changes in the gap $L/H$ ratio in a combined gap/step configuration. It is seen from these plots that, similar to the other surface quantities, the gap $L/H$ ratio changes do not affect the heat flux coefficient along these surfaces, for the range investigated.

#### 5.2.4.2  Step Frontal-face Thickness Effect

The sensitivity of the heat transfer coefficient $C_h$ is demonstrated in Fig. 5.41 for surfaces S1 and S5, and for surface S4 in a combined gap/step geometry. According to Fig. 5.41(a), along surface S1, the heat transfer coefficient $C_h$ for the gap/step configuration follows the same behavior presented by the flat-plate case close to the sharp leading edge, region unaffected by the presence of the gap/step, the forward-facing step or the gap configuration. Further downstream along surface S1, the heat transfer coefficient $C_h$ significantly increases and reaches peak values in the vicinity of the surface-S1/surface-S2 junction. These peak values is probably due to the
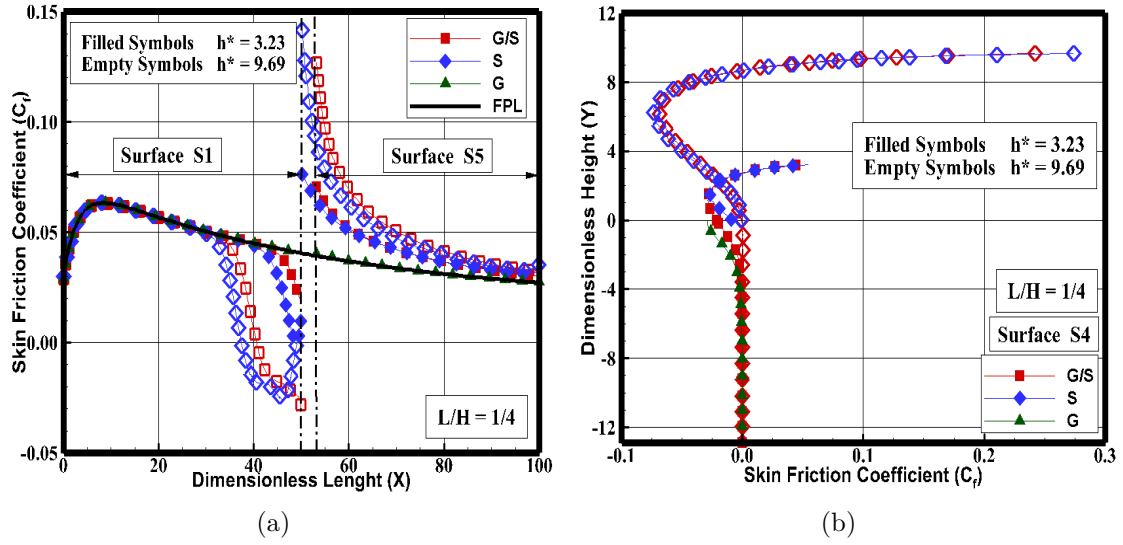
Figure 5.40 - Distribution of heat transfer coefficient $C_h$ along surfaces (a) S1/S5 and (b) S4 for dimensionless step height $h^*$ of 3.23 and 9.69, and gap $L/H$ ratio of 1, 1/2, and 1/4 in a gap/step configuration.

recirculation region in front of the steps. For comparison purpose, in a combined gap/step case with step height $h^*=$ 3.23, and 9.69, the maximum heat transfer coefficient occurs around the position $X$ of 50, and 40, respectively. Accordingly to Tab.5.1, the separation point on surface S1 is exactly at position $X$ of 50.0 and 40.6 for dimensionless step height $h^* =$ 3.23 and 9.69, respectively.

Still referring to Fig. 5.41(a), along surface S5, it is observed that the heat transfer coefficient $C_h$ for the gap/step configuration is larger than that for the flat-plate case, and slightly larger than that for the forward-facing step, in the vicinity of the step convex corner, defined by the surface-S4/surface-S5 junction. Nevertheless, as the flow moves downstream along surface S5, the heat transfer coefficient $C_h$ basically recovers the value obtained for the flat-plate case.

Along surface S4, Fig. 5.41(b), the heat transfer coefficient increases monotonically, from zero at surface-S3/surface-S4 junction to a maximum value near the step convex corner. The maximum value depends on the frontal-face height $h$. It is quite apparent that this significant increase in the heat transfer coefficient is due to the flow reattachment zone. It is important to mention that peak values observed for the heat transfer coefficient on the step frontal-face surface is one order of magnitude larger than those observed on surface S1. The reason for that is because the step face acts as a stagnation region for the reattaching shear layer (AUXER et al., 1969).
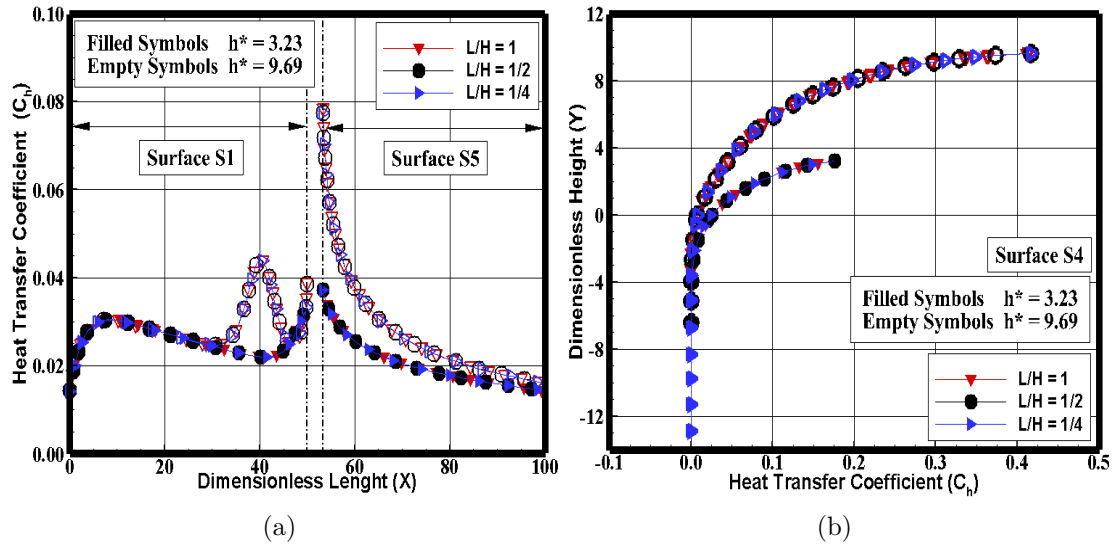
140
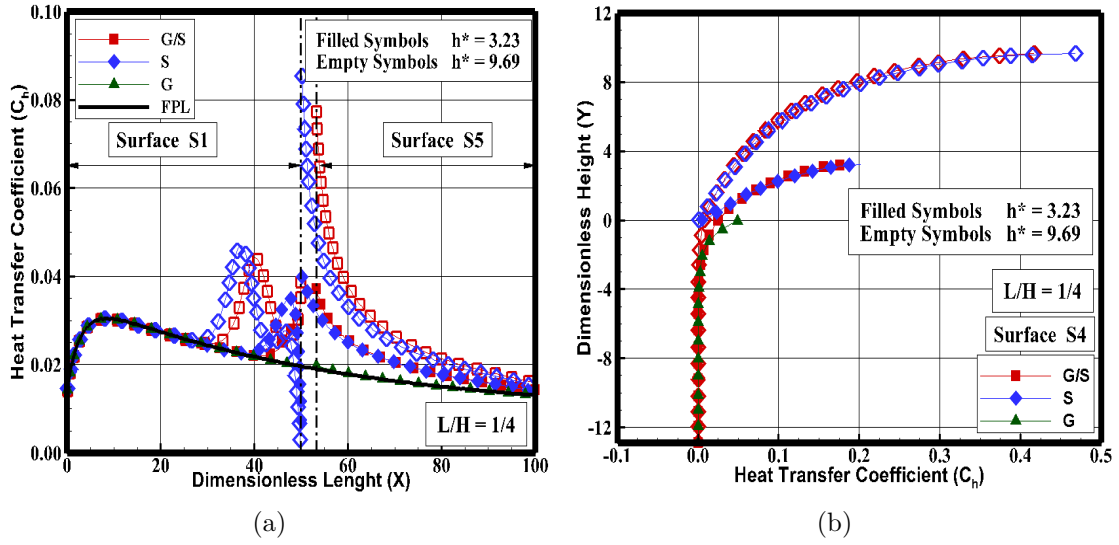
Figure 5.41 - Distribution of heat transfer coefficient $C_h$ along surfaces (a) S1/S5 and (b) S4 for dimensionless step height $h^*$ of 3.23 and 9.69, and gap $L/H$ ratio of 1/4.

As a base of comparison, the maximum values for $C_h$ are around 0.18, 0.30 and 0.41 for dimensionless height $h^*$ of 3.23, 6,46 and 9.69, respectively. In contrast, the $C_h$ for the flat-plate case, i.e., a flat-plate without discontinuities, is around 0.030 at section $X = 9.1$ on surface S1. Therefore, $C_h$ of 0.18, 0.30 and 0.41 correspond respectively to 6.0, 10.0 and 13.7 times the peak value for the flat-plate case.

Finally, the heat flux to the combined gap/step surfaces was defined in terms of the incident and reflected flow properties, Eq. 5.13, and based upon the gas-surface interaction model of fully accommodated, complete diffuse reemission. The diffuse model assumes that the molecules are reflected equally in all directions, quite independently of their incident speed and direction. Due to diffuse reflection model, the reflected velocity of their molecules impinging on the gap/step surfaces is obtained from a Maxwellian distribution that takes into account for the temperature of the surfaces. In this fashion, according to Eq. 5.13, not only the number of molecules impinging on the surface but also the wall temperature plays a important role on the reflected contribution to the net heat flux to the combined gap/step surface.

## 5.3 Numerical and Experimental Comparison

The distribution of wall pressure $p_w$ along the upstream (surface S1), frontal-face (surface S4), and downstream (surface S5) surfaces and temperature ratio $T/T_\infty$ for two sections over surfaces S1 and S5 of a combined gap/step (G/S) geometry with

step height $h^* = 3.23$ and gap $L/H$ ratio of 1, may be qualitatively compared to those for the forward-facing step (S) case that was presented by Pullin & Harvey (PULLIN; HARVEY, 1977) and Leite (LEITE, 2009), which investigated a rarefied hypersonic flow over forward-facing steps by employing the DSMC method. In their study, Pullin & Harvey (PULLIN; HARVEY, 1977) employed $N_2$ as the working fluid, freestream Mach number $M_\infty$ of 22.9, and freestream temperature $T_\infty$ of 20 K. The forward-facing step, located at 48 $\lambda_\infty$ downstream of the flat-plate leading edge, was kept to a wall temperature $T_w$ of 288 K, which corresponds to $T_w/T_\infty$ = 14.4. Although it is not directly defined in the technical note, the frontal-face height $h$ was in the range of $3\lambda_\infty < h < 5\lambda_\infty$. According to the authors, the flow and body conditions where chosen in order to reproduce experiments conducted by Jeffrey (JEFFREY, 1973), a private communication cited by Pullin & Harvey (PULLIN; HARVEY, 1977). The freestream and flow conditions used for the combined gap/step and for the forward-facing steps investigations are tabulated in Tab. 5.2.

Table 5.2 - Comparison between the freestream and flow conditions used for a combined gap/step and a forward-facing steps simulations.

| Work | Gas | $M_\infty$ | $T_\infty$ (K) | $T_w$ (K) | $T_w/T_\infty$ | h/$\lambda_\infty$ | L |
|---|---|---|---|---|---|---|---|
| Pullin & Harvey (1977)(S) | $N_2$ | 22.9 | 20.00 | 228 | 14.4 | 3 to 5 | $48\lambda_\infty$ |
| Leite (2009)(S) | $O_2;N_2$ | 25.0 | 219.69 | 880 | 4.0 | 3.23 | $50\lambda_\infty$ |
| Present work (G/S) | $O_2;N_2$ | 25.0 | 219.69 | 880 | 4.0 | 3.23 | $50\lambda_\infty$ |

### 5.3.1 Wall Pressure

Figure 5.42 displays the pressure ratio $p_w/p_\infty$ along surfaces S1, S4, and S5 for the forward-facing step, which was experimentally investigated by Jeffrey (JEFFREY, 1973), and numerically by Pullin & Harvey (PULLIN; HARVEY, 1977) and Leite (LEITE, 2009). For comparison purpose, the gap/step results with step height $h^*$ = 3.23 and gap $L/H$ ratio of 1 are also displayed. In this set of plots, $X'$ and $Y$ are, respectively, the horizontal length $(x - L_u)$ and the vertical height $y$, normalized by the mean free path $\lambda_\infty$. According to Fig. 5.42, the comparison presents a good qualitative agreement on the pressure ratio distribution along the upstream (S1), frontal-face (S4), and downstream (S5) surfaces of a combined gap/step with the step results. Despite of some differences in terms of the flow conditions, summarized in Tab. 5.2, the comparison seems to be relevant in the sense that the pressure ratio
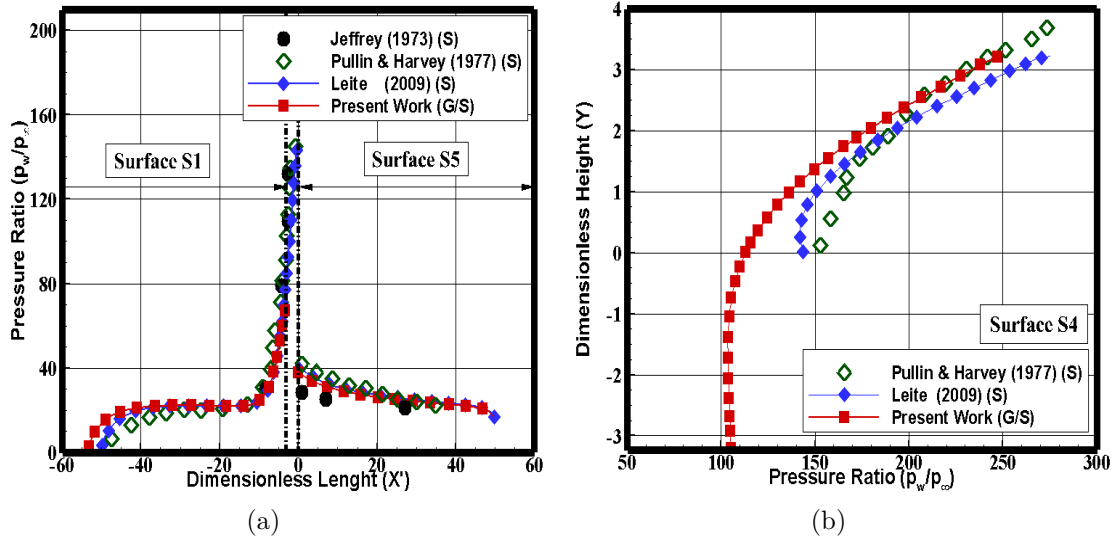
Figure 5.42 - Comparison of pressure ratio ($p_w/p_\infty$) distribution acting along (a) upstream (S1) and downstream (S5) surfaces, and along (b) the frontal-face (S4) of a combined gap/geometry.

$p_w/p_\infty$ demonstrates a similar trend for the three cases investigated.

## 5.3.2  Kinetic Temperature Field

Figure 5.43 displays the kinetic temperature ratio profiles for two sections on surfaces S1 and S5 for a combined gap/step configuration with $h^* = 3.23$ and $L/H = 1$, in comparison with the forward-facing step case investigated by Pullin & Harvey (PULLIN; HARVEY, 1977), and by Leite (LEITE, 2009). Again in this set of plots, X' and Y are, respectively, the horizontal length $(x - L_u)$ and the vertical height $y$ normalized by the mean free path $\lambda_\infty$. Also, filled and empty symbols stand for translational $T_t$ and rotational $T_r$ temperatures, respectively, normalized by the freestream temperature $T_\infty$.

It could be inferred from Fig. 5.43 that the flow is in a highly non-equilibrium state, since there is a lack of equilibrium of the translational and rotational temperatures. Thermal non-equilibrium occurs when the temperatures associated with translational, and rotational modes of a polyatomic gas are different one to each other. It is clearly seen from Fig. 5.43 that kinetic temperatures reach a value on the upstream (S1) and downstream (S5) surfaces that is above to the wall temperature, resulting in a temperature jump, as defined in continuum formulation. It is also seen that the temperature related to the gap/step (G/S) configuration has the same trend to that observed for the forward-facing step (S) case investigated by Leite (LEITE, 2009).

143

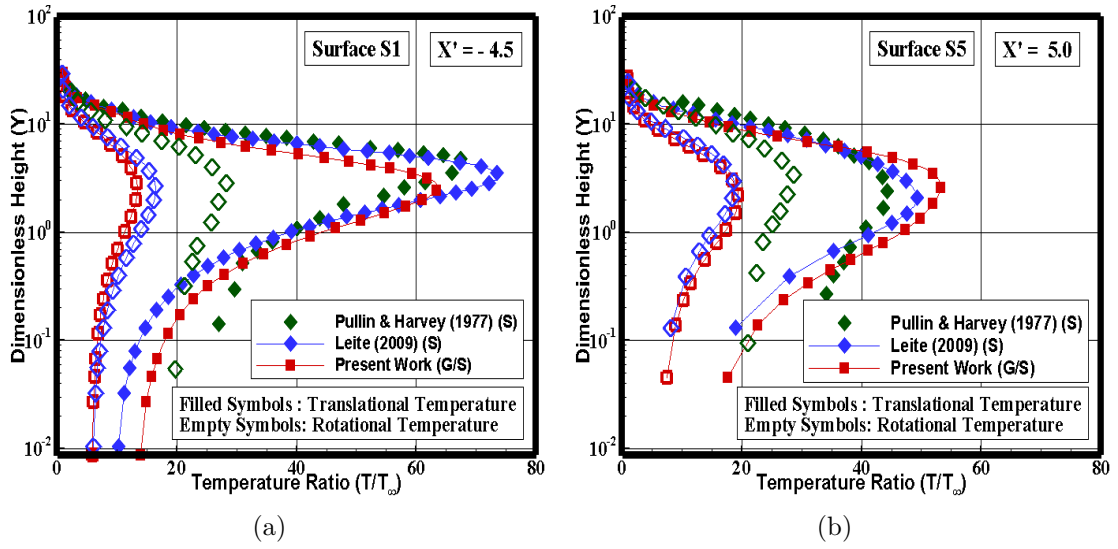Figure 5.43 - Distribution of kinetic temperature ratio $(T/T_\infty)$ profiles for two sections on (a) upstream (S1) and downstream (S5) surfaces, of a combined gap/geometry.

Some differences in the results presented by Pullin & Harvey (PULLIN; HARVEY, 1977) might be attributed to differences in freestream and flows conditions used in the investigations, as tabulated in Tab.5.2.

# 6 CONCLUSIONS

## 6.1 Concluding Remarks

A computational analysis has been carried out in order to investigate a two-dimensional rarefied hypersonic flow over a gap/step configuration by employing the Direct Simulation Monte Carlo method. In the present account, the gap/step configuration models a misalignment observed between individual tiles in the thermal protection system of reentry vehicles, such as the Space Shuttle Orbiter. The main focus was to analyze the effects of the gap $L/H$ ratio and the step frontal-face height $h$ on the flowfield properties, such as velocity, density, pressure, and kinetic temperature, and on the aerodynamic surface quantities, such as number flux, heat transfer, pressure, and skin friction coefficients that were presented separately outside and inside the gap/step configuration by a numerical method that properly accounts for non-equilibrium effects. Results for a combined gap/step configuration, defined by gap $L/H$ ratio of 1, 1/2, and 1/4, and step frontal-face height $h$ of 3, 6, and 9 millimeters, were compared to those of a forward-facing step, a gap, and a flat-plate case.

For the conditions used in the present investigation, it was observed that the gap $L/H$ ratio changes in a combined gap/step did not disturb significantly the primary flowfield properties and the aerodynamic coefficients far upstream and downstream the gap/step position, and neither the aerodynamic surface coefficients along the gap/step frontal-face surface. Inside the gap, the primary properties tend to a constant value at the bottom surface with decreasing the $L/H$ ratio.

Conversely, the analysis showed that the upstream disturbance imposed by the combined gap/step configuration increased with increasing the step frontal-face height $h$. As a consequence, it was found that the aerodynamic heating and pressure loads were affected by the the step frontal-face height changes. It was evident that these loads increased with increasing the step frontal-face. Consequently, maximum values occur on the step face, more precisely at the vicinity of the step shoulder. In addition, these loads are much higher than the maximum values found for a smooth surface, i.e., a flat plate without a gap/step configuration.

Additionally, it was found that step frontal-face acts as a barrier in the sense that part of the flow enters into the gap increasing the number of molecules inside the gap. As a consequence, density and pressure inside the gap in a combined gap/step configuration dramatically increased when compared to those observed for the gap

configuration, i.e., a gap without a step, due to the presence of the step.

The analysis showed that as the step height $h^*$ increases from 3.23 to 9.69, the primary recirculation region, in the clockwise direction inside the gap tends to move outside, toward the front of the step, and this recirculation region increases with increasing $h^*$. As a result, another recirculation region arises inside the gap in a counterclockwise direction.

## 6.2 Future Work

The present investigation has described an initial investigation of a hypersonic rarefied flow over a combined gap/step configuration in order to simulate a misalignment observed between individual tiles in the thermal protection system of hypersonic vehicles, such as the Space Shuttle Orbiter. Although this investigation has taken into account a representative range for the gap $L/H$ ratio, and step frontal-face height $h$, a number of improvements to a realistic investigation on surface discontinuities is still desirable.

Diffuse reflection was the model employed in this research. This model assumes that the molecules are reflected equally in all directions, quite independently of of their incident speed and direction. Nevertheless, as a space flight vehicle is exposed to a rarefied environment over a considerable time, a departure from the diffuse model is observed, resulting from the colliding molecules that clean the surface of the vehicle, which becomes gradually decontaminated. Molecules reflected from clean surfaces show lobular distribution in direction. In this way, incomplete surface accommodation effects might provide more insight into the sensitivity of the aerothermodynamic surface quantities to gas-surface model.

The DSMC method has been used to assess the flowfield structure on a combined gap/step configuration by considering constant wall temperature. In a realistic design, temperature not only changes along the body surface but also inside de gap and at the step. In this context, a more detailed analysis that includes the conjugate heat transfer problems seems to be a challenge.

Finally, the Mach number, chemical reactions, angle-of-attack, as well the geometrical effects, i.e., the distance $L_u$ in front of a combined gap/step configuration, might be included in this list.

# REFERENCES

ABE, T. Generalized scheme of the no-time-counter scheme for the dsmc in rarefied gas flows analisys. **Computers & fluids**, Elsevier, v. 22, n. 2, p. 253–257, 1993. 23, 26

ALEXANDER, F. J.; GARCIA, A. J.; ALDER, B. J. Consistent boltzmann algorithm. **Physical Review Letter**, APS, v. 74, n. 26, p. 5212–5215, 1995. 19

_____. Cell size dependence of transport coefficients in stochastic particle algorithm. **Physics of Fluids**, AIP Publishing, v. 10, n. 6, p. 1540–1542, 1998. 19, 21

_____. Erratum: Cell size dependence of transport coefficients in stochastic particle algorithms. **Physics of Fluids**, AIP Publishing, v. 12, n. 3, p. 731, 2000. 21

ANDERSON, J. **Modern compressible flow with historical perspective**. New York, EUA: McGrawHill, 1990. 50

AUXER, W.; NESTLER, D.; SAYDAH, A. Heat transfer to steps and cavities in hypersonic turbulent flow. **AIAA Journal**, v. 7, n. 7, p. 1368–1370, 1969. 140

BERGEMANN, F.; BOYD, I. New discrete vibrational energy model for the direct simulation monte carlo method. **Progress in Astronautics and Aeronautics**, American Institute of Aeronautics and Astronautics, v. 158, p. 174–174, 1994. 39, 42

BERTIN, J.; KEISNER, A. **Effect of step and/or gap tile misalignment on shuttle transition**. Austin, Texas, EUA, june 1978. 1, 8

BERTRAN, M.; WEINSTEIN, L.; JR., A. C.; ARRINGTON, J. Heat transfer to wavy wall in hypersonic flow. **AIAA Journal**, American Institute of Aeronautics and Astronautics, v. 5, n. 10, p. 1760–1767, 1967. 1, 6, 7, 11

BERTRAN, M.; WIGGS, M. Effect of surface distortions on the heat transfer to a wing at hypersonic speeds. **AIAA Journal**, v. 1, n. 6, p. 1313–1319, 1963. 1, 6, 7, 11

BIRD, G. **Molecular gas dynamics**. New York, EUA: Clarendon Press, Oxford, 1976. 18, 23, 26, 27, 72

_____. Monte-carlo simulation in an engineering context. **Progress in Astronautics and Aeronautics**, v. 74, p. 239–255, 1981. 28, 32, 34

_____. Definition of mean free path for real gases. **Physics of Fluids**, AIP Publishing, v. 26, n. 11, p. 3222–3223, 1983. 32, 56

_____. Direct simulation of high-vorticity gas flow. **Physics of Fluids**, AIP Publishing, v. 30, n. 2, p. 364–366, 1987. 19

_____. Perception of numerical methods in rarefied gasdynamics. **Progress in Astronautics and Aeronautics**, v. 117, p. 211–226, 1989. 23, 26, 27, 72

_____. **Molecular gas dynamics and the direct simulation of gas flows**. New York, EUA: Clarendon Press, Oxford, 1994. 5, 17, 18, 19, 23, 29, 31, 35, 37, 42, 44, 45, 46, 53, 57, 59, 66, 118

_____. Forty years of dsmc, and now? In: INTERNATIONAL SYMPOSIUM ON RAREFIED GAS DYNAMICS, 22th. **Proceedings...** Sidney, Australia: AIP Publishing, 2001. p. 372–380. 60

_____. A criterion for the breakdown of vibrational equilibrium in expansions. **Physics of Fluids**, AIP Publishing, v. 14, n. 5, p. 1732–1735, 2002. 43

_____. A comparison of collision energy-based and temperature-based procedures in dsmc. In: INTERNATIONAL SYMPOSIUM ON RAREFIED GAS DYNAMICS, 26th. **Proceedings...** Kyoto, Japan: Edited by T.Abe, 2008. v. 1084, p. 245–250. 36, 42, 43, 44, 56

_____. **The DSMC method**. Lexington, KY, EUA: Plenum Press, CreateSpace Independent Publishing Platform, 2013. 33, 36, 39, 40, 43, 44, 49, 50, 52, 54

BIRD, G.; LEVIN, D. A.; WYSONG, I. J.; GARCIA, A. L. Chemical reactions in dsmc. In: AIP CONFERENCE,V.1333, 1th. **Proceedings...** Pacific Grove, EUA: American Institute of Physics, 2011. p. 1195. 43

BORGNAKKE, C.; LARSEN, P. Statistical collision model for monte carlo simulation of polyatomic gas mixture. **Journal of Computational Physics**, Elsevier, v. 18, n. 4, p. 405–420, 1975. 35, 38, 56

BOYD, I. Rotational and vibrational nonequilibrium effects in rarefied hypersonic flow. **Journal of Thermophysics and Heat Transfer**, American Institute of Aeronautics and Astronautics, v. 4, n. 4, p. 478–484, 1990. 36, 42, 56, 72

_____. Direct simulation monte carlo for atmospheric entry part i: Theoretical basis and physical models. In: HYPERSONIC ENTRY AND CRUISE

VEHICLES, 1th. **Proceedings...** Stanford, Califórnia, EUA: Von Karman Institute for Fluid Dynamics, 2008. 39

BOYD, I. D. Analysis of rotational nonequilibrium in standing shock waves of nitrogen. **AIAA journal**, v. 28, n. 11, p. 1997–1999, 1990. 38, 42

_____. Rotational–translational energy transfer in rarefied nonequilibrium flows. **Physics of Fluids A: Fluid Dynamics**, AIP Publishing, v. 2, n. 3, p. 447–452, 1990. 41, 42

_____. Relaxation of discrete rotational energy distributions using a monte carlo method. **Physics of Fluids A: Fluid Dynamics**, AIP Publishing, v. 5, n. 9, p. 2278–2286, 1993. 39

_____. Computation of hypersonic flows using the direct simulation monte carlo method. **Journal of Spacecraft and Rockets**, American Institute of Aeronautics and Astronautics, v. 52, n. 1, p. 38–53, 2014. 16, 17, 24, 26, 38, 39, 47, 48, 49, 89

BURNETT, D. The distribution of molecular velocities and the mean motion in a non-uniform gas. **Proc. London Math. Soc.**, Oxford University Press, v. 2, n. 1, p. 382–435, 1936. 17

BURT, J. M.; JOSYULA, E. Techniques for reducing collision separation in direct simulation monte carlo calculations. In: AIAA THERMOPHYSICS CONFERENCE, 42th. **Proceedings...** Honolulu, Hawaii, EUA, 2011. 18, 19

CAIB. **Columbia accident investigation board report**. Florida, EUA, 2003. 3, 4

CERCIGNANI, C. **Mathematical methods in kinetic theory**. New York, EUA: Springer, 1969. 50

_____. **The boltzmann equation and its applications**. New York, EUA: Springer- Verlag, 1988. 16, 17

CHEN, G.; BOYD, I. Statistical error analysis for the direct simulation monte carlo technique. **Journal of Computational Physics**, Elsevier, v. 126, n. 2, p. 434–448, 1996. 20

DEEPAK, N.; GAI, S.; NEELY, A. A computational study of high enthalpy flow over a rearward facing step. In: AIAA AEROSPACE SCIENCES MEETING INCLUDING THE NEW HORIZONS FORUM AND AEROSPACE EXPOSITION, 48th., 2010. **Proceedings...** Orlando, EUA. 98

DIETRICH, S. Efficient computation of particle movement in 3-d dsmc calculations on structured body-fitted grids. In: 158 INTERNATIONAL SYMPOSIUM ON RAREFIED GAS DYNAMICS, 17th. **Proceedings...** Aachen, Germany: Edited by ED.A.E.Beylich, 1990. p. 745–752. 23

EVERHART, J. L.; ALTER, S. J.; MERSKI, N. R.; WOOD, W. A. Pressure gradient effects on hypersonic flow heating. In: AIAA AEROSPACE SCIENCES MEETING AND EXHIBIT, 44th. **Proceedings...** Reno, Nevada, EUA: AIAA, 2006. p. 0185. 2, 6, 7, 9, 11, 96

FALLAVOLLITA, M.; BAGANOFF, D.; MCDONALD, J. Reduction of simulation cost and error for particle simulations of rarefied flow. **Journal of Computational Physics**, Elsevier, v. 109, n. 1, p. 30–36, 1993. 20, 60, 61

GAB CONSULTING PTY. **The DS2G program user guide.** Killara, Australia, 1999. 1–56 p. 61

GAI, S.; MILTHORPE, J. Hypersonic high-enthalpy flow over a blunt-stepped cone. In: INTERNATIONAL SYMPOSIUM ON SHOCK WAVES, 20th. **Proceedings...** California, EUA: Edited by Sturtevant, B. and Shepherd, J.E and Hornung, H.G, v.1, 1995. p. 234–244. 6, 7, 11

GROTOWSKY, I.; BALLMANN, J. Numerical investigation of hypersonic step-flows. **Shock Waves**, Springer, v. 10, n. 1, p. 57–72, 2000. 6, 7, 8, 11

HAHN, M. Experimental investigation of separeted flow over a cavity at hypersonic speed. **AIAA Journal**, v. 7, n. 6, p. 1092–1098, 1969. 1, 6, 7, 11

HARVEY, J.; GALLIS, M. Review of code validation studies in high-speed low-density flows. **Journal of Spacecraft and Rockets**, v. 37, n. 1, p. 8–20, 2000. 18

HASSAN, H. A.; HASH, D. B. A generalized hard-sphere model for monte carlo simulation. **Physics of Fluids A: Fluid Dynamics**, AIP Publishing, v. 5, n. 3, p. 738–744, 1993. 28

HINDERSKS, M.; RADESPIED, R. Investigation of hypersonic gap flow of a reentry nosecap with consideration of fluid structure interaction. **AIAA Paper**, v. 6, p. 1111, 2006. 2, 6, 7, 11

HIRSCHFELDER, J. O.; CURTISS, C. F.; BIRD, R. B. **Molecular theory of gases and liquids**. New York, EUA: Wiley, 1954. 25

HOZUMI, K.; KOYAMA, T.; HIRABAYASHI, N. Experimental study on hypersonic heating characteristics of cavity wake flow. In: INTERNATIONAL CONGRESS OF THE AERONAUTICAL SCIENCES, 24th. **Proceedings...** Yokohama, Japan: AIAA, 2004. 6, 7, 11

JACKSON, A.; HILLIER, R.; SOLTANI, S. Experimental and computational study of laminar cavity flows at hypersonic speeds. **Journal of Fluid Mechanics**, Cambridge Univ Press, v. 427, p. 329–358, 2001. 6, 7, 11

JAKUBOWSKI, A.; LEWIS, C. Experimental study of supersonic laminar base flow with and without suction. **AIAA Journal**, v. 11, n. 12, p. 1670–1677, 1973. 6, 7, 11

JEFFREY, R. **Private Comunication**. London, England: Dept. of Aeronautics, Imperial College, 1973. 142

JI, M.; WANG, M. Sound generation by turbulent boundary-layer flow over small steps. **Journal of Fluid Mechanics**, Cambridge Univ Press, v. 654, p. 161–193, 2010. 98

_____. Surface pressure fluctuations on steps immersed in turbulent boundary layers. **Journal of Fluid Mechanics**, Cambridge Univ Press, v. 712, p. 471–504, 2012. 98

KABURAKI, H.; YOKOKAWA, M. Computer simulation of two-dimensional continuum flows by the direct simulation monte carlo method. **Molecular Simulation**, Taylor & Francis, v. 12, n. 3-6, p. 441–444, 1994. 27

KIM, H.; SETOGUCHI, T. Shock-induced boundary layer separation. In: INT. SYMP. OF EXPERIMENTAL AND COMPUTATIONAL AEROTHERMODYNAMICS OF INTERNAL FLOWS, 8th., 2007. **Proceedings...** Lyon, France. 98

KOURA, K. Null-collision technique in the direct simulation monte carlo method. **Physics of Fluids**, AIP Publishing, v. 29, n. 11, p. 3509–3511, 1986. 23, 26, 27, 71

_____. A sensitive test for accuracy in evaluation of molecular collision number in the direct-simulation monte carlo method. **Physics of Fluids A: Fluid Dynamics**, AIP Publishing, v. 2, n. 7, p. 1287–1289, 1990. 27

_____. Improved null-collision technique in the direct simulation monte carlo method: application to vibrational relaxation of nitrogen. **Computers &**

**Mathematics with Applications**, Elsevier, v. 35, n. 1, p. 139–154, 1998. 23, 26, 27

KOURA, K.; MATSUMOTO, H. Variable soft sphere molecular model for inverse-power-law of lennard-jones potential. **Physics of Fluids A: Fluid Dynamics**, AIP Publishing, v. 3, n. 10, p. 2459–2465, 1991. 28

LAUX, M. Optimization and parallelization of the dsmc method on unstructured grids. In: AIAA THERMOPHYSICS CONFERENCE, 32th. **Proceedings...** Atlanta, EUA, 1997. p. 23–25. 23

LEE, G.; CHANDRA, S. Numerical analysis of heat transfer enhancement from surfaces with cavities. In: AIAA AEROSPACE SCIENCES MEETING AND EXHIBIT, 44th. **Proceedings...** Reno, Nevada, EUA: AIAA, 2006. p. 0186. 6, 7, 11

LEITE, P. **Direct molecular simulation of step influence on a reentry vehicle surface**. 2009. 164 p. Master Thesis in Engineering and Space Technology - Combustion and Propulsion — National Institute for Space Research, São José dos Campos- SP, Brazil, 2009. Disponível em: <http://urlib.net/8JMKD3MGP8W/35TNLKS>. 10, 11, 12, 49, 87, 95, 96, 100, 108, 131, 134, 137, 142, 143

LEITE, P. H. M.; SANTOS, W. F. N. Computational analysis of rarefied hypersonic flow over a forward-facing step. In: AIAA THERMOPHYSICS CONFERENCE, 42th. **Proceedings...** Honolulu, Hawaii, EUA: AIAA, 2011. p. 3310. 87, 100, 108, 120, 131, 134

LENGRAND, J.; ALLEGRE, J.; CHPOUN, A.; RAFFIN, M. Rarefied hypersonic flow over a sharp flat plate: Numerical and experimental results. **AIAA journal**, American Institute of Aeronautics and Astronautics, p. 277–284, 1992. 62, 63, 69, 70, 71, 72, 73

LIU, N.; YIN-KWEENG, E. The impacts of the-step size in the application of the direct simulation monte carlo method to ultra thin gas film lubrification. **Journal of Micromechanics and Microengineering**, v. 12, p. 567–573, 2002. 20

LIU, S.; YU, P.; XU, K.; ZHONG, C. Unified gas-kinetic scheme for diatomic molecular simulations in all flows regimes. **Journal of Computational Physics**, Elsevier, v. 259, p. 96–113, 2014. xxi, 69, 73, 74, 75

LORD, R. Application of the cercignani-lampis scattering kernel to direct simulation monte carlo method. In: 158 INTERNATIONAL SYMPOSIUM ON RAREFIED GAS DYNAMICS, 17th. **Proceedings...** Aachen, Germany: Edited by ED.A.E.Beylich, 1991. p. 1427–1433. 48

_____. Some extensions to the cercignani–lampis gas-surface scattering kernel. **Physics of Fluids A: Fluid Dynamics**, AIP Publishing, v. 3, n. 4, p. 706–710, 1991. 48

_____. Direct simulation of rarefied hypersonic flow over a flat plate with incomplete surface accommodation. **Progress in Astronautics and Aeronautics**, American Institute of Aeronautics and Astronautics, v. 160, p. 221, 1994. 48

LORDI, J. A.; MATES, R. E. Rotational relaxation in nonpolar diatomic gases. **Physics of Fluids**, AIP Publishing, v. 13, n. 2, p. 291–308, 1970. 42

LUMPKINIII, F. E.; HAAS, B. L.; BOYD, I. D. Resolution of differences between collision number definitions in particle and continuum simulations. **Physics of Fluids A: Fluid Dynamics**, AIP Publishing, v. 3, n. 9, p. 2282–2284, 1991. 39

MEIBURG, E. Comparison of the molecular dynamics method and the direct simulation monte carlo technique for flows around simple geometries. **Physics of Fluids**, AIP Publishing, v. 29, n. 10, p. 3107–3113, 1986. 19

MILLIKAN, R. C.; WHITE, D. R. Systematics of vibrational relaxation. **The Journal of Chemical Physics**, AIP Publishing, v. 39, n. 12, p. 3209–3213, 2004. 44

MORGENSTERN, A.; CHOKANI, N. Hypersonic flow past open cavities. **AIAA Journal**, v. 32, n. 12, p. 2387–2393, 1994. 1, 6, 7, 8, 11

MOSS, J.; BIRD, G. Direct simulation of transitional floor for hypersonic re-entry conditions. **Journal of Spacecraft and Rockets**, American Institute of Aeronautics and Astronautics, v. 40, p. 830–843, 2003. 21

MOSS, J. N.; PRICE, J. M.; DOGRA, V. K.; HASH, D. B. Comparison of dsmc and experimental results for hypersonic external flows. In: AIAA THERMOPHYSICS CONFERENCE, 30th. **Proceedings...** San Diego, CA, EUA: AIAA, 1995. p. AIAA paper 95–2028. 18

MOSS, J. N.; SCOTT, C. D. Thermophysical aspect of re-entry flows. **Progress in Astronautics and Aeronautics**, American Institute of Aeronautics and Astronautics, New York, NY, EUA, 1986. 18

NANBU, K. Theorethical basis of the direct simulation monte carlo method. In: INTERNATIONAL SYMPOSIUM ON RAREFIED GAS DYNAMICS, 15th. **Proceedings...** Grado, Italy, 1986. p. 369–383. 23, 26

NANCE, R. P.; WILMOTH, R. G.; HASSAN, H. A. Comparison of grid-definition schemes for monte carlo simulations. **Journal of Thermophysics and Heat Transfer**, v. 11, n. 2, p. 296–303, 1997. 60

NARIS, S.; VALOUGEORGIS, D. The driven cavity flow over the whole range of the knudsen number. **Physics of Fluids**, AIP Publishing, v. 17, n. 9, p. 097106, 2005. 6, 7, 11

NESTLER, D. An experimental study of hypersonic cavity flow. **Journal of Spacecraft and Rockets**, v. 19, n. 3, p. 195–196, 1982. 1, 6, 7, 11

NESTLER, D.; SAYDAH, A.; AUXER, W. Heat transfer to steps and cavities in hypersonic turbulent flow. **AIAA Journal**, v. 7, n. 7, p. 1368–1370, 1969. 1, 6, 7, 11

ORAN, E.; CYBYK OH, C.; CYBYK, B. Direct simulation monte carlo: Recent advances and applications. **Annual Review of Fluid Mechanics**, Annual Reviews, v. 30, n. 1, p. 403–441, 1998. 21

PALHARINI, R. **Numerical investigation of aerothermodynamic in a reentry vehicle with surface discontinuity - like cavity**. 2010. 153 p. Master Thesis in Engineering and Space Technology - Combustion and Propulsion — National Institute for Space Research, São José dos Campos- SP, Brazil, 2010. Disponível em: <http://urlib.net/8JMKD3MGP7W/38CL3PB>. 11, 12

PALMER, G. E.; PULSONETTI, M.; WOOD, W. A.; ALTER, S.; GNOFFO, P.; TANG, C. Computational assessment of thermal protection system damage experienced during sts-118. **Journal of Spacecraft and Rockets**, v. 46, n. 6, p. 1110–1116, 2009. 4

PAOLICCHI, L. T. L. C. **Computational analysis of gap effects on the surface of reentry space vehicles**. 2011. 156 p. Master Thesis in Engineering and Space Technology - Combustion and Propulsion — National Institute for Space Research, São José dos Campos- SP, Brazil, 2011. Disponível em:

<http://urlib.net/8JMKD3MGP7W/394K2HS>. 12, 87, 89, 95, 100, 103, 108, 112, 114, 120, 125, 131, 134

PAOLICCHI, L. T. L. C.; SANTOS, W. F. N. Heat transfer and pressure distribution in a rarefied hypersonic gap flow. In: ENCONTRO DE MODELAGEM COMPUTACIONAL - EMC 2010, XIII. **Proceedings...** Nova Friburgo - RJ, Brasil, 2010. 103

PARKER, J. Rotational and vibrational relaxation in diatomic gases. **Physics of Fluids**, AIP Publishing, v. 2, n. 4, p. 449–462, 2004. 38, 42

PETLEY, D.; SMITH, D.; EDWARDS A.B., C. A.; II, H. H. Surface step induced gap heating in the space shuttle thermal protection system. **Journal of Spacecraft**, v. 21, n. 2, p. 156–161, 1984. 2

PIEKOS, E. **DSMC modeling of micromechanical devices**. PhD Thesis — Massachusetts Institute of Technology, 1995. 48

PIEKOS, E.; BREUER, K. Numerical modeling of micromechanical devices using the direct simulation monte carlo method. **Journal of Fluids Engineering**, American Society of Mechanical Engineers, v. 118, n. 3, p. 464–469, 1996. 50

PRASANTH, P.; KAKKASSERY, J. K. Molecular models for simulation of rarefield gas flows using direct simulation monte carlo method. **Fluid Dynamics Research**, Elsevier, v. 40, n. 4, p. 233–252, 2008. 24, 28, 31, 34, 35, 36, 41, 45

PULLIN, D.; HARVEY, J. Direct simulation calculations of the rarefield flow past a forward-facing step. **AIAA Journal**, v. 15, n. 1, p. 124–126, 1977. 142, 143, 144

PULSONETTI, M.; THOMPSON, R. Laura aerothermodynamics computations for space shuttle columbia sts-107 baseline and damage scenarios. In: AIAA FLUID DYNAMICS CONFERENCE, 35th. **Proceedings...** Portland, Oregon, EUA: AIAA, 2004. 3

PULSONETTI, M.; THOMPSON, R.; ALTER, S. Prediction of sts-107 hypervelocity flow fields about the shuttle orbiter with various wing leading edge damage. In: AIRBREATHING PROPULSION SUBCOMMITTEE MEETING, 27th. **Proceedings...** Colorado Springs, EUA: JANNAF, 2003. 3

PULSONETTI, M.; WILLIAN, W. Computational aerothermodynamic assemnt of space shuttle orbiter tile damage - open cavities. In: AIAA THERMOPHYSICS CONFERENCE, 38th. **Proceedings...** Toronto, Canada: AIAA, 2005. 8

RIEFFEL, M. A. A method for estimating the computational requirements of dsmc simulations. **Journal of Computational Physics**, Elsevier, v. 149, n. 1, p. 95–113, 1999. 61

ROGERS, E.; BERRY, C. Research at the npl on the influence at supersonic speeds and low reynolds numbers of thick laminar boundary layers. In: J.A.LAURMANN (Ed.). **Rarefied Gas Dynamics**. Paris, France: Academic Press, 1965. v. 1, p. 574. 97

ROWLEY, C.; WILLIAMS, D. Dynamics control of high-reynolds-number flow over open cavities. **Annual Review of Fluid Mechanics**, Annual Reviews, v. 38, p. 251–276, 2006. 6, 7, 11

SCANLON, T.; WHITE, C.; SCHUEBLER, M.; BROWN, R.; REESE, J. Thermochemistry modelling in an open-source dsmc code. In: INTERNATIONAL SYMPOSIUM ON SHOCK WAVES, 28th. **Proceedings...** Manchester, U.K., 2011. 43, 44

SCHÄFER, F.; BREUER, M.; DURST, F. The dynamics of the transitional flow over a backward-facing step. **Journal of Fluid Mechanics**, Cambridge Univ Press, v. 623, p. 85–119, 2009. 98

SEBASTIÃO, I. **Numerical simulation of MEMS-based cold gas micronozzle flows**. 2011. 234 p. Master Thesis in Engineering and Space Technology - Combustion and Propulsion — National Institute for Space Research, São José dos Campos - SP, Brazil, 2011. Disponível em: <http://urlib.net/8JMKD3MGP7W/3A8PU95>. 22

SHANKAR, P.; DESHPANDE, M. Fluid mechanics in the driven cavity. **Annual Review of Fluid Mechanics**, Annual Reviews, v. 32, n. 1, p. 93–136, 2000. 6, 7, 11

SHEN, C. **Rarefied gas dynamics: fundamentals, simulations and micro-flows**. New York, EUA: Springer Science & Business Media, 2006. 32

SHU, C.; MAO, X. H.; CHEW, Y. Particle number per cell and scaling factor effect on accuracy of dsmc simulation of micro flows. **International Journal of Numerical Methods of Heat and Fluid Flow**, Emerald Group Publishing Limited, v. 15, n. 8, p. 827–841, 2005. 19, 20, 56, 61

STRUCKMEIER, J.; STEINER, K. A comparison of simulated methods for rarefied gas flows. **Physics of Fluids**, AIP Publishing, v. 7, n. 11, p. 2876–2885, 1995. 21

SUN, Z.; TANG, Z.; HE, Y.; TAO, W. Proper cell dimension and number of particles per cell for dsmc. **Computers & Fluids**, Elsevier, v. 50, n. 1, p. 1–9, 2011. 6

TOKUMASU, T.; MATSUMOTO, Y. Dynamic molecular collision (dmc) model for rarefied gas flow simulations by the dsmc method. **Physics of Fluids**, AIP Publishing, v. 11, n. 7, p. 1907–1920, 1999. 62, 71

TSUBOI, N.; MATSUMOTO, Y. Experimental and numerical study of hypersonic rarefied gas flow over flat plates. **AIAA Journal**, American Institute of Aeronautics and Astronautics, v. 43, n. 6, p. 1243–1255, 2005. xxi, 69, 73, 74, 75

TSUBOI, N.; YAMAGUCHI, H.; MATSUMOTO, Y. Direct simulation monte carlo method on rarefied hypersonic flow around flat plates. **Journal of Spacecraft and Rockets**, v. 41, n. 3, p. 397–405, 2004. 62, 63, 69, 70, 71

VICENTI, W.; KRUGER, C. **Introduction to physical gas dynamics**. New York, EUA: Wiley, 1967. 16, 25

WAGNER, W. A convergence proof for bird's direct simulation monte carlo method for the boltzmann equation. **Journal of Statistical Physics**, Springer, v. 66, n. 3-4, p. 1011–1044, 1992. 18

WILMOTH, R. G.; LEBEAU, G. J.; CARLSON, A. Dsmc grid methodologies for computing low-density, hypersonic flows about reusable launch vehicles. In: AIAA THERMOPHYSICS CONFERENCE, 31th. **Proceedings...** Lousiana, EUA: Edited by AIAA Paper, 1996. p. 1812. 60

XUE, H.; FAN, Q.; SHU, C. Prediction of micro-channel flows using direct simulation monte carlo. **Probabilistic Engineering Mechanics**, Elsevier, v. 15, n. 2, p. 213–219, 2000. 19, 20, 21, 27, 28, 48, 50

YOON, S.; KWAKT, D. Implicit navier-stokes solver for three-dimensional compressible flows. **AIAA journal**, v. 30, n. 11, p. 2653–2659, 1992. 8

ZDANSKI, P.; ORTEGA, M.; JR., N. F. Heat transfer on shallow cavities: Aspect ratio and reynolds number influence. In: APPLIED AERODYNAMICS CONFERENCE AND EXHIBIT, 22th. **Proceedings...** Providence, Rhode Island, EUA: AIAA, 2004. p. 4961. 6, 7, 11

# PUBLICAÇÕES TÉCNICO-CIENTÍFICAS EDITADAS PELO INPE

### Teses e Dissertações (TDI)

Teses e Dissertações apresentadas nos Cursos de Pós-Graduação do INPE.

### Notas Técnico-Científicas (NTC)

Incluem resultados preliminares de pesquisa, descrição de equipamentos, descrição e ou documentação de programas de computador, descrição de sistemas e experimentos, apresentação de testes, dados, atlas, e documentação de projetos de engenharia.

### Propostas e Relatórios de Projetos (PRP)

São propostas de projetos técnico-científicos e relatórios de acompanhamento de projetos, atividades e convênios.

### Publicações Seriadas

São os seriados técnico-científicos: boletins, periódicos, anuários e anais de eventos (simpósios e congressos). Constam destas publicações o Internacional Standard Serial Number (ISSN), que é um código único e definitivo para identificação de títulos de seriados.

### Pré-publicações (PRE)

Todos os artigos publicados em periódicos, anais e como capítulos de livros.

### Manuais Técnicos (MAN)

São publicações de caráter técnico que incluem normas, procedimentos, instruções e orientações.

### Relatórios de Pesquisa (RPQ)

Reportam resultados ou progressos de pesquisas tanto de natureza técnica quanto científica, cujo nível seja compatível com o de uma publicação em periódico nacional ou internacional.

### Publicações Didáticas (PUD)

Incluem apostilas, notas de aula e manuais didáticos.

### Programas de Computador (PDC)

São a seqüência de instruções ou códigos, expressos em uma linguagem de programação compilada ou interpretada, a ser executada por um computador para alcançar um determinado objetivo. Aceitam-se tanto programas fonte quanto os executáveis.